
Hybrid and ultrafine-grained materials produced by high pressure torsion extrusion

Zur Erlangung des akademischen Grades Doktor-Ingenieur (Dr.-Ing)
genehmigte Dissertation von Herrn Dayan Nugmanov
Tag der Einreichung: 24.04.2024
Tag der Prüfung: 15.07.2024
Darmstadt 2024

1. Gutachten: Prof. Dr.-Ing. Horst Hahn
2. Gutachten: Prof. Dr.-Ing. Karsten Durst



TECHNISCHE
UNIVERSITÄT
DARMSTADT

Fachbereich Material- und
Geowissenschaften
Technische Universität Darmstadt
Institut für Nanotechnologie
Karlsruher Institut für Technologie

Nugmanov, Dayan: Hybrid and ultrafine-grained materials produced by high pressure torsion
extrusion

Darmstadt, Technische Universität Darmstadt

Veröffentlichungsjahr der Dissertation auf TUprints: 2024

Tag der mündlichen Prüfung: 15.07.2024

Lizenzangaben (CC BY 4.0 International)

Erklärung zur Dissertation

Hiermit versichere ich, die vorliegende Dissertation ohne Hilfe Dritter nur mit den angegebenen Quellen und Hilfsmitteln angefertigt zu haben. Alle Stellen, die aus Quellen entnommen wurden, sind als solche kenntlich gemacht. Diese Arbeit hat in gleicher oder ähnlicher Form noch keiner Prüfungsbehörde vorgelegen.

Darmstadt, den

(Nugmanov Dayan)

Abstract

The development of advanced structural materials by creating designed structures and architectures is one of the main areas of scientific work in the field of modern materials science.

High pressure torsion extrusion (HPTE), as one of the methods of severe plastic deformation, was used to process ultrafine-grained (UFG) samples of pure copper and hybrid samples. HPTE-processing of hybrid samples with straight Fe wires in the straight configuration embedded in the copper matrix leads to the creation of a helical architecture of the wires and a significant change of the wire cross section shape. The helical configuration (number of loops and pitch) can be easily varied by changing the HPTE-processing parameters (extrusion and rotation rate).

Results of finite element modelling, experimentally validated using copper samples with aluminium markers, were analyzed to gain a profound understanding of the influence of processing temperature and properties of the processed materials on the strain distribution in the bulk billet processed by HPTE. The calculations were performed for pure copper for HPTE regimes with resulting strains in a range between 0.3 and 12.0 at deformation temperatures of 25 and 100°C. It was established that the accumulated strain in HPTE can be as high as ~ 4 even in the middle of the round bar-billet, which shows the high efficiency of HPTE to obtain severe plastic deformation. By the comparison of the calculated strain distributions with experimentally measured ones in copper samples the spreading of the deformation zone along the height of the billet, caused by its sliding in the die could be revealed. It was established that the sliding increases with increasing deformation temperature and in creating accumulated strain. X-ray tomography was used to visualize the change of the shape of wire markers inserted in the billets prior to HPTE processing.

The potential of the HPTE method for obtaining high strength in bulk structural materials has been demonstrated. The helical architecture of iron reinforcements leads to a substantial enhancement in the plasticity of copper processed through severe plastic deformation (SPD). In particular, an extension of the stage of uniform elongation from ~ 1 to $\sim 4\%$ has been obtained.

The microstructure of the HPTE processed Cu shows a gradient structure, consisting of fine grains in the central area and of ultrafine grains on the edge and in the middle-radius zone. A detailed analysis of the tensile characteristics for the samples with gradient structure showed that the strength of copper after HPTE exhibiting a structure is similar to that of copper after others SPD techniques that result in a homogeneous UFG structure. The analysis of the contributions of various strengthening mechanisms revealed that the main strengthening factor in the HPTE-processed copper arises from high and low-angle grain boundaries, which act as effective obstacles to dislocation motion, as discussed by the Hall-Petch relationship.

Abstrakt

Die Entwicklung fortschrittlicher struktureller Materialien durch die Schaffung konstruierter Strukturen und Architekturen ist ein wichtiger Bereich der modernen Materialwissenschaft.

Das Hochdruck-Torsionsextrusion (HDTE) ist eine Methode der starken plastischen Verformung, die zur Bearbeitung von ultrafeinkörnigen (UFK) Proben aus reinem Kupfer und Hybridproben verwendet wird. Bei der HDTE-Bearbeitung von Hybridproben mit geraden Fe-Drähten in geradliniger Konfiguration, die in die Kupfermatrix eingebettet sind, bildet sich eine spiralförmige Architektur dieser Drähte aus und es kommt zu einer signifikanten Veränderung der Drahtquerschnittsform. Die Anzahl der Schleifen und die Steigung der schraubenförmigen Konfiguration können durch eine Änderung der HDTE-Verarbeitungsparameter (Extrusions- und Rotationsgeschwindigkeit) leicht variiert werden.

Die Ergebnisse der Finite-Elemente-Modellierung wurden analysiert, um ein tieferes Verständnis des Einflusses der Verarbeitungstemperatur und der Eigenschaften der verarbeiteten Materialien auf die Dehnungsverteilung in dem mit HDTE verarbeiteten Knüppel zu erlangen. Die Validierung erfolgte anhand von Kupferproben mit Aluminiummarkern. Die Berechnungen wurden für reines Kupfer für HDTE-Regime mit resultierenden Dehnungen im Bereich zwischen 0,3 und 12,0 bei Verformungstemperaturen von 25 und 100 °C durchgeführt. Es wurde festgestellt, dass die akkumulierte Dehnung bei HDTE sogar in der Mitte des Rundstabs bis zu ~ 4 betragen kann. Dies zeigt die hohe Effizienz von HDTE bei der Erzielung starker plastischer Verformung. Durch den Vergleich der berechneten Dehnungsverteilungen mit experimentell gemessenen Dehnungsverteilungen in Kupferproben konnte gezeigt werden, wie sich die Verformungszone entlang der Höhe des Knüppels ausbreitet, die durch das Gleiten in der Matrizie verursacht wird. Es wurde festgestellt, dass das Gleiten mit zunehmender Verformungstemperatur und akkumulierten Dehnungen zunimmt. Durch die Anwendung der Röntgentomographie wurde die Veränderung der Form von Drahtmarkierungen, die vor der HDTE-Bearbeitung in die Knüppel eingebracht wurden, sichtbar.

Das Potenzial der HDTE-Methode zur Erzielung hoher Festigkeit in Massenstrukturmaterialien wurde nachgewiesen. Die spiralförmige Architektur von Eisenverstärkungen führt zu einer erheblichen Verbesserung der Plastizität von Kupfer, das durch schwere plastische Verformung (SPV) verarbeitet wird. Insbesondere wurde eine Verlängerung der Phase der gleichmäßigen Dehnung von etwa 1 auf etwa 4% erreicht.

Das Mikrogefüge des mit HDTE bearbeiteten Kupfers weist eine Gradientenstruktur auf. Im zentralen Bereich sind feine Körner zu finden, während am Rand und in der Zone mit dem mittleren Radius ultrafeine Körner vorherrschen. Eine detaillierte Analyse der Zugfestigkeitseigenschaften für die Proben mit Gradientenstruktur zeigt, dass die Festigkeit von Kupfer nach HDTE, das eine solche Struktur aufweist, ähnlich ist wie die von Kupfer nach anderen Techniken der SPV, die zu einer homogenen UFK-Struktur führen. Die Analyse ergab, dass der Hauptverfestigungsfaktor im HDTE-verarbeiteten Kupfer von hohen und niedrigwinkligen Korngrenzen ausgeht, die als wirksame Hindernisse für die Versetzungsbewegung wirken, wie in der Hall-Petch-Beziehung beschrieben.

Table of contents

1.....Introduction	1
1.1. Motivation	1
1.2. Objective, Scope and Outline of thesis	3
2.....Scientific background	5
2.1. Strength and plasticity of hybrid materials	5
2.1.1. Mechanical properties of hybrid materials with gradient architecture	6
2.1.2. Mechanical properties of helically architected hybrid materials	8
2.1.3. Strengthening mechanisms of pure metals and alloys subjected to SPD	11
2.2. High pressure torsion extrusion process	15
2.2.1. HPTE processing of pure metals	16
2.2.2. HPTE processing of hybrid samples	17
2.3. Evaluation of strain in HPTE	18
2.3.1. Analytical equation for the calculation of strain in HPTE	18
2.3.2. Finite element modeling of the HPTE processes	20
3.....Materials, samples preparation and investigation methods	22
3.1. Choice of materials	22
3.2. Initial sample design and manufacturing	23
3.2.1. Preparation of samples of pure metals for HPTE	23
3.2.2. Preparation of hybrid samples for HPTE	23
3.2.3. Processing of pure copper	26
3.2.4. Processing of hybrid samples	26
3.3. Characterization methods	27
3.3.1. General characterization	27
3.3.2. XRD tomography of hybrid samples	28
3.3.3. Methods for microstructural characterization	28
3.3.3.1. Metallographic sample preparation	28
3.3.3.2. Scanning electron microscopy	29
3.3.3.3. Grain and subgrain size; grain boundary misorientations	31
3.3.3.4. Scanning transmission electron microscopy	31
3.3.3.5. Estimation of dislocation density by EBSD-SEM data	33
3.3.3.6. Creation of dislocation density map from ACOM-TEM data	34
3.3.3.7. Estimation of integral dislocation density from X-ray diffraction peak broadening	36
3.4. Mechanical properties testing	38
3.5. Finite element modeling settings and validation	39
4.....Investigation of material flow at HPTE: FEM calculations and experimental validation	41

4.1.	Strain analysis of the processed billets	41
4.1.1.	Intermediate processing	41
4.1.2.	Full-height processing	41
4.2.	FEM modelling of the HPTE process	43
4.2.1.	Definition of contact friction coefficients	43
4.2.2.	Discussion of the helical shape of HPTE - processed samples as a validation of the calculated strain distribution	47
5.....	Characterisation of gradient and hybrid samples after HPTE	49
5.1.	Microstructure of copper after HPTE	49
5.1.1.	Microstructure characterisation	49
5.1.1.1.	Microstructure in the central area of the billet	50
5.1.1.2.	Microstructure in the middle-radius area of the billet	54
5.1.1.3.	Microstructure in the edge area of the billet	57
5.1.2.	Dislocations density	57
5.2.	Discussion of the microstructure of the HPTE - processed copper	58
5.3.	3D configurations of hybrid samples after HPTE	61
5.3.1.	Initial configurations	61
5.3.2.	HPTE processing of hybrid samples	63
5.3.2.1.	Configurations designed for the tensile tests	63
5.3.2.2.	Microstructure characterization of hybrid samples after HPTE	64
6.....	Mechanical properties of pure copper and helically architected hybrid samples	66
6.1.	Mechanical properties of pure copper after HPTE	66
6.1.1.	Analysis of strengthening factors in HPTE-processed pure copper	68
6.2.	Mechanical properties of hybrid samples after HPTE	70
6.2.1.	Analysis of the strain hardening rate of Cu and Cu-Fe hybrid samples	72
6.2.2.	Analysis of helical reinforcements during the uniaxial extension process	74
6.2.3.	Geometrical consideration of the helical elements extension in the hybrid samples	75
7.....	Conclusions and Outlook	78
7.1	General discussion and conclusions	78
7.2	Outlook and future investigations	80
	References	82
	Acknowledgements	89
	Curriculum Vitae	90

List of figures

- Figure 2.1** Schematic of the cross-sectional microstructure of the gauge section of the gradient sample consisting of a UFG layer (dark blue) and a deformed CG layer (blue) on a CG core (light blue) (from [21]) (a). Architected material of the ‘soft core/hard shell’ type: cross-section showing a CG core and an UFG sheath (b), stress-strain curves for various values of the volume fraction λ of the core material (c). Pictures b and c are taken from [41]. 7
- Figure 2.2** Depiction of straight reinforced composite (top) and corrugation reinforced composite (bottom) (a) [22]. Helical assembly scheme of curved fibrous building blocks (b) [49] and corrugated strips (c) from [22]. Stress as a function of elongation for flat and corrugated strips (d) [22]. Computed evolution of the flow stress as a function of strain for the perfectly plastic matrix strengthened by reinforcement with the different geometries of corrugation (e) [22]. Tensile force directed along Y direction. Reprinted from [22]. 8
- Figure 2.3** Tension of a plate with an embedded thin layer normal to the direction of tensile load (a). An architected material of the ‘artificial crystal’ type: schematic drawing (b), engineering stress-strain dependence under uniaxial tension for several values of the inclination angle α of the CG layers (c) [44]. 10
- Figure 2.4** Typical engineering stress–strain curves for pure Cu subjected to SPD. HPT with different resulting strain (a) taken from [50]. Curve A – annealed coarse grained Cu; B – room temperature rolling to 95% (CW); C – liquid-nitrogen temperature rolling to 93%; D - 93% CW+180°C, 3 min; E – 93% CW+200°C, 3 min (taken from [51]). Relation between the yield strength and the uniform elongation in CG and UFG copper including the results for the samples with the bimodal structure produced by annealing for 1, 3 and 10 min at 200 °C after ECAP (c) (taken from [7]). 12
- Figure 2.5** HV saturation depending on the accumulated strain during the HPTE (a) [12], HPT and ECAP (b) [58] processes. The grain size obtained from inverse pole figure maps in the axial direction parallel to the $\langle 111 \rangle$ and $\langle 001 \rangle$ crystal orientations, considering high angle boundaries as a function of strain (c) [53]. 13
- Figure 2.6** Schematic diagrams of the HPTE (a) and HPT (b) processes. Schemes are taken from [12] (a) and from [29] (b). 16
- Figure 2.7** Formation of a spiral-shaped layered architecture by means of HPTE: initial arrangement of embedded fibers (a); various shapes of a resulting spring (b, c); an example of a spiral layer structure in the copper/aluminum system (d, e). The Cu matrix is colored with yellow and aluminum fibers (transformed to spiral Al sheets in the process of HPTE) are shown in blue. Pictures are taken from [41]. 18
- Figure 2.8** Detailed drawing of the HPTE tool with smooth cone surfaces (a), 6-wrench-shape surfaces (b) and 3D image of a billet inside HPTE die (c) [12]. External directions are shown as radial direction (RD), extrusion direction (ED) and shear direction (SD) (d). 19
- Figure 2.9** Equivalent strain in dependence on the radius calculated using FEM and Equation (2.12) for $v10w1$ (a) and $v1w1$ (b) regimes. Plots are taken from [12]. 21
- Figure 3.1** Scheme of hybrid samples preparation: assembling of matrix and rods (a); direct extrusion (b). 25
- Figure 3.2** Drawing of initial configurations of hybrid Cu samples before CE processing. Diameter of each sample is 20 mm. 25
- Figure 3.3** Images of the cross sections of the billets prepared for the HPTE. 26
-

Figure 3.4 Interphase boundary in the Cu-Al hybrid samples after CE. Secondary electron images (a), EDS signal along the scanning lines (b).	26
Figure 3.5 Scheme of the heating elements (marked by shaded areas) location in the top part of the HPTE machine. Top view.	27
Figure 3.6 Schematic of the radiography from [94].	29
Figure 3.7 Scheme of the samples location for EBSD study on the cross-section of the HPTE-processed rod.	30
Figure 3.8 The formation of the electron backscattered diffraction pattern (EBSP) (a) determination of the Kikuchi bands position in the diffraction pattern (b, c) [96].	31
Figure 3.9 Precession geometry in the modern condenser-objective TEM (taken from [99]) applied for the ACOM-TEM technique (a) and the center precession pattern (b) (taken from [101]) are an integration of the simulated tilt series (contrast inverted) that surround the vertical axis, forming an effective cone of illumination.	33
Figure 3.10 Principles of the GND density calculation based on the kernel average misorientation (a, b) for the case of a 2 nd neighbor evaluation and a step size of 100 nm (c). Grain boundaries are marked in red. Misorientations that exceed the minimum threshold value of 2° are excluded from the calculation of the average misorientation of neighboring points to a given measurement point g_0 . Picture was taken from [106].	35
Figure 3.11 Alignment of the GND distribution maps calculation for the ACOM TEM data of coarse grained aluminum. Bright field image (a), HAADF (b), oriented image map (c) and GND map (d) after reconstruction in ATEX.	37
Figure 3.12 Typical X-ray diffraction pattern from the edge area of the Cu rod after HPTE <i>v1w1</i> regime ($\lambda_{Cu}=154.183$ pm) (a). Williamson-Hall plot of the XRD pattern shown in (b).	38
Figure 3.13 A schematic drawing of the tensile test sample (a) and photo of the sample after machining (b). Dimensions are given in millimeters.	40
Figure 3.14 3D images of the billet and marking lines, used for the FEM, in initial rod (a), at the intermediate stage of the HPTE process (b) and after processing (c).	42
Figure 3.15 Engineering stress-strain curves for FEM calculation of HPTE deformation of copper	42
Figure 4.1 The images of the longitudinal (a, b, c) cross sections of the copper samples with six aluminum markers obtained using optical microscopy. The samples were processed by the <i>v6w1</i> (a) and <i>v1w1</i> (b, c) HPTE regimes at 25°C. The position of the parting plane between the top and bottom HPTE dies, is indicated by the dashed lines in (a), (b).	43
Figure 4.2 The 2D images of the aluminum wires in copper billets after the <i>v6w1</i> regime at 100°C (a-d) and at 25°C (e-h) were captured in both longitudinal (a, e) and transversal (b-d, f-h) sections. The initial configurations included six wires (a-d) and five wires (e-h). Optical microscopy was combined with the results of X-ray tomography in (a, b, d) to obtain detailed information.	46

-
- Figure 4.3** FEM-simulated configurations of the marker lines after the HPTE process executed using the $v10w0$ (a) and $v6w1$ (b, c) regimes at deformation temperatures of 25°C (a, b) and 100°C (c). 47
- Figure 4.4** The strain distribution after HPTE of copper at 100°C (right part of a-d) and at 25°C (left part of a-d) is shown. The HPTE regimes $v10w0$ (a, c) and $v6w1$ (b, d) were used for the calculations and are represented in transversal (a, b) and longitudinal (c, d) sections. The transversal section is taken at the half of the height of the billet. 48
- Figure 4.5** The accumulated strain distribution in the transversal cross section at the half of the billet height was calculated using the FEM and Equation (2.12) for the $v10w0$ and $v6w1$ HPTE regimes at 25 (a)°C and 100 (b)°C. The strain estimate by Equation (2.12) utilized experimentally obtained values of rotation velocity w_e from Table 4.2. 49
- Figure 5.1** The typical OIM map (a, left), grain boundaries map (a, right) and BSE image (b) of the annealed Cu rod (longitude section). In the OIM map, the coloring corresponds to the projection of the ED in the inverse pole figure. The grain boundaries map indicates high angle misorientations ($\theta > 15^\circ$) with blue lines, and low angle misorientations ($2^\circ < \theta < 15^\circ$) with red lines. 51
- Figure 5.2** The OIM maps (left) and grain boundaries maps (right) of the $v10w0$ (a-c) and $v10w1$ (d-f) regimes are shown for both transversal (above) and longitudinal (bottom) sections of the sample areas after HPTE at 100°C. These maps corresponds to the center (a, d); mid-radius (b, e); and edge regions (c, f). In the OIM maps, coloring represents the projection of the ED in the inverse pole figure. In grain boundaries maps, high angle misorientations ($\theta > 15^\circ$) are marked with blue lines, while low angle misorientations ($2^\circ < \theta < 15^\circ$) are marked with red lines. 53
- Figure 5.3** OIM maps of the $v1w1$ in the transversal (above) and longitudinal (bottom) sections of the sample are shown at (a) the center; (b) the mid-radius; and (c) the edge, after HPTE at 100°C. The coloring in the OIM map corresponds to the projection of ED in the inverse pole figure. In the grain boundaries maps, high angle misorientations ($\theta > 15^\circ$) are marked by blue lines, and low angle misorientations ($2^\circ < \theta < 15^\circ$) are marked by red lines. 55
- Figure 5.4** Grain size distribution (D_{15}) based on the specific area of the grains (S_i/S) after the $v1w1$ regime at 100°C in the transversal (a) and longitudinal (b) sections. 56
- Figure 5.5** Misorientation distributions of the boundaries of crystallines after the $v1w1$ regime at 100°C in the (a) transversal and (b) longitudinal sample sections. 56
- Figure 5.6** The microstructure of HPTE Cu in the mid-radius area of the longitudinal section of the billet subjected to the $v1w1$ regime is depicted in the following images, all at the same scale. (a) TEM BF image; (b) ACOM TEM OIM map, highlighting LABs ($3^\circ < \theta < 15^\circ$) with white lines) and HABs ($\theta > 15^\circ$) with black lines; (c) GND distribution map from ACOM TEM, with all GBs marked by white lines; (d) EBSD OIM GBs network, with LABs marked by red lines and HABs marked by blue lines. 58
- Figure 5.7** The distribution of dislocation density in the Cu sample before and after various HPTE regimes at 100°C. 60
- Figure 5.8** The 3D reconstruction of the initial samples in configurations (1) (a, b) and (2) (c, d). XRD tomography was conducted using ORS Dragonfly reconstruction software. 63
-

-
- Figure 5.9** The interphase boundary in the Cu-Al hybrid samples in configuration (1) after DE at 250°C. The figure consist of transversal (a, b) and longitudinal (c-e) sections. Image (a) displays secondary electron images, image (b) exhibits the EDS detector-induced signal along the scan line, and images (c-e) present mapping data. 64
- Figure 5.10** X-ray tomography of the samples in configuration (1) after the *v18w1* (a-e) and *v6w1* (f-j) regimes conducted at 100°C. 3D (a, f) and 2D (b-e, g-j) images were served using ORS Dragonfly reconstruction software. The 2D images in the transverse section (b-d, g-i) were captured from the top (b, g), middle-height (c, h) and bottom (d, i) sections. The 2D images in the longitudinal section (e, j) were taken along the diameter of the billet. 65
- Figure 5.11** The transversal (a, c) and longitudinal (b, d) sections of the Cu-Al (a, b) and the Cu-Fe (c, d) hybrid samples after the *v18w1* HPTE processing. The longitudinal section in the middle-part of the sample's height corresponds to the gauge of tensile sample. 66
- Figure 5.12** SEM image (a, c), EDS scan along the line (b) and mapping (d, e) of the Cu-Al (a, b) and Cu-Fe (c-e) hybrid samples after the *v6w1* HPTE processing. The longitudinal section in the middle-part of the sample height is presented. 67
- Figure 6.1** The microhardness distribution along the radius (a), and tensile curves of Cu (b) before and after the HPTE at 100°C. 68
- Figure 6.2** The tensile curves of copper, Cu-Al (a, c), and Cu-Fe (b, d) hybrid samples in the configuration (1) before and after the HPTE process. 73
- Figure 6.3** The normalized strain hardening rates, θ/σ_t , of the copper and Cu-Fe hybrid samples in the configuration (1) after the HPTE process, as fuction of the true strain. 75
- Figure 6.4** The image of the longitudinal section of the hybrid Cu-Fe sample in the configuration (1) processed by the *v6w1* regime, showing the state after 3.1% of extension (a, b) and after full rupture (c, d). The microhardness of iron wires in the area of holders and in the gauge was displayed on the scheme. The schemes (b, d) illustrated the shape of the longitudinal section of the hybrid sample, with the copper matrix marked by the green colour and the iron wires marked by the grey colour. The microhardness of the copper matrix was measured in the middle-radius region of the rod. 76
- Figure 6.5** The geometry of the helical wire after twisting in 3D image (a) and a 2D longitudinal diametral section (b). 77
- Figure 6.6** The diagram illustrated two relationships: (a) the length of the helixes formed after HPTE plotted against the length of the gauge of the tensile sample, and (b) and the elongation of the helixes plotted against the elongation of the gauge. 79
-

List of tables

Table 2.1 Regimes of HPTE process and respective von Mises strains for cone-shape dies.	20
Table 3.1 Chemical composition of metals (in wt. %).	23
Table 3.2 Regimes of HPTE process employed for processing of the hybrid samples.	28
Table 3.3 Data for FEM calculation of HPTE.	42
Table 4.1 The experimentally obtained number of loops of the marker wires after the HPTE process and the values of friction coefficients employed for the FEM calculation.	45
Table 4.2 The experimentally obtained values of friction coefficients employed for the FEM calculations.	46
Table 5.1 The structural parameters of Cu samples after the HPTE treatment at 100°C were determined based on SEM–EBSD analysis in the longitudinal and transverse cross sections.	52
Table 5.2 The types of resulting structures in the copper samples subjected to the HPTE at 100°C.	62
Table 6.1 The tensile properties and microhardness of the copper before and after the HPTE conducted at 100°C.	69
Table 6.2 The Vickers hardness (<i>HV</i>), yield strength (<i>YS</i>), ultimate strength (<i>UTS</i>), and elongation to failure (δ) of Cu after the HPTE and other SPD methods.	69
Table 6.3 The structure parameters of copper were measured in the transversal section of the HPTE sample, which was used for the calculations of strengthening contributions.	71
Table 6.4 The contributions (in MPa) of various strengthening mechanisms in Cu before and after the HPTE process conducted at 100°C. The testing sample included the central and mid-radius areas of the sample.	71
Table 6.5 The tensile properties of copper gradient samples, as well as the Cu-Al and Cu-Fe hybrid samples before and after the HPTE process.	73
Table 6.6 The geometry parameters of the helical wires after HPTE.	78

Definition of abbreviations and symbols

Latin symbols and abbreviations

Abbreviation	Full name	unit
ACOM	automated crystal orientation mapping	
ARB	accumulative roll bonding	
ASTM	american society for testing and materials	
CAD	computer aided design	
CE	conventional extrusion	
CEE	cycle expansion extrusion	
CG	coarse grained	
CI	coinfidence index	
D ₂ , D ₁₅	(sub)grain size	nm
<D>	crystallite size (from XRD)	nm
DP	diffraction pattern	
EBS	electron back scattered diffraction	
EBSP	electron back scattered pattern	
ECAP	equal channel angular pressing	
ED	electrodeposition	
EDX	energy dispersive X-Ray spectroscopy	
IHPT	incremental high pressure torsion	
IGES	International graphical exchange standard	
FCC	face-centered cube (lattice structure)	
FEM	finite element modeling	
FG	fine-grained	
GB	grain boundary	
GND	geometrically necessary dislocation	m ⁻²
GNG	gradient nano-grained (structure)	
H-P	Hall-Petch (relation)	
h.p.c	hexagonal close-packed (lattice structure)	
HV	microhardness	MPa
HAADF	high angle annular dark field	
HCF	high cycle fatigue	
HPT	high pressure torsion	
LCF	low-cycle fatigue	
m	strain rate sensitivity	
MD	molecular dynamic	
MIF	multidirectional isothermal forging	
NC	nanocrystalline	
ROI	region of interest	
rpm	rotations per minute	min ⁻¹
RT	room temperature	°C
SB	shear band	

SEM	scanning electron microscopy	
SFE	stacking fault energy	
SHC	strain hardening capacity	
SPD	severe plastic deformation	
SSD	statistically stored dislocations	m ⁻²
STEM	scanning transmission electron microscopy	
T _m	melting temperature	°C
TEM	transmission electron microscopy	
TRIP	transformation-induced plasticity	
UFG	ultra-fine grained	
UTS	ultimate stress	MPa
XRD	X-ray diffraction	
YS	yield stress	MPa
Z	Zener–Hollomon parameter	s ⁻¹

Greek symbols and abbreviations

α	the angle of incline of the reinforcement element to the axis	°
$\delta(\theta)$	full width at half maximum	°
ε	strain	
$\langle \varepsilon^2 \rangle^{1/2}$	microstrain (for XRD)	%
$\dot{\varepsilon}$	strain rate	s ⁻¹
λ	wave length	pm
ρ (dd)	dislocation density	m ⁻²
σ_s	flow stress	MPa
τ	shear stress	MPa
2θ	scattering angle	°
θ	normalized work hardening rate	
γ	shear strain	
γ_{sf}	stacking fault energy	mJ/m ²

1. Introduction

1.1. Motivation

For the last 30 years, nanocrystalline (NC) and ultrafine-grained (UFG) materials attracted the attention of researchers worldwide due to their advanced mechanical and physical properties. These properties have led to many opportunities for practical applications, e.g. in the production of medical implants, superplastic forming of light metals and some others [1-5]. Generally, NC materials can be synthesized using various bottom-up techniques like chemical and physical deposition methods resulting in a formation of nano-powders and thin films. An alternative route is to refine the microstructure via the top-down approach. The grains of bulk coarse-grained (CG) metals and alloys are reduced in size to sub-micrometer and even nanometer scales using severe plastic deformation (SPD) techniques [4, 6, 7]. The best-known SPD methods are high pressure torsion (HPT) [4, 8], equal channel angular pressing (ECAP) [4, 6], accumulative roll bonding (ARB) [9], twist extrusion (TE) [10], multidirectional isothermal forging (MIF) [11]. SPD methods are especially attractive because they open up new possibilities for the production of bulk nanostructured materials (BNM) even at industrial scales and allow the creation of UFG structures at various length scales. Recently, a new method, scaling up the HPT process, namely High Pressure Torsion Extrusion (HPTE), has been developed by Ivanisenko et al. [12], [13]. HPTE method combines HPT with conventional extrusion (CE).

Despite the considerable improvement of the strength of UFG materials, the study of fatigue properties of SPD materials has led to controversial results. On the one hand, there are many reports demonstrating an increase of the high cycle fatigue (HCF) strength σ_{HCF} of UFG materials [14] [15]. On the other hand, a significant decrease in the fatigue strength of low-cycle fatigue (LCF) σ_{LCF} and the fatigue life N_f of UFG metals and alloys has been reported [16, 17]. Careful investigations of LCF properties in UFG pure copper have shown that cyclic loading with comparably high amplitude of maximal cycle strain is accompanied by the significant softening of a material [18]. The analysis of surface deformation features revealed strong localization of deformation in shear bands (SBs), extending over the entire specimen surface, and the formation of cracks or voids along them. The decay in fatigue properties in combination with the energy and material costs for SPD processing significantly limit the possibilities for industrial applications of fine-grained (FG) and UFG materials. A simple way to improve LCF properties is annealing, which can help to extend uniform elongation and to improve maximal elongation of the UFG materials in tensile tests [19].

Under certain annealing conditions, promising mixed UFG-CG microstructure can be obtained [20], which yields much longer (10 times more, with the same $\Delta\sigma/2$) fatigue life (LCF strength). Unfortunately, annealing is accompanied by softening and partial or complete disappearance of the SPD-achieved improvement a strength.

One of the most impressive ways to extend the uniform elongation stage is to create an architecture combining UFG – or nanomaterial with high strength and CG material with high plasticity. In particular, T. Fang et al. [21] suggested that the ideal architecture may contain a NC metal film adherent on a CG bulk material of the same metal with a graded grain-size

transition between them. This creates a gradient architecture without a sharp interface between NC film and CG substrate, which is elastically homogeneous with a gradient in plasticity. This approach may offer an improvement in mechanical response and provide a unique opportunity for retaining the intrinsic tensile plasticity of CG metals without strain localization.

Another configuration of an architected material consist of corrugated elements embedded in a matrix. For example, Bouaziz demonstrated experimentally in [22] that it is possible to obtain two stage tensile curves of hybrid samples containing copper matrix and corrugated iron wires, embedded in the gauge part of the tensile specimen. Recently, several research groups proposed that SPD processing techniques can be applied with a great efficiency to produce architected hybrid materials with a very fine grain size [23, 24]. The claim of this nascent paradigm shift is well founded and further development of SPD in the direction proposed to control the rate of hardening and localization of the material under loading. The expected outcome of such research will be the creation of hybrid materials in which the advantages of nanostructuring of their constituents are enhanced by their rearrangement at larger length scales up to the macroscopic level. A reference to hybrid materials in this connection is in keeping with their definition given by Ashby and Bréchet [25], as these materials are comprised by two or more constituents, and their properties are crucially determined by their inner architecture. A prominent example of such materials is metal-based composites in which architecture is achieved by SPD processing along with concurrent nanostructuring [23, 24, 26]. In this respect, the HPTE method is attractive, as it allows for the formation of helical architected wires in the UFG matrix, as it was demonstrated for copper samples with embedded aluminum wires [12]. HPTE regimes, defining the number of loops of a twisted wire (similar to the geometry of corrugated wire in [22]) will control the length of the uniform elongation stage in the tensile curve. Thus, HPTE processing will provide a conjoint process result in both refinement of the microstructure of the matrix material and twisting of the wires into a spiral. Therefore, both the wire configuration in the hybrid samples as well as microstructure of the matrix should be analyzed.

Annealing is one efficient way to improve mechanical properties of hybrid materials. In the case of different thermal stability of the chosen materials, it is possible to combine a harder matrix with a softer embedded material and, vice versa, the softer matrix with harder reinforcements. In this case, one can obtain an extruded matrix material with significantly better quality of the conjugation between the matrix and reinforcements, than that of the cast matrix material, as used by Bouaziz in [22].

1.2. Objective, Scope and Outline of thesis

Objective:

The **main aim** of the present thesis is to investigate the opportunities of the HPTE method for the processing of bulk UFG samples of pure metals and hybrid materials at room and elevated temperatures, in particular, to enhance mechanical properties.

Objectives:

- Analysis of the strain distribution in the work piece at all HPTE conditions used in the present study by means of finite element modeling.
- Analysis of the contributions of various strengthening mechanisms in the HPTE processed materials.
- Design of hybrid specimens with a helical architecture in order to enhance their mechanical properties.

Scope:

The investigations within the present work can be divided into two parts:

1) technical part, that includes the design and preparing of hybrid samples with helical architecture, the choice of the HPTE processing regimes, and the characterisation of the resulting configuration / microstructure of hybrid and UFG samples, as well as modeling of the HPTE process by the finite element method.

2) analysis of the static strength of hybrid / UFG samples to reveal the influence of the helical configuration on the tensile behavior and tensile strength of hybrid samples as well as contributions of strengthening factors in the tensile strength.

Thesis outline:

Chapter 1 is an introduction, which shortly explains the motivation for the present work, main objectives and scope of investigations.

Chapter 2 a review of the literature is presented, where the strengthening mechanisms of UFG and hybrid materials are considered. Modern concepts of the relationship between tensile strength, maximal elongation and configuration of hybrid materials are discussed. Further, this chapter summarizes briefly the background concerning the HPTE method, microstructure and mechanical properties of materials subjected to HPTE, as well as simulations of the HPTE process and resulting strain distribution calculations.

Chapter 3 contains the description of investigated materials, preparation of billets for HPTE and HPTE processing regimes used for pure copper and hybrid samples, experimental investigation techniques and characterization methods.

Chapter 4 contains the calculations of the strain distribution after different HPTE processing regimes by finite element modeling.

Chapter 5 the microstructure of the HPTE-processed billets and 3D configurations of hybrid samples with helical geometry after processing is described.

Chapter 6, mechanical properties of pure copper and hybrid samples before and after HPTE. An analysis of the strain hardening of pure and hybrid copper samples processed by HPTE with different helical configurations was carried out. The expanded part of the uniform elongation of hybrid samples was obtained and the mechanism of action of the helix geometry of the strengthening elements, which ensures an increase in the stage of uniform elongation, was discussed.

Chapter 7, the main conclusions from each of the Chapters 4-6. The outlook regarding the opportunities for the scientific and practical applications for the results of the thesis is represented.

2. Scientific background

UFG metals, including those processed by the HPT method, usually show very high strength, but limited tensile ductility (with uniform elongation reaching only a few percent) and almost no work hardening [4]. Low uniform elongation is a disadvantage of NC- and UFG-metals, despite they often show high values of elongation to failure [5, 27], which is realized in a high value of the reduction of area before the failure and large post-necking strain. Normally, for structural materials tested at room temperatures, grain boundary sliding or diffusional creep is not active sufficiently to accommodate plastic straining [28].

A mechanism of the deformation localization in shear bands during tensile testing of UFG pure copper was investigated in detail by Matsutani [29]. In this work it was demonstrated how intrinsic plasticity could be realized via different deformation modes: pure shear deformation provided higher uniform and maximal elongation in comparison to simple shear deformation. A change of the deformation mode was realized via dented and undented tensile gauge. The improvement of plasticity is a result of suppression of evolution of many micro-shear bands in narrow regions which cause a rapid decrease in plate thickness. The fact that there is no significant difference in the shape of stress–strain curves for both dented and undented specimens suggests that the presence of dents affects only shear deformation behavior during localized deformation.

As was considered for aluminum and its alloys, SPD by ECAP [30] as well as other techniques, e.g. HPTE [31], can activate all possible deformation modes, that can be varied from pure shear to simple shear. During subsequent mechanical tests, a rapid localization of deformation and a gradual decrease in the engineering stresses occur as a result of the neck formation. In addition, dimples were observed on the fracture surfaces of various UFG metals, indicating plastic deformation before fracture [32]. By this way, experimental data have hinted to the possibility that the generally observed low plasticity in UFG metals may be extrinsic rather than intrinsic. Indeed, limited tensile ductility of UFG metals has been often attributed to the absence of work hardening, so that strain localization and early necking occur immediately after the onset of yielding. On the other hand, intrinsic tensile plasticity of UFG metals can be detected by an effective suppression of strain localization in heterogeneous UFG/CG material. For example, Q. Pan in [33] demonstrated significant improvement of both intrinsic plasticity, and LCF characteristics of gradient NC pure copper. Further, in the present work the functions of strengthening in composite hard/soft materials with a special architecture, where the sample geometry works as a design allowing to change the deformation mode, in a similar way as in the work of Matsutani [29, 34], will be considered.

2.1. Strength and plasticity of hybrid materials

First, let us define the term "architected material". In [35], architecture is understood as a combination of different structures of materials, and, therefore, it can be considered at different scales, i.e. from macro to micro. An architected material can be defined as the combination of several materials (or the geometry shape of one material), disposed of predefined morphology, in which a representative elementary volume has at least one dimension that is very small in comparison with the dimensions of the part it composes [36].

According to this definition, a large number of materials of very different types, such as bulk and layered composites, cells, foam, etc. can be regarded as architected materials. It is necessary to mention that various terms offered in the literature are largely overlapping, for example, hybrid materials [25], multi-materials [36], tailored materials [37]. For the improvement of tensile plasticity of UFG materials, the gradient-architected and helically-architected materials are most interesting, since such architecture allows to obtain plasticity even in materials, consisting of hard and brittle elements. In the nature, for example, fracture surface of the *Clio Pyramidata* shell reveals a microstructure composed of densely packed curved fibrous building blocks [38]. Polished transverse cross-sections provide further evidence of the helical assembly of the fibrous building blocks and multiple series of parabolic arced patterns with alternating transversely and parallel cut regions.

As revealed by both microindentation experiments and naturally damaged shells, cracks tend to follow along the helical interfaces of the fibers, which rotate and nest volumetrically within the shell, hindering the catastrophic propagation of cracks through the shell thickness. This behavior leads to the generation of a much larger surface area per unit crack length in the thickness direction, increasing maximal applied loading energy which dissipates without destruction. Very same regime for the energy dissipation operates in biomineralized composites, such as bones, sponge spicules and mollusk shells. Such natural materials demonstrate excellent mechanical properties, especially considering their relatively soft/weak organic and stiff/brittle ceramic constituents. Similarly, soft/rigid combinations of the CG/UFG states of one metallic material and different kinds of materials can be created to realize advantages of architecture for SPD-processed samples. In the following subsections mechanical properties of both gradient and helical architected materials will be considered.

2.1.1. Mechanical properties of hybrid materials with gradient architecture

One promising materials design was suggested, based on natural structures known in plant and animal structures [38, 39]. The idea that soft layers incorporated into an otherwise strong material promises a good balance of strength and ductility. K. Lu [40] named an ideal architecture a NC metal (gradient nano-grained – GNG – structure) film adherent on a CG substrate of the same metal with a graded grain size transition between them. Such architecture can be achieved by surface mechanical grinding treatment [21]. This is a gradient architecture without a sharp interface between the NC film and the CG substrate (Figure 2.1 a). T. H. Fang [21] reported, that during surface mechanical grinding treatment a large fraction of grain boundaries in the top NC layer was derived from twin boundaries induced by high strain rate deformation. Wherein, in the subsurface layer deformed at lower rates, most of the grain boundaries were ordinary high-angle boundaries originating from dislocation structures [21].

This kind of elastically homogeneous but plastically gradient architected materials, may offer unusual mechanical response and provide a unique opportunity for revealing the intrinsic tensile plasticity of NC metals without strain localization. NC Cu film with a spatial gradient in grain size on a bulk CG Cu substrate demonstrated a large tensile plasticity and revealed deformation mechanisms, such as grain boundary sliding, that usually cannot be realized in conventional coarse grained materials [21].

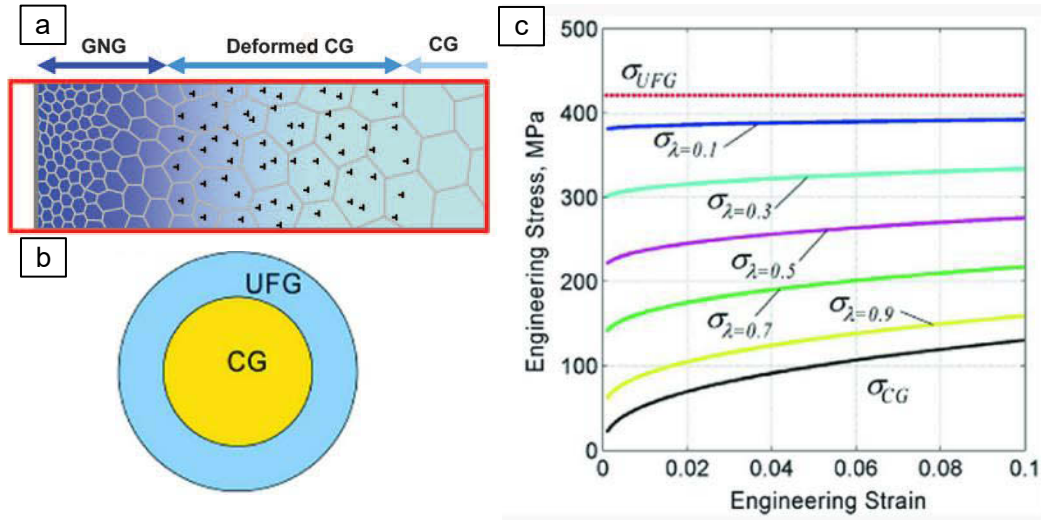


Figure 2.1 Schematic of the cross-sectional microstructure of the gauge section of the gradient sample consisting of a UFG layer (dark blue) and a deformed CG layer (blue) on a CG core (light blue) (from [21]) (a). Architected material of the ‘soft core/hard shell’ type: cross-section showing a CG core and an UFG sheath (b), stress-strain curves for various values of the volume fraction λ of the core material (c). Pictures b and c are taken from [41].

In a similar way, Beygelzimer et al. in [41] considered a cylindrical geometry consisting of a soft core enclosed in a hard shell as an architecture to increase the resistance of the UFG material to tensile overloads (Figure 2.1 b). This type of construction is typical for tubular bones, trees, as well as all metal structures subjected to surface hardening. It can be produced by severe plastic deformation through a number of processes, including ECAP of bimetallic samples [42], TE [43] and by HPTE [12].

The tensile overload sensitivity of such a structured material, can be evaluated as follows. Beygelzimer et al. in [44] suggested that the connection between both components of the structure is completely cohesive and that the tensile deformation of the sample is joint. It means that the deformation of the hybrid components occurs jointly, without differences in strain values and strain rates. These differences could result from the sliding of the components during the interphase surfaces. Then, the flow stress σ_s^* , in such sample can be expressed by the rule of mixtures:

$$\sigma_s^* = \lambda \sigma_s + (1 - \lambda) \sigma_{UFG}, \quad (2.1)$$

where λ denotes the volume fraction (or specific thickness) of the core material. The tensile stress-strain curves for materials with different λ values, calculated using Equation (2.1) are presented in Figure 2.1 c. Figure 2.1 c shows that this architecture is capable to provide tensile hardening kinetics intermediate between that of the inner soft and outer hard layers. The amount of hardening is determined by the ratio of the thicknesses of the soft and hard layers.

The experimental stress-strain curve of copper from [45] was used as the basis for the calculations. The experimental curve is approx. by the power law equation:

$$\sigma_s^* = A e_M^n \quad (2.2)$$

with the parameters $A = 320$ MPa and $n = 0.39$.

2.1.2. Mechanical properties of helically architected hybrid materials

The second type of the geometry of architected materials, which can be implemented by the HPTE method, is spiral architectural materials [12]. The idea of Bouaziz [22] to use the advantage of embedded strong corrugated lamellas during tensile test, when bending deformation of the lamellas occurs together with the tensile deformation of the matrix (Figure 2.2 a), is very close to the performance principle of helical architected plates in the nacre of a shell (a 3D model from [38, 46] that represents the hypothesized helical assembly scheme of curved fibrous building blocks is represented in Figure 2.2 b). Corrugated geometry could improve the tensile ductility of the matrix material due to artificial strain hardening associated with the "spring" embedded in the matrix (configuration of the corrugated strip tested in [22] is demonstrated in Figure 2.2 c). Such spring represents a wire corrugated along the axis with some period λ and radius R (Figure 2.2 b).

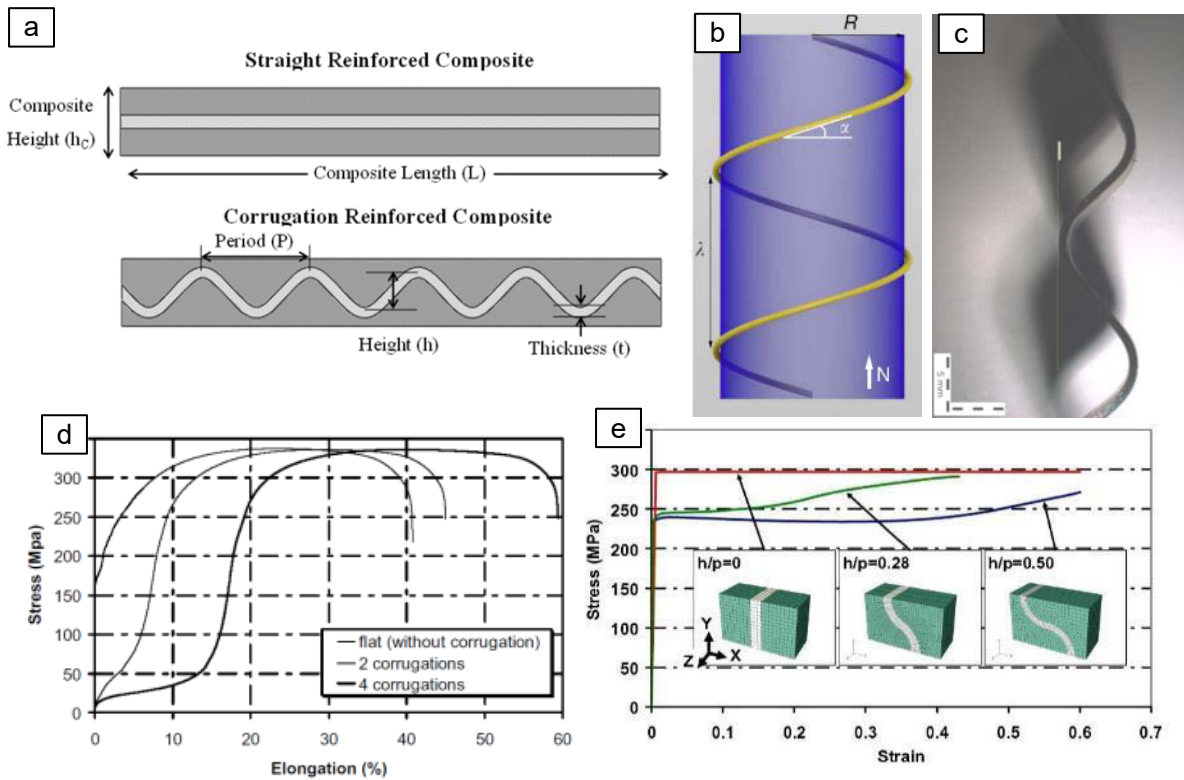


Figure 2.2 Depiction of straight reinforced composite (top) and corrugation reinforced composite (bottom) (a) [22]. Helical assembly scheme of curved fibrous building blocks (b) [38] and corrugated strips (c) from [22]. Stress as a function of elongation for flat and corrugated strips (d) [22]. Computed evolution of the flow stress as a function of strain for the perfectly plastic matrix strengthened by reinforcement with the different geometries of corrugation (e) [22]. Tensile force is along Y direction. Reprinted from [22] and [38].

The tensile behavior was experimentally verified for flat specimens of interstitial-free steel with two and four corrugations. The variation of the engineering stress as a function of elongation of such sample is drawn in Figure 2.2 d. The tensile curve is clearly divided into two stages. At the first stage in the beginning of the plastic deformation, the flow stress is low

and the elongation of the corrugated specimens occurs due to the unbending of the corrugations.

Subsequently, the flow stress slowly increases in the stage of unbending of the corrugated strips (first stage) and fast strengthening of material on the uniaxial tensile stage (second stage) occurs. Of interest are also the results of numerical simulation of uniaxial tension of samples reinforced with corrugated layers with various ratios between heights h and periods p of corrugations performed using the finite element method [22]. Y-axis tensile tests were simulated in the unit cell with the geometries shown in the inserts in Figure 2.2 e. Finite element modeling (FEM) was carried out under the assumption of plane deformation, and the volume fraction of reinforcement was 14%.

As seen in Figure 2.2 e, FEM results demonstrate a strong effect of the ratio between the amplitude and the wavelength (h/p) of corrugations on flow stress. The highest hardening rate was obtained for corrugations oriented perpendicular to the direction of the tensile force. Samples with corrugated layers demonstrated delayed strain hardening behavior when maximal strength was reached at strains of 0.4 and higher, depending on the layers architecture (Figure 2.2 e).

According to Considère's criterion, such behavior will delay the onset of plastic flow instability, thereby increasing tensile ductility, while SPD deformation provides increased strength of the matrix material [47, 48]:

$$\left(\frac{\partial\sigma}{\partial\varepsilon}\right) \leq \sigma, \quad (2.3)$$

where σ and ε are true stress and true strain, respectively.

An analytical approach to the same problem of stretching of thin and corrugated layers is discussed in [41]. In this work an opposite case was regarded, namely, thin planar layers of soft material (for instance, well annealed coarse grained) were embedded in a matrix with much higher strength (e.g. ultrafine-grained). Such layers have maximal strength in the normal direction and thus shear easily along the layers.

Let us consider a plate with a single thin layer as illustrated in Figure 2.3 a. For simplicity, plane strain condition is assumed. The matrix material surrounding the thin plastic layer is considered to be an element of an absolutely rigid body with the flow stress σ_s . For a thin layer, the condition $\frac{h}{b} \ll 1$ is used, where b is the plate width.

The flow stress σ_s^* of the matrix + soft thin layer composite was calculated in [44]. For the case when a thin layer is normal to the tensile direction along the axis 2, Equation (2.4) describes:

$$\frac{\sigma_s^*}{\sigma_s} = \frac{2}{\sqrt{3}} \left(1 + \frac{1}{2} \frac{b}{h}\right). \quad (2.4)$$

Obviously, it exceeds by far the flow stress σ_s of the base material of the matrix. An interesting corollary following from this result is that a softer layer is not detrimental to the tensile strength of the structure.

The composite with corrugated geometry is considered and named by authors of [44] an ‘artificial crystal’ with a thin layer inclined to axis 2 at non-zero angle α (see Figure 2.3 b) The flow stress for the artificial crystal was calculated as:

$$\sigma_s^* = \frac{2}{\sqrt{3}} \frac{\sigma_s}{\sin 2\alpha}. \quad (2.5)$$

Since the plastic elongation of the "artificial crystal" is provided exclusively by shear in the embedded layers, from geometric considerations, the deformation can be evaluated as:

$$\varepsilon^* = \frac{h}{H} \gamma \cos \alpha, \quad (2.6)$$

where the geometry parameter H is defined in Figure 2.3 b, and h is the thickness of the coarse-grained layer.

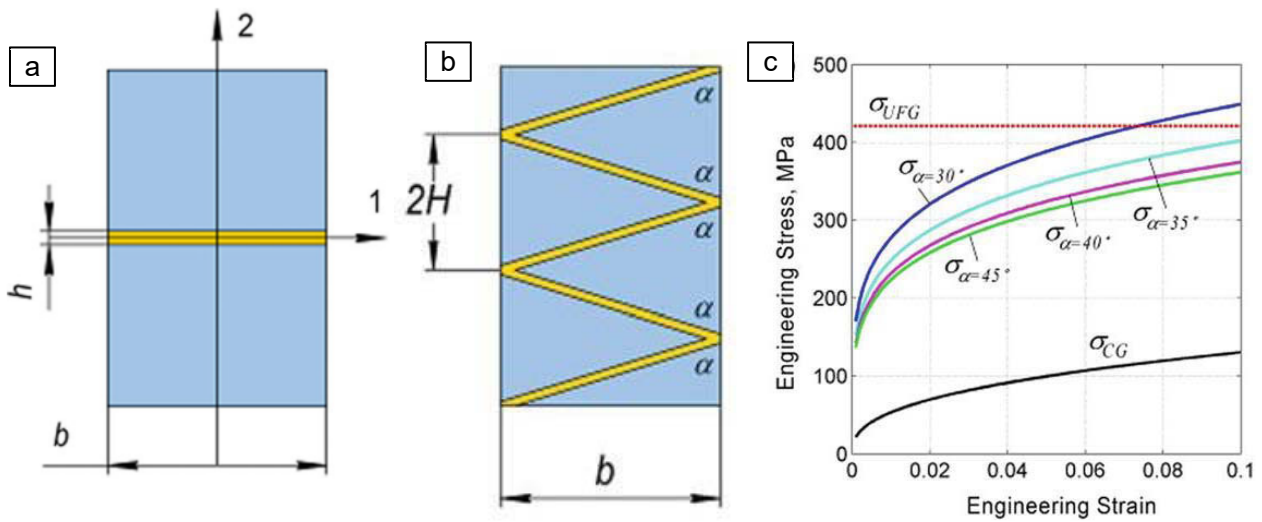


Figure 2.3 Tension of a plate with an embedded thin layer normal to the direction of tensile load (a). An architected material of the 'artificial crystal' type: schematic drawing (b), engineering stress-strain dependence under uniaxial tension for several values of the inclination angle α of the CG layers (c) [44].

Results of the calculation of the engineering stress-strain dependence under uniaxial tension for several values of the inclination angle α of the CG layers in the rigid UFG matrix are shown in Figure 2.3 c. As we can see, the smaller the angles α , the higher the hardening of the composite sample, and the closer its flow curve to that of the UFG matrix. The smallest strengthening and lower resulting strength was obtained at $\alpha = 45^\circ$. Obviously, this result is different to the result of Bouaziz [22], where a soft matrix and hard corrugated layers were considered. Thus, relations (2.5) and (2.6) derived by Beygelzimer et al. in [41] can be used for a simple description of the change in the resulting tensile strength of a composite specimen with corrugated layers. However, it can be easily rationalized, since the main flaw in Beygelzimer's description is the significant assumption that allow for a simple consideration of the mechanical behavior of the construction using mathematical formalism to develop simple analytical models of the mechanical loading. The main assumption is that friction between the matrix and reinforcing elements is neglected. This consideration is equivalent to considering a space-separated, independent zigzag reinforcement and a matrix with a notch that coincides with the notch. The shape of the notch corresponds to the shape of the reinforcing element. Significant forces arising from the interaction of the matrix and

reinforcing element, as well as the heterogeneous nature of their flow, make the Beigelzimer's approach too crude and do not provide accurate quantitative estimates of the resulting strength of hybrid materials.

With regard to the composite materials with a corrugated reinforcement geometry, it is of interest to determine the conditions when the use of a corrugated geometry improves the necking onset strain of the SPD-processed samples. In conventional composite materials, reinforcements have simple shapes like granules, fibers or laminae. Using severe plastic deformation, one can transform these simple shapes into complicated ones, for example, straight fibers can be transformed to helices. An attempt to prove this concept experimentally was undertaken in [49], where samples of commercially pure Cu reinforced with stainless steel fibers were deformed by torsion/extension to obtain a helical shape of steel reinforcements. Although the strain at torsion/extension was not significantly high to provide a significant grain refinement of the Cu matrix, the mechanical performance of such metal-metal hybrid samples showed an improvement of properties compared to the solid part without the helical fibers.

2.1.3. Strengthening mechanisms of pure metals and alloys subjected to SPD

Figure 2.4 demonstrates tensile test engineering curves of Cu processed by HPT (a) and rolled at liquid nitrogen temperature to a high value of strain (b) [50, 51].

The typical features of tensile test of SPD-processed material are rapid strengthening after increasing of yield stress (YS) and short interval of strengthening between the onset of plastic flow and ultimate tensile stress (UTS). This mechanical behavior is expressed by the absence or very short stage of uniform elongation and the apparent decrease of the flow stress up to rupture (Figure 2.4 a).

HPT, ECAP, TE of pure copper with high strain result in maximal increase of YS in the range of 410-430 MPa, which does not grow with further increase in the accumulated strain [52-56]. As seen in Figure 2.4 c, an increase in the yield stress is accompanied by a drop in plasticity at a hyperbolic curve, which is typical for all metals and alloys deformed at equal homologous temperatures [7]. This is the well-known "banana" curve indicating increasing of the strength along with decreasing of the material plasticity. Although there is considerable potential to increase the strength of materials by SPD, the maximum hardening is limited. Comparison of the strength characteristics of copper after various types of SPD processes at room temperature suggests the presence of saturation of the microhardness values [12], YS and UTS (Figure 2.5 a). HPTE, HPT and ECAP result in the microhardness saturation for pure copper, as well as for aluminum alloy [12, 57, 58] (see Figure 2.5 a, b).

It should be mentioned, that deformation temperature has significant influence on the size of grains and subgrains, which are formed during SPD. As it was clearly shown in the number of works of R. Pippan's group [23, 53, 59, 60], the maximum strengthening of SPD materials is determined by the deformation temperature and can be sufficiently described by the Zener–Hollomon parameter Z [61]

$$Z = \dot{\epsilon} \exp\left(\frac{Q}{RT}\right), \quad (2.7)$$

where the Zener–Hollomon parameter is the temperature-compensated strain rate and Q is the activation energy of deformation.

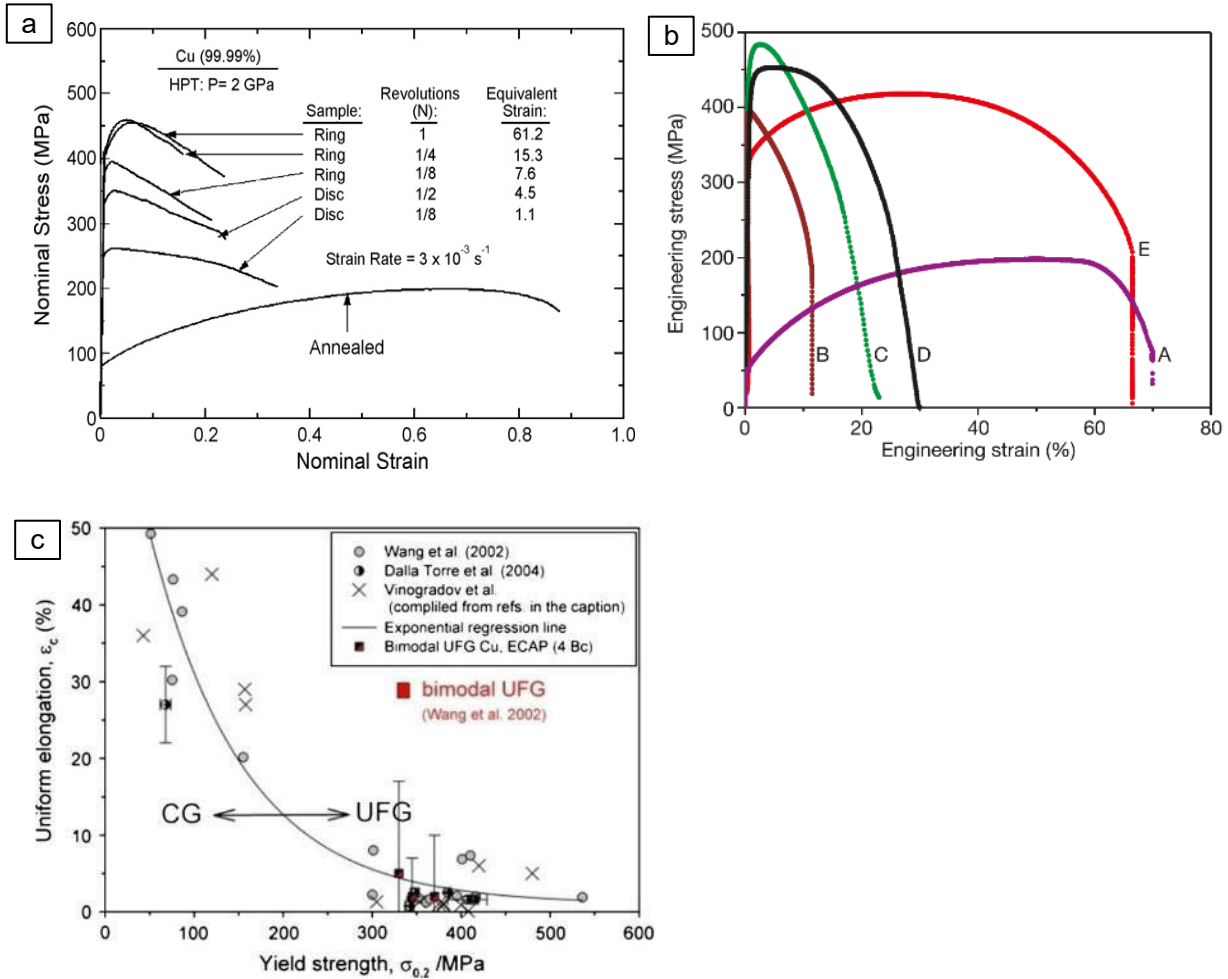


Figure 2.4 Typical engineering stress–strain curves for pure Cu subjected to SPD. HPT with different resulting strain (a) taken from [50]. Curve A – annealed coarse grained Cu; B – room temperature rolling to 95% (CW); C – liquid-nitrogen temperature rolling to 93%; D - 93% CW+180°C, 3 min; E – 93% CW+200°C, 3 min (taken from [51]). Relation between the yield strength and the uniform elongation in CG and UFG copper including the results for the samples with the bimodal structure produced by annealing for 1, 3 and 10 min at 200 °C after ECAP (c) (taken from [7]).

Saturation in strengthening of pure metals after SPD is accompanied by the saturation of a grain size, as for nickel subjected to HPT [53]. A reduction of grain size with increasing of strain in Figure 2.5 c demonstrated, that there are some differences in the kinetics of grain refinement at the stage, where grain size decreased, for crystal orientations with different orientation relatively torsion plane (TOR). Anyway, grain size saturation occurs in a narrow range between 0.35 and 0.40 μm [53].

The length of the uniform elongation stage depends largely on the temperature and rate of the SPD. Even short-term annealing can increase the uniform elongation stage, which leads, however, to a loss of material strength (compare curves C and D in Figure 2.4 b). The SPD-processed material has an ultrafine-grained and even nanocrystalline microstructure with a high fraction of high angle boundaries, which is very different to microstructure of cold worked materials [4, 58]. For example, SPD of copper deformed at a liquid nitrogen

temperature provides more significant strengthening via the activation of nanosize twins. This effect was demonstrated by Wang [62] for pure copper, subjected to rolling with high thickness reduction at low deformation temperatures.

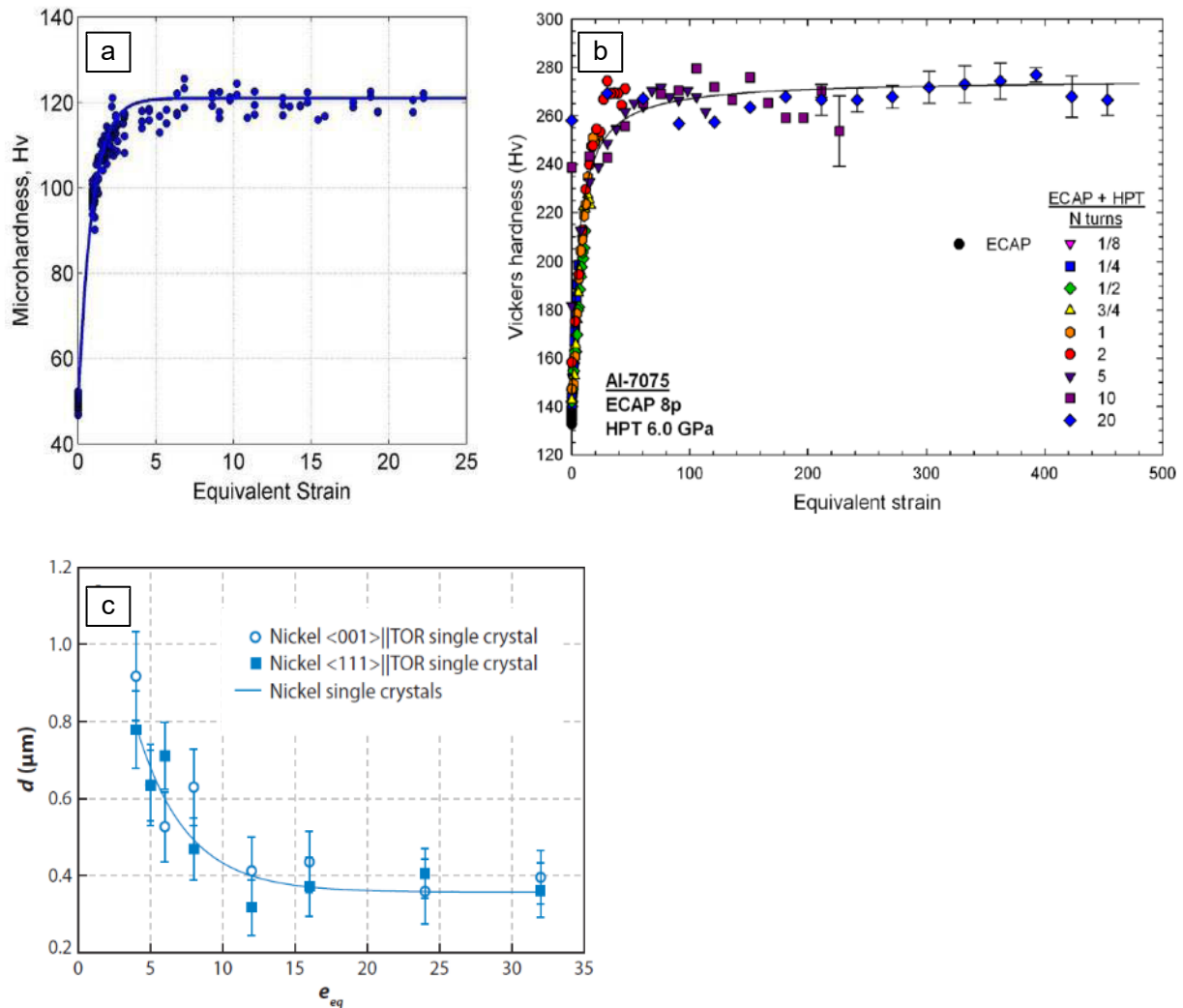


Figure 2.5 HV saturation depending on the accumulated strain during the HPTE (a) [12], HPT and ECAP (b) [58] processes. The grain size obtained from inverse pole figure maps in the axial direction parallel to the $\langle 111 \rangle$ and $\langle 001 \rangle$ crystal orientations, considering high angle boundaries as a function of strain (c) [53].

It should be mentioned, that the deformation temperature has significant influence on the size of grains and subgrains, which are formed during SPD. Wang et al. [52] argue, that NC and UFG materials tend to lose the work hardening capacity (left-hand side of Considere's criterion (2.3)) quickly on deformation owing to their very low dislocation storage capacity inside the tiny grains. Such a high-strength material is therefore prone to plastic instability (early neck formation), which severely limits the desired uniform elongation.

Generally, total strength of SPD-processed metals and alloys can be calculated by a simple arithmetic addition of contributions from different hardening mechanisms:

accumulation of dislocations (σ_ρ), Hall–Petch strengthening (σ_{H-P}), solid solution strengthening (σ_{SSS}), and second-phase particle strengthening (σ_{SPPS}) [4, 5, 63, 64].

The contribution of stored dislocations to the yield strength can be estimated using the Taylor equation [65]

$$\sigma_p = \alpha M G b \sqrt{\rho}, \quad (2.8)$$

where M is the Taylor factor, α is a constant, G is the shear modulus, b is the absolute value of the average Burgers vector, and ρ is the total dislocation density.

Strengthening due to the grain refinement can be estimated using the Hall–Petch relation [66]:

$$\sigma_{H-P} = \sigma_0 + k d^{-0.5}, \quad (2.9)$$

where σ_0 is the friction stress in the crystal lattice, k is a constant, and d is the mean grain size in the corresponding sample area. The microstructure of the SPD materials is complex, because both HABs and LABs are present in the microstructure. Therefore, it is not clear which grain boundaries (GB) misorientation threshold and grain size should be used in Equation (2.8). *In-situ* TEM study [67] had shown that in face centered cubic (FCC) metals with low and medium stacking fault energy, LABs with misorientations $\Theta > 3^\circ$ and special GBs provide effective barriers for the dislocation slip. Therefore, it can be assumed that the effective grain size d , in the Hall–Petch equation is equal to a grain size estimated with a misorientation threshold of 3° . The parameters σ_0 and k included in Equation (2.8), for a given material at a given temperature and a strain rate, are constant. In the presence of both subgrain and cellular structures, the general form of the Hall–Petch dependence does not change. In this case, the value of k usually becomes less, and the exponent approaches unity [68, 69].

Solid solution strengthening is complex, since the solute atoms can interact with dislocations by elastic, electrical, short-range and long-range interactions [70]. For a single-phase substitutional solid solution, the elastic interaction is the most important. This elastic interaction can be associated with local short-range mean normal stress. In the linear approximation, the elastic interaction is assessed as Peierls-Nabarro forces taking into account the atomic radius misfits and alloying element concentrations [70]. As a result, solid solution strengthening leads to an increase in the friction stress σ_0 .

Solid solution strengthening for single crystals was measured experimentally and, depending on the concentration of dissolved element in solid solution, a non-linear dependence of the σ_{SSS} was [71] as

$$\sigma_{SSS} = 4M c^{\frac{2}{3}} \quad (2.10)$$

where c is the concentration of the alloying element in the solid solution.

Second-phase particle strengthening can be calculated using the Orowan's formula for non-coherent particles [72]:

$$\sigma_{SPPS} = \frac{2\alpha M G b}{d_p \sqrt{\pi/6f}}, \quad (2.11)$$

where d_p – the second phase particles size and their volume fraction f are estimated experimentally. Subsequently, the original Orowan equation was refined taking into account the features of real metals. U.F. Kocks took into account the random arrangement of particles [73] and the effect of the so-called dislocation dipole [74]. The latter is related to an appearance of the stresses of opposite signs due to two edge dislocations with opposite Burger vectors comprising a dipole. These stresses reduces the stress of the dislocation bending around the particle.

2.2. High pressure torsion extrusion process

HPTE developed at the Insitute of Nanotechnology at Karlsruhe Institute of Technology [12, 75, 76] was used for the processing of samples. The combination of HPT [32] and conventional extrusion (CE) allows the realization of simple shear conditions and to create high hydrostatic pressure in the work piece. In this process, a large strain is accumulated in a single deformation pass. Similar to direct extrusion [77], in the HPTE technique, the material is extruded through two sectional containers: one container is stationary and the second can be rotated (Figure 2.6 a). HPTE is a new method, scaling up the HPT process (Figure 2.6 b), with a shear zone, confined in the narrow sample area between the upper and the bottom containers (Figure 2.6 a).

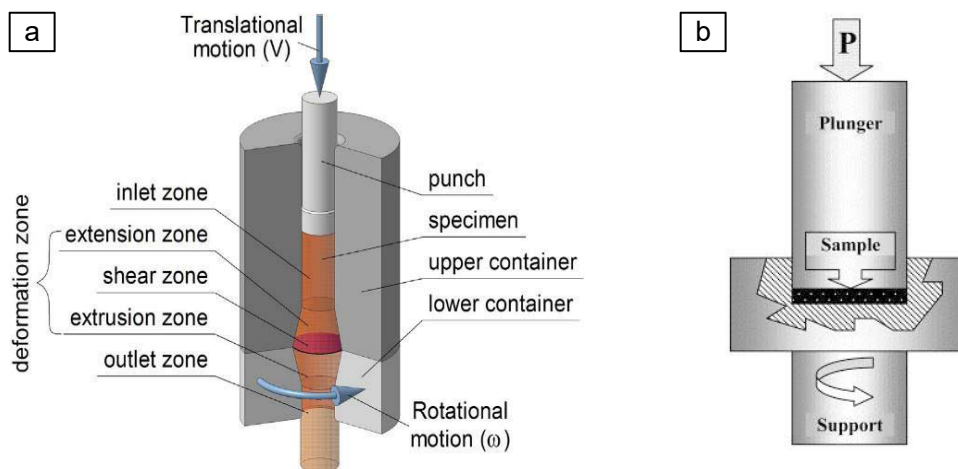


Figure 2.6 Schematic diagrams of the HPTE (a) and HPT (b) processes. Schemes are taken from [12] (a) and from [32] (b).

Additionally, it can be combined in a straight forward way with the Conform process [78] to obtain UFG samples with practically unlimited length. HPTE scheme was virtually implemented with Conform scheme by Hu et al. [79] and modelled by FEM.

The HPTE process includes the following steps. Initially, the channels of all containers must be completely filled with the material of a dummy billet, for example copper. This can be achieved by using a specially shaped sample or by plugging the outlet. In the applied design of the HPTE machine, the upper die is stationary, while the lower die rotates clockwise.

After the channels are fully filled, the plug can be removed and the extruded material provides the necessary back pressure for the next sample and ensures that the two containers remain completely filled during the process. In particular, the reduction of the channel diameter in the extrusion zone (Figure 2.6 a) and friction result in an appearance of the forces acting opposite to the extrusion direction and creating hydrostatic pressure in the shear zone. In this case, the sample is deformed by a punch moving at a speed v , and rotates with the lower container (with the rotation rate ω) in the shear zone located in the joining plane between the upper and lower containers. After the sample has been extruded to the full length of the punch, the process stops, the punch is lifted and the next sample is loaded into the container. Then the process starts over for the next billet.

2.2.1. HPTE processing of pure metals

It was originally assumed that using HPTE the entire length of the specimen is deformed by torsion as the specimen gradually passes through the shear zone [12]. However, more detailed studies and, in particular, finite element modeling have demonstrated that it is not completely true. R. Kulagin et al. obtained a significant difference in the distribution of strain along the sample height [76]. Simplified, it can be kept in mind that the top and bottom ends of HPTE samples are poorly processed. In the remaining volume of the samples, HPTE treatment results in changes of the microstructure as seen for example in pure copper [12] and aluminum [80]. It is noteworthy that after HPTE processing the grains of copper are not only noticeably refined, but also have equiaxed shape both in normal and longitudinal cross sections of the sample. The average grain size after HPTE are approx. 350 nm, and are very similar in both sections (normal and longitudinal) in the regions corresponding to the edges of the sample and at half of its radius (Figure 2.2 c and d). Omranpour et al. in [80] demonstrated that HPTE provides efficient grain refinement comparable to that after ECAP and HPT processes in aluminum. In the sample processed by HPTE, the mean grain size after an equivalent strain of ~ 20 was about of 0.7 μm . Further increase in strain via HPTE regime $v1\omega3$ did not lead to additional decrease of the grain size. This result is similar to that obtained by Cao and El-Danaf [81, 82], who reported that in an Al-1050 alloy processed by eight passes of ECAP, the mean grain size was approx. 0.7 μm . Further increase in strain for HPTE led to a saturation of the grain size at ~ 0.6 μm . Naderi et al. [83] reported the same grain size obtained at an equivalent strain of ~ 95 in AA1050 Al alloy processed by HPT at room temperature. It seems that the minimum grain size achievable in dilute aluminum alloys by SPD at room temperature is in the range of 0.6-0.7 μm , and can be obtained already at a strain of 10-20.

Comparing the results of microstructure observations and microhardness measurements of copper and aluminum after various SPD treatments, it can be concluded that the efficiency of HPTE in grain refinement is comparable to that of traditional HPT and even better than that of other SPD methods such as incremental high pressure torsion (IHPT) [84] and cycle expansion extrusion (CEE) [85].

Furthermore, the hardness values achieved after HPTE are only slightly (within the standard deviation) lower than those after other SPD treatments. Several reasons such as lower level of hydrostatic pressure at HPTE to compare with that at HPT [86, 87], influence

of the scale effect, adiabatic heating during the deformation, different purity of the material, etc.

In conclusion, HPTE is a very attractive method for the production of bulk samples of both pure metals and alloys, as well as hybrid materials, since it allows an implementation of simple shear conditions at high hydrostatic pressure not only in the peripheral regions, but also up to the center of the cylindrical rod.

2.2.2. HPTE processing of hybrid samples

In traditional industrial methods for the production of composite materials, various types of hardening elements (in the form of solid particles or powders) can be introduced into the billet. The control of the material flow during large plastic deformation can provide both mixing and homogeneous volume distribution, as well as create a desired internal distribution, i.e. reinforcement of the structure or creating special architecture inside the billet being processed [41]. Thus, SPD methods are tools for creating architected materials. The initial distribution of the introduced particles, which gives rise to the desired architecture, can be found computationally, solving the inverse problem, i.e. calculating the displacements of points distributed in the volume of the material during deformation. In certain SPD conditions, a strong bonding between the components parts can be provided, similar to that which occurs at friction stir welding. In this way, architected materials with good mechanical characteristics can be produced. A special type of architected materials are disks obtained by HPT, with embedded elements, arranged in a spiral [26]. Our interest in helical hybrid materials is due to the work of Bouaziz on the strength of specimens with corrugated iron wires inserted into a copper matrix as discussed in *Section 2.1.2* [22].

The schematical representation of the initial configuration of the hybrid sample with the wires embedded in the matrix prepared for the HPTE process is shown in Figure 2.7 a. Initially, fibers of the embedded material are aligned parallel to the axis of the sample prepared for the HPTE (Figure 2.7 a from [41]). Depending on the ratio between the speed of the translation movement of the punch and the speed of rotation of the bottom container, each wire is transformed into a spiral with a different number of loops per unit length (height) (Figure 2.7 b, c).

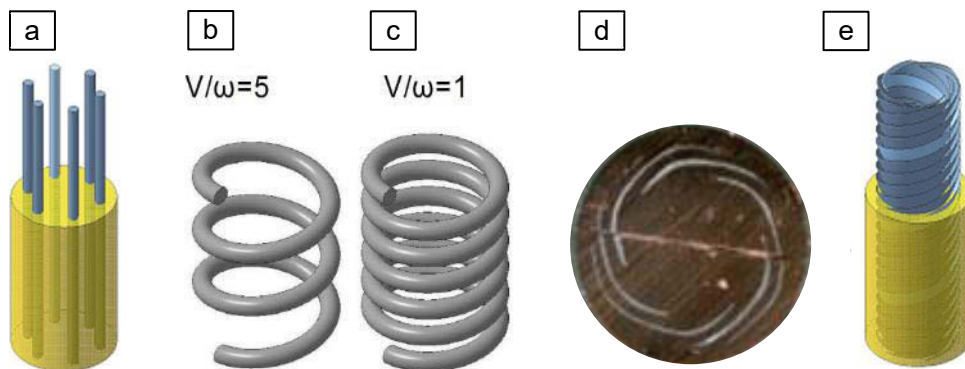


Figure 2.7 Formation of a spiral-shaped layered architecture by means of HPTE: initial arrangement of embedded fibers (a); various shapes of a resulting spring (b, c); an example of a spiral layer structure in the copper/aluminum system (d, e). The Cu matrix is colored with yellow and aluminum fibers (transformed to spiral Al sheets in the process of HPTE) are shown in blue. Pictures are taken from [41].

Using FEM simulation, it was shown that the initially round cross section of the samples after the HPTE process acquired a drop-like shape. This is confirmed experimentally on the cross section of the wires treated with HPTE (Figure 2.7 d), that the wires change the shape of the cross section as a result of HPTE. The original wire, which has a circle or ellipse in cross-section, is deformed into a tape, which has a drop-shaped cross section or a highly elongated ellipse, depending on the processing regime and the initial shape of the wire. (Figure 2.7 e) [41]. By combining matrix materials and embedded wires with different recrystallization kinetics and using post-deformation heat treatment modes, the desired combination of soft/hard layers can be created. Beygelzimer et al. [41] recommended to use embedded fibers of a metal, melting temperature of which is significantly lower than that of the matrix to create soft embedded elements in the hard matrix using post-deformation annealing. This can be rationalized in the case of Al fibers in Cu matrix presented in the Figure 2.7 [41]. Therefore, the investigation of the recrystallization kinetics is an important part of the study of materials subjected to HPTE.

The creation of hybrid materials is a promising direction in the development of new materials. Thus, the incorporation of new structural elements into a solid is possible by mixing ready-made powders, which must be mixed, deformed and bonded to the desired structure. The SPD community has already achieved great success in the production of UFG alloys by mechanical alloying, as exemplified by the production of multicomponent aluminum alloys with a multilayer structure by ARB [88, 89].

Another example is the process of accumulative press bonding of composites with a nanostructured metal matrix [90]. Forming thin layers from host-doped materials using HPTE is a potential way to produce UFG materials with embedded thin layers (can be seen in Figure 2.7 d). Thin layers of alloyed material have a developed surface and adhere well to the matrix. Therefore, conditions for diffusion of the doped component into the matrix can be provided.

2.3.Evaluation of strain in HPTE

2.3.1. Analytical equation for the calculation of strain in HPTE

The principal scheme of the HPTE technique is given in Figure 2.8 a. The conical shape of the hollow space in the containers allows to create the required level of hydrostatic pressure in the shear zone. The strain e accumulated in the sample after one pass can be controlled by adjusting the ratios of the sample diameters ($D2/D1$ in Figure 2.9 a), final diameter reduction for the back pressure ($D1/D3$) and processing velocities v / ω of the instruments in accordance with Equation (2.12) (from [12]):

$$e = 4 \ln \frac{D2}{D1} + 2 \ln \frac{D3}{D1} + \frac{\omega \cdot R}{\sqrt{3} \cdot v} \frac{D2}{D1} \quad (2.12)$$

Each billet is extruded via two containers, the top and the bottom (Figure 2.8) using HPTE machine (Walter Klement GmbH, Daxenberg, Austria). The employed HPTE machine

equipped with a hexagon configuration of the die (Figure 2.8 b) has provided opportunities to obtain large strains in copper, aluminum and copper/aluminum samples [12].

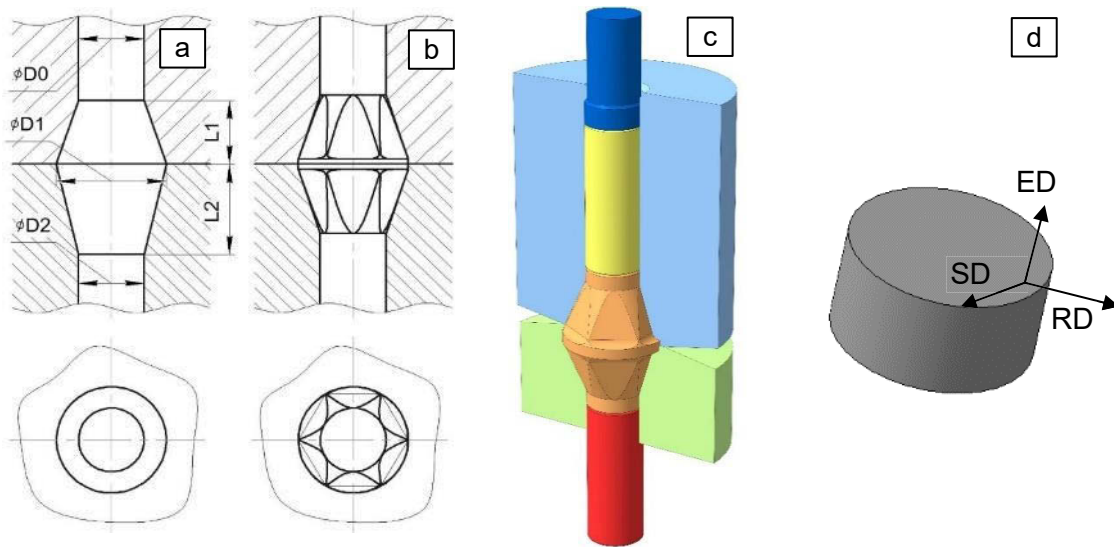


Figure 2.8 Detailed drawing of the HPTE tool with smooth cone surfaces (a), 6-wrench-shape surfaces (b) and 3D image of a billet inside HPTE die (c) [12]. External directions are shown as radial direction (RD), extrusion direction (ED) and shear direction (SD) (d).

In this machine the top die is stationary and the bottom one can rotate. The HPTE process includes the following steps: in the beginning, the channels of all containers were filled completely using two dummy-billets. Dummy-billets acted as a plug and ensured that the two containers remain fully filled during the process. The reduction of the channel diameter and friction result in forces acting opposite to the extrusion direction and creating a hydrostatic pressure in the shear zone. Therefore, the specimen is deformed by the action of the punch (moving at speed v) as well as the containers (the bottom one is rotating at speed ω). Once the specimen is extruded to the full length of the punch, the process stops, the punch is lifted and the next specimen is loaded into the container, after which the process starts again. Consequently, the entire length of a specimen is deformed, as a specimen gradually passes through the shear zone.

A simple analytical consideration of the HPTE process given in [12] allows to calculate the von Mises strain using Equation (2.12) for simple cone-shape dies. The calculations were performed at three points located in the cross section of the sample at different distances from the center of the billet, subjected to the HPTE deformation using the operating parameters $vX\omega Y$ presented in Table 2.1.

The simplest form of the HPTE channels is a truncated cone, as shown in Figure 2.6 a. The channels of the expansion and extrusion containers have a diameter $D1$ in the plane, where they meet. The strain that accumulates in the specimen after one pass can be controlled by adjusting the ratio of specimen diameters and the rate of translational and rotational movements.

The analytical formula (2.12) assumes that expansion-extrusion and torsion deformations are additive. The strain calculated in this way is directly proportional to the value ($R = D2/2$), i.e. $\epsilon \sim R$. The analytical formula has many rough assumptions that do not

take into account important process factors, such as friction and sliding of the billet inside the HPTE tool, hardening of the billet material, etc. A computer simulation of the HPTE process using the finite element method (FEM) can allow as to calculate the strain distribution more accurately.

Table 2.1 Regimes of HPTE process and respective von Mises strains for cone-shape dies.

Process ID	v , mm/min	ω , rpm	N^*_c	von Mises strain		
				center	mid_rad	edge
$v10\omega0$	10	0	0	0.9	0.9	0.9
$v18\omega1$	18	1	1.9	0.9	1.6	2.3
$v10\omega1$	10	1	3.5	0.9	2.2	3.0
$v6w1$	6	1	5.9	0.9	3.0	5.2
$v1\omega1$	1	1	35.0	0.9	13.8	22.4

* N_c – number of revolutions performed by any point of a billet during HPTE processing of this billet.

Kulagin et al. in [76] presented a simple mathematical model of the deformation behavior of a rigid-plastic material during HPTE. The model can predict the distribution of strain along the height of the sample, when a slippage of sample along the container walls occurs. It also predicts the magnitude of equivalent strain of the material given the slip of the billet. HPTE process in [76] is represented with a rotation of the upper and lower blocks with relative angular velocities ω_1 and ω_1 .

$$L_1 \frac{w_1}{\sqrt{v^2 + (w_1 R)^2}} = L_2 \frac{(w - w_2)}{\sqrt{v^2 + ((w - w_2) R)^2}}, \quad (2.13)$$

where the heights of the upper and lower holding elements 1 and 2 are denoted L_1 and L_2 , respectively. Equation (2.13) describes the change in angular velocity of the points along the height of the billet during the HPTE processing. However, both analytical ratios (2.12) and (2.13) don't allow to take into account all the details of the holding element geometry implemented in the HPTE.

2.3.2. Finite element modeling of the HPTE processes

At present, some results of the finite element modeling of the deformation process during HPTE are available. Calculations of strain at HPTE with simple conical dies were performed in [12]. The obtained strain distribution for the two HPTE regimes $v10w1$ and $v1w1$ gives results that are quite close to the values which can be determined using Equation (2.12) (see Figure 2.9). The authors [12] proposed that the discrepancies between the results obtained by FEM and by the analytic Equation (2.12) can be explained by the fact that the actual die geometry and friction conditions are taken into account in the FEM analysis. Nevertheless, in some points the deviations of the FEM calculations from the analytical ones reached 25-30% (Figure 2.9), which was large enough to talk about a significant discrepancy of the different calculated values.

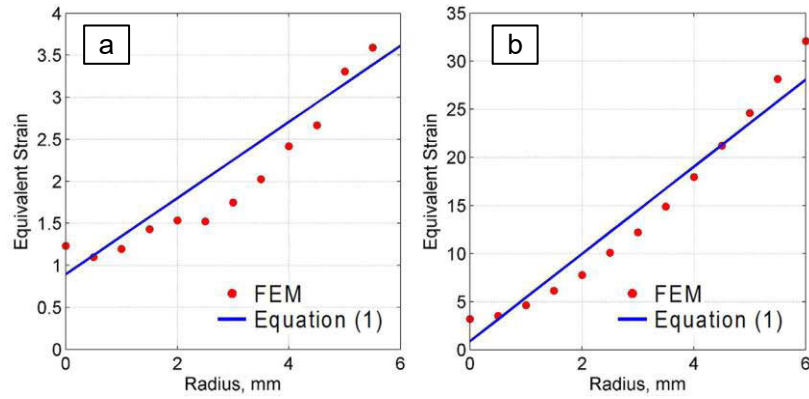


Figure 2.9 Equivalent strain in dependence on the radius calculated using FEM and Equation (2.12) for $v_{10}w_1$ (a) and $v_{1}w_1$ (b) regimes. Plots are taken from [12].

Kulagin in [76] performed FEM simulations of the HPTE process with the real geometry of the die with holding elements. The results of these simulations are shown in Figure 2.9 a, b, which demonstrated that the resulting strain depends on the geometry of the holding elements, namely, variation of their height, which also takes into account the analytical Equation (2.13). It was found that, as the height of the holding elements increased, the amount of strain decreased, and the height of the uniformly deformed part of the billet increased [76]. Hu et al. in [79] simulated HPTE in combination with the Conform process. The FEM calculation [79] shows that the strain is distributed gradually along the radius of the cylindrical billet, i.e., in general, combining the Conform process with the HPTE does not change the final strain distribution. As a rule, in the sample areas from the center to the middle of the radius, the strain increases insignificantly, while at greater distances from the center the strain grows exponentially. In addition, the total strain in [79] was calculated as the arithmetic sum of the strain in the Conform and HPTE processes. The contribution of the HPTE treatment was calculated using Equation(2.12). The tendency of the deformation to increase from the center towards the edge calculated by both approaches is the same (linear).

Based on the existing results of strain distribution under various HPTE regimes, it can be concluded that the geometry of the holding elements can significantly affect the resulting strain distribution in the sample and strain rate. FEM allows to describe the plastic flow of the billet during HPTE process, taking into account the real process conditions, such as the presence and type of lubricant (friction conditions), deformation temperature, hardening of the billet material, etc. This requires experimental verification of the calculated data. The role of the inhomogeneity of the lubricant distribution and, consequently, friction on the inner surface of the tool remains unclear. Friction conditions can vary not only on the side, top and bottom surface of the billet, but also can differ in the top and in the bottom holding elements. The deformation temperature and the related hardening rate of the billet material also should be taken into account.

3. Materials, samples preparation and investigation methods

In the third chapter the techniques of samples preparation, HPTE processing and characterization methods such as electron microscopy, X-ray techniques and mechanical testing are presented. In general, the effect of HPTE on the structure and mechanical properties of pure copper and hybrid samples was investigated in the thesis. The HPTE regimes for each kind of material and deformation temperature are specified and experimental validation path for the finite element modeling is described.

3.1. Choice of materials

The choice of materials for hybrid samples was directed to the main goal: to extend the uniform elongation stage of the UFG matrix. Based on the results of Bouaziz [22], iron wires in Cu/Fe hybrid samples provided significant increase of the resulting flow stress to compare with flow stress of the copper matrix during tensile test, in spite of the difference in the cross section area of the matrix and wires. Therefore, Cu/Fe combinations are chosen as the main object for investigations.

A Cu/Fe pair corresponds to a hybrid of a soft matrix and a hard wire. However, to study the process of plastic deformation of a material during HPTE, it is advisable to use easily deformable wires as indicators of the plastic flow of the matrix. For such purpose, Cu/Al hybrid samples consisting of a hard copper matrix and soft aluminum ductile (at processing temperatures) wires were chosen. Some HPTE regimes have already been experimentally verified for the simplest Cu/Al hybrid configurations [12] and can be used as the basis for the development of technology for obtaining more complex configurations.

Also, the results of the production of the Cu/Al hybrids can be helpful to develop technical regimes of the more complex HPTE processing of the Cu/Fe hybrids. Chemical compositions of the used materials are given in Table 3.1.

Table 3.1 Chemical composition of metals (in wt. %).

Metal	C	Si	Mn	Fe	Al	Cu
Copper	-	-	-	-	0.4-0.6	balance
Aluminum	-	0.2-0.3	0.01	0.1-0.2	balance	-
Iron	0.09	0.13	0.36	balance	-	-

To analyze the mechanisms of hardening during tensile testing, the developed mathematical tools should be applied to the prepared hybrid samples. In particular, equations (2.5) and (2.6) were developed for a combination of a hard matrix and soft embedded layer (Figure 2.3 b). Compatible deformation of hard and soft constituents was one of the main provisions in the development of a model for strengthening of hybrid materials in [41]. Compatible deformation requires a very good joining of the contact surfaces of both materials.

3.2. Initial sample design and manufacturing

Helical shape of the embedded wire after the HPTE process (Figure 2.7 b, c) executes the same function as the corrugated wire in experiments of Bouaziz [22]. For the proper tensile tests of the obtained hybrid materials, reinforcements should be completely embedded in the gauge part of the tensile specimen. Next, the helical configuration should maintain the axial symmetry geometry in the uniaxial tension conditions and to not change it to the twisting of the gauge.

According to the requirements for the deformation conditions of hybrid samples, samples with very good junction of the embedded elements and the matrix should be prepared. In the SPD process, there is a high probability of the formation of a "dead" deformation zone in case of poor connection between two metals in hybrid and, as a consequence, development of incompatible deformation. To provide the complete fitting of the interfaces between the wire and the matrix, a conventional extrusion of Cu/Al and Cu/Fe hybrids at temperatures, allowing deformation without cracking was performed. HPTE machine was equipped with specially designed matrix for the conventional extrusion with reduction of the diameter of the billet to the diameter that is employed in the HPTE process.

3.2.1. Preparation of samples of pure metals for HPTE

First of all, bulk samples of pure Cu were processed by HPTE at room temperature. Copper with commercial purity (Table 3.1) was chosen as a matrix material for hybrid samples. Since at room temperature iron has insufficient deformability at high strains necessary for the formation of helical shape, it was decided to perform deformation at elevated temperature.

Commercially pure copper samples with a chemical composition given in Table 3.1, were machined, extruded from diameter 20.0 to 11.8 mm and annealed for two hours at 600 °C, then water quenched to obtain a CG microstructure.

3.2.2. Preparation of hybrid samples for HPTE

Al and Fe wires with initial diameter of 2 mm were inserted in the channels with a diameter of 2.1 mm which were previously drilled in commercially pure copper samples (Figure 3.1 a). A clearance of 0.1 mm between the hole and wire diameters was necessary to avoid scoring and scratching the contact surfaces during assembly. Before assembly, the surfaces of the wires and holes were degreased with acetone and dried with compressed air. In order to create a proper joining of both materials, Cu-Al billets had been extruded at 250 °C, and Cu-Fe – at 400 °C from the initial diameter of copper samples $D_0 = 20.0$ mm to the diameter of 11.8 mm (b). Deformation temperatures were selected in accordance with technical recommendations for direct extrusion of copper [91] and aluminum – 250 °C [92], as well as copper and pure iron [93] – 400 °C. To ensure the specified temperature conditions for deformation, the deformation tool was equipped with built-in heating elements. The workpieces were heated inside the die for 5 minutes before deformation.

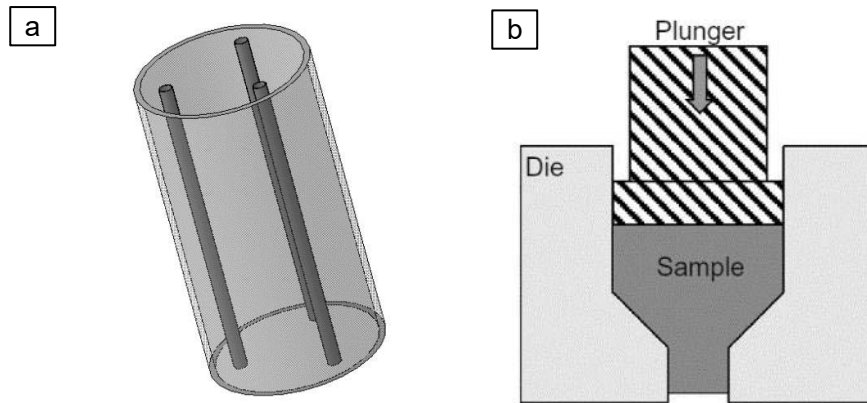


Figure 3.1 Scheme of hybrid samples preparation: assembling of matrix and wires (a); direct extrusion (b).

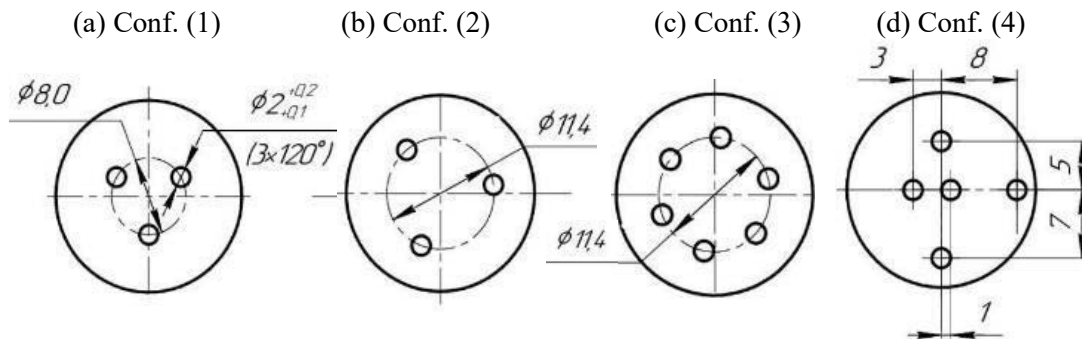


Figure 3.2 Drawing of initial configurations of hybrid Cu samples before CE processing. Diameter of each sample is 20 mm.

Initially four configurations with wires (Figure 3.2 a-d) were prepared. The first and the second configurations were designed for the tensile tests HPTE-processed samples. The third was prepared to create a high density of embedded material layers along the billet height required to analyze configurations with a small number of turns. The fourth configuration was used to study the material flow at different distances from the center of the wire at HPTE. The configurations (1) and (2) combining Cu-matrix and three iron wires (chemical composition in Table 3.1) were prepared according to the similar procedure as for the Cu-Al hybrid samples described above (configurations (1) and (2) in Figure 3.2), with the only difference that 20 mm samples were extruded at 400 °C.

The sample configurations prepared in this way are shown in Figure 3.3. After extrusion, initial diameter of wires of 2.2 mm was reduced to 1.2 mm (Figure 3.3 a-d). Careful inspection of the joints between the Al wires and Cu matrix using optical and scanning electron microscopy did not reveal any flaws between the two materials (Figure 3.4), and EDS analysis showed a sharp transition from Cu to Al (Figure 3.4 b). The as-prepared hybrid samples were cut into 35 mm pieces for the subsequent HPTE.

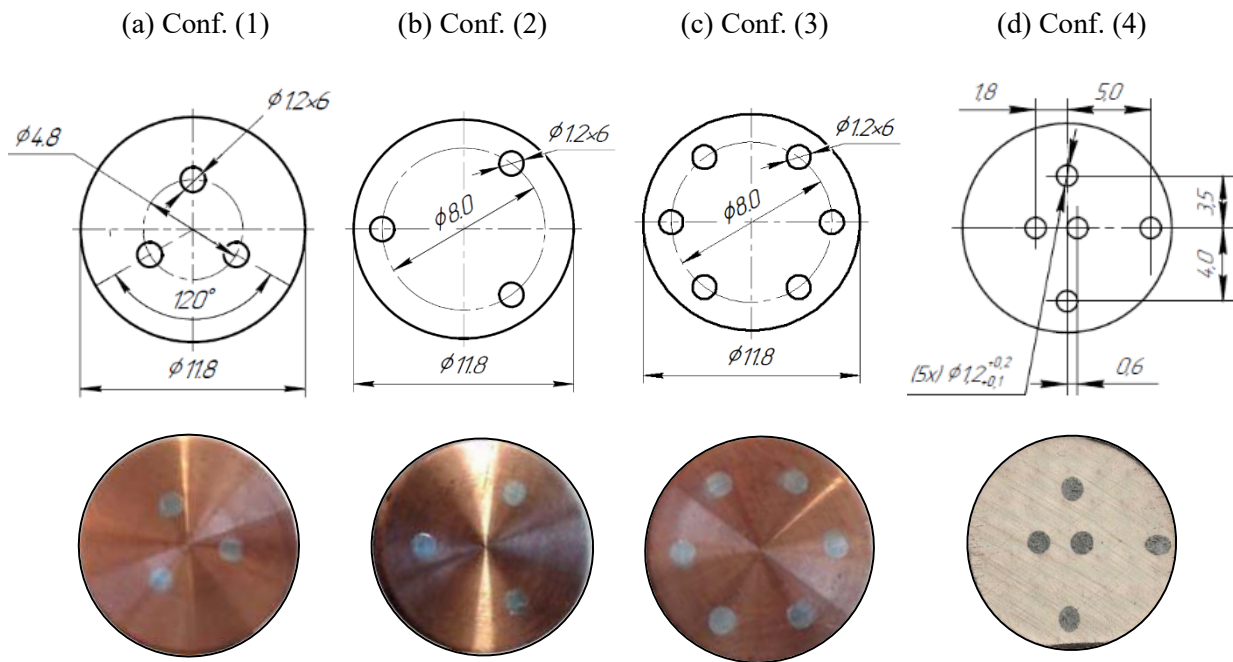


Figure 3.3 Images of the cross sections of the billets prepared for the HPTE.

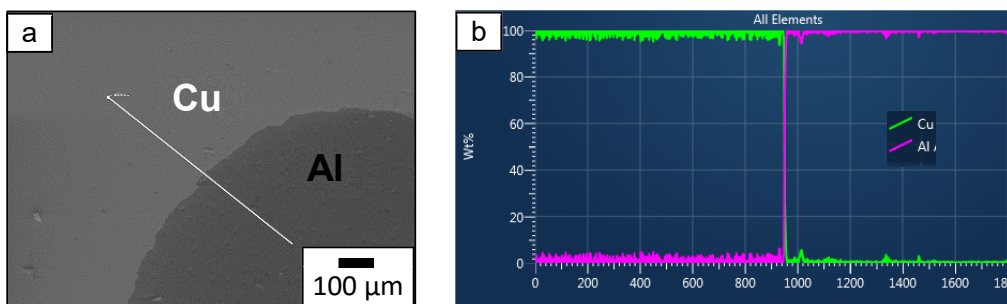


Figure 3.4 Interphase boundary in the Cu-Al hybrid samples after CE. Secondary electron images (a), EDS signal along the scanning lines (b).

One sample of each configuration was cut in transversal and longitudinal sections to confirm good joining. It was confirmed that CE at 250 °C of Cu-Al and at 400 °C Cu-Fe with extrusion rate of 10 mm/min provide joint deformation both of copper matrix and the second component. Macroscopic cracks and flaws were not revealed at the interphase boundaries. The interphase Cu-Al boundary looks serrated in SEM images (Figure 3.4 a). Serrated interphase boundaries indicate joint deformation of the metals during CE.

3.2.3. Processing of pure copper

Pure copper was subjected to HPTE in various $vX\omega Y$ (X, Y – are translation and rotation velocity values, respectively) regimes, including the $v18\omega1$, $v10\omega1$, $v6\omega1$, $v1\omega1$ regimes and $v10\omega0$ regime that employed deformation without rotation of bottom container [12]. The first cylinder-shaped copper sample with initial diameter of 11.8 mm and a length of 35 mm was used for the creation of the back pressure before HPTE processing. The next and following copper samples were processed using the HPTE die shown in Figure 2.8 b and molybdenum disulfide (MoS_2) as a lubricant to facilitate the extrusion process.

The pre-heating of the tool for the processing at 100°C was carried out during three hours before deformation to ensure constant temperature conditions during processing. Heating was realized by six electric resistance heating elements placed inside the HPTE die as shown in Figure 3.5.

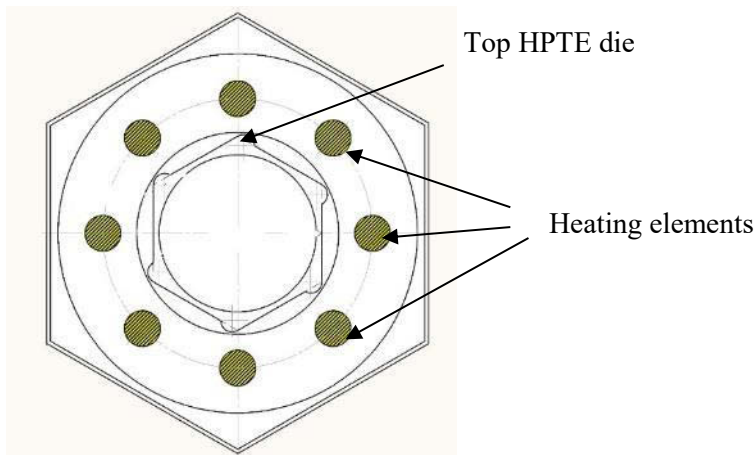


Figure 3.5 Scheme of the heating elements (marked by shaded areas) location in the top part of the HPTE machine. Top view.

After processing, the copper samples were cooled in air.

3.2.4. Processing of hybrid samples

HPTE regimes applied for the processing of hybrid samples were $v18\omega1$, $v6\omega1$ and $v1\omega1$ (Table 3.2). Regimes $v18\omega1$ and $v6\omega1$ were employed to get helical geometries with different number of loops and different ratio between the wavelength p and amplitude h . As mentioned above, Bouaziz [22] demonstrated that an increase in the strain hardening rate as a function of the plastic strain can be obtained depending on the reinforcements architecture.

The processing temperature was chosen taking into account the deformability of copper, aluminum and iron.

Temperatures of HPTE deformation of Cu-Al and Cu-Fe samples of 100°C and 180°C (see Table 3.2), respectively, provide the necessary conditions for the compatible deformation of hybrid samples.

Table 3.2 Regimes of HPTE process employed for processing of the hybrid samples.

Materials	Process ID	v, mm/min	ω , rpm	T, °C
Cu-Al	v18 ω 1	18	1	100
	v6 ω 1	6	1	100
	v1 ω 1	1	1	100
Cu-Fe	v18 ω 1	18	1	180
	v6 ω 1	6	1	180
pure Cu	v18 ω 1	18	1	180
	v10 ω 1	10	0	25; 100
	v6 ω 1	6	1	180
	v1 ω 1	1	1	25; 100
	v10 ω 0	10	0	25; 100

Processing of the Cu/Fe hybrid samples at 100 °C led to the rupture of all iron wires. Consequently, the deformation temperature was increased to 180 °C. Macrodefects, such as cracks, leaks, sagging, galling, etc., were not found on the surface of all processed samples.

3.3. Characterization methods

Samples after HPTE were characterized using methods for the macro- and microstructure analysis and for the measurement of tensile properties of the large-scale samples and microhardness distribution. Generally, macrostructure of the hybrid samples was investigated to define resulting configurations of the wires after deformation. Microstructure was evaluated in the processed samples of pure copper and hybrid samples.

3.3.1. General characterization

In order to analyse the strain state in the billet directly in the deformation zone (in the following referred as intermediate processing), the deformation process was stopped, when the half of the billet was processed. Corresponding 3D image of the billet in this position is shown in Figure 2.8 c (orange billet). Subsequently, the HPTE die was disassembled. In order to track the marker wire shape and location, the resulting samples as well as the samples after completed HPTE were sectioned as follows. Billets were cut through the extrusion direction (ED in Figure 2.8 d), and as-obtained surfaces were grinded and polished with subsequently reduced grain (diamont) size of the polishing suspension to obtain mirror-like surface. Optical images of the as-prepared and processed sample surfaces were recorded using Keyence VH-Z100R fixed in VHX-550 system microscope. SEM Zeiss LEO1530 operating at 20 kV and equipped with secondary electrons (SE) detector was used for microstructure investigations.

Other samples of pure Cu and Cu with inserted Al and Fe wires were fully processed by HPTE (in the following referred as full-height processing), and then the resulting configuration was analyzed, namely, counting of the number of the wire loops N_H at a full height of the billet. The N_H value was counted as a number of wire exit points on the longitudinal section of the sample (diametral section of the sample along the ED in the Figure 2.8 d).

Samples processed by HPTE were cut in the extrusion direction through the diameter (ED on the Figure 2.8 a) and transversal section perpendicular to ED in the middle of the height of the rod. Surface was grinded and polished with subsequently reduced particle size of the polishing suspensions to obtain mirror-like surface. Full-size images of HPTE-processed samples were obtained using a Keyence VH-Z100R camera attached to a VHX-550 optical microscope system.

3.3.2. XRD tomography of hybrid samples

For the full-size non-destructive characterization of the 3D geometry of the hybrid samples before and after HPTE, X-Ray tomography measurements in collaboration with Prof. L. Toth at the University of Lorraine were performed.

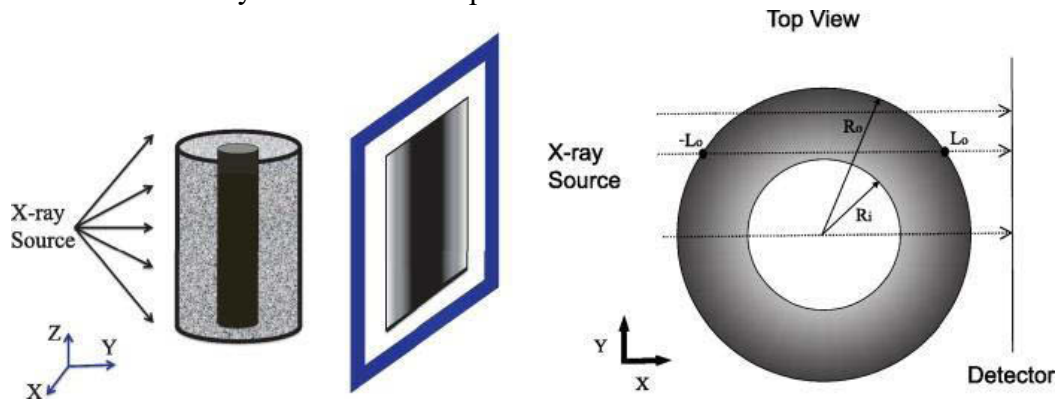


Figure 3.6 Schematic of the radiography is represented from [94].

The setup is mounted in X-ray computer tomography (CT) scanner Easytom Nano model from RX-Solutions equipped with a 160 kV X-ray tube with a spatial resolution of up to 0.35 μm . The principal scheme of scanning is presented in Figure 3.6. X-ray CT projections of a stationary object at different angles are obtained. For example, more than 3000 images along Y direction are necessary to reconstruct a 3D image. The scanning process takes about 2 h to build a 3D computed object using the Radon transform. Resulting 2D slices of the longitudinal sections were reconstructed into 3D images and segmented using a Dragonfly object recognition system (non-commercial edition).

3.3.3. Methods for microstructural characterization

3.3.3.1. Metallographic sample preparation

The HPTE-processed samples were sectioned both in the transverse (normal) and longitudinal directions. Thin plates with the thickness of $\sim 1.0\text{-}1.2$ mm were cut by Struers Minitom disc saw using water base coolant.

The plates were subsequently thinned mechanically down to $\sim 100\text{-}150$ μm , grinded by SiC papers (from 140 to 4000 grit size) and polished with Struers DP suspensions on the cloths using a Struers Rotopol-25 machine. Mechanically polished disks with a diameter of 3 mm were cut from the thinned plate as shown in Figure 3.7. The 2×3 mm rectangular shaped samples for SEM-EBSD study were cut such that their long side was parallel to ND to unambiguously determine their orientation related to the deformation geometry. Orientation

imaging microscopy (OIM) maps were collected on the 3 mm disk-shaped samples. The samples were cut at three different locations, i.e. in the center, at the middle-radius (~2.7 mm from the sample axis), and at the edge (~4.5 mm from the sample axis) of the HPTE-processed sample (Figure 3.7).

A similar layout was used for the diametrical longitudinal section, where the central specimen was cut at half of the sample height.

Prepared copper and aluminum samples were polished electrolytically for further transmission and scanning electron microscopy studies. The electropolishing was conducted using the Tenupol-5 twinjet polisher, with the standard Struers D2 solution for copper and A3 solution for aluminum at the voltage of 20 V. Final polishing was performed using GATAN PIPS system to remove the surface oxide layer.

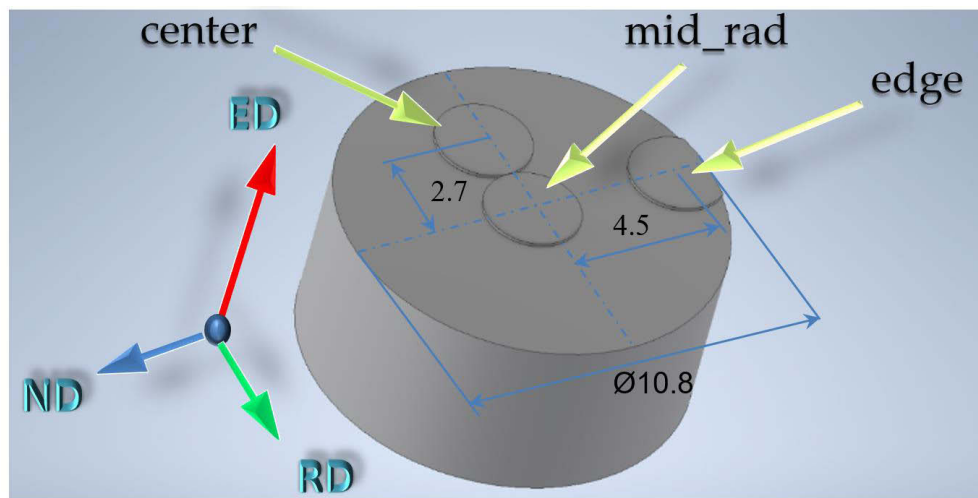


Figure 3.7 Scheme of the samples location for EBSD study on the cross-section of the HPTE-processed rod.

3.3.3.2. Scanning electron microscopy

A Zeiss LEO1530 scanning electron microscope (SEM) coupled with energy-dispersion EDS spectrometer (X-Max 50, Oxford Instruments with a large area analytical Silicon Drift Detector) was used for the elemental analysis of the samples. All EDS measurements were performed at an acceleration voltage of 20 kV in at least three different samples sites to confirm the compositional homogeneity. The sample composition presented in this work is within 2 at.% of standard deviation.

The microstructure of the polished samples was examined by means of electron back scattered diffraction (EBSD) technique using Zeiss Auriga60 SEM, equipped with an EDAX-TSL EBSD detector. The EBSD study was carried out at an acceleration voltage of 20 kV using 140 μm aperture, at the working distance of ~ 8 mm. Scan step was defined as $D_{\text{av}}/8$, where D_{av} is an average (sub)grain size of investigated sample as suggested by Humphreys et al. [95].

The EBSD method allows to determine local phase and crystallographic orientation of the sample from the electron back scattered pattern (EBSP) [96]. The EBSP formation scheme is illustrated in Figure 3.8 a. Electrons that travel along a crystallographic plane trace generate Kikuchi bands which form EBSP. These patterns are registered on the phosphorus screen connected to the charge-coupled device - camera (Figure 3.8 b). The Hough transform is

applied to detect the bands in EBSD, to enhance its quality and to compress the image. A set of pixels forming a line can be described in terms of a pair of Hough parameters corresponding to a line in the image space. Thus, the problem of finding a band (denoted by a linear set of high intensity pixels) in the diffraction pattern is reduced to find a point of high intensity in the Hough transform. An EBSD image, the corresponding Hough transform, and the detected bands are shown in Figure 3.8 c.

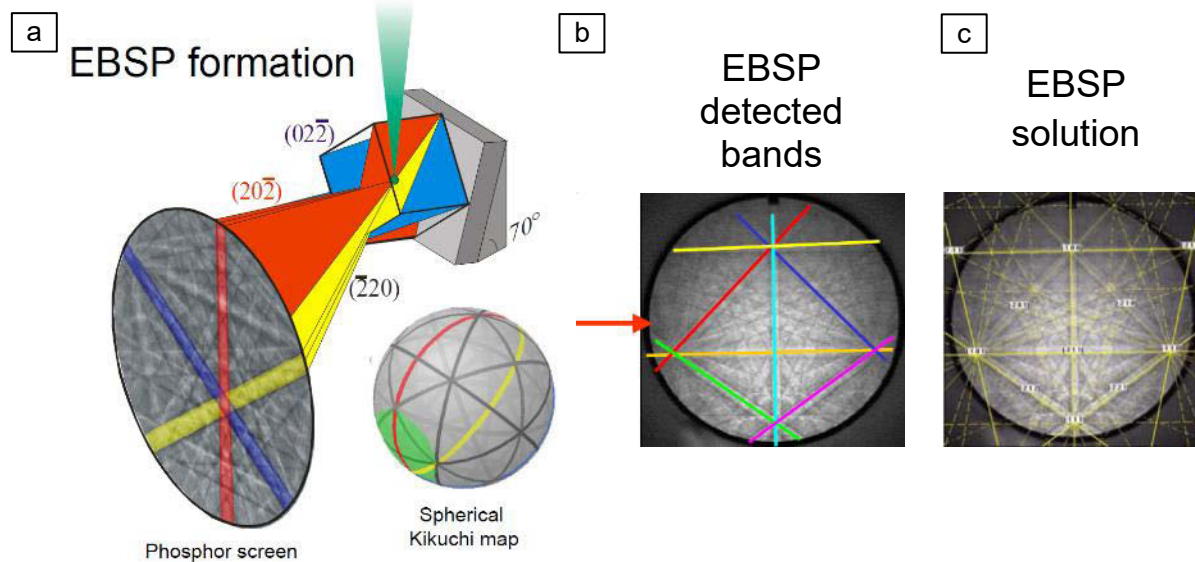


Figure 3.8 Formation of the electron backscattered diffraction pattern (EBSD) (a) determination of the Kikuchi bands position in the diffraction pattern (b, c) [96].

The analysis of EBSDs was carried out using the TSL OIM EDAX v.7 software (EDAX Inc., Draper, UT, USA). As a result of the analysis, the system delivers the phase and crystallographic orientation for each pixel of OIM map or gives a zero-solution, if it is unable to determine local orientation from the EBSD [97]. Zero-solutions can result from points where EBSD does not contain any band, and where EBSDs cannot be solved due to overlapping signals from several crystallites, or if a new phase not listed in the experimental set-up is encountered. The camera settings and the Hough parameters allow to collect data without significant loss in pattern quality with the angular resolution of $\sim 0.5^\circ$. EBSDs may not be produced if a strain in the sample surface is too high that no coherent diffraction can be produced or if a non crystalline material is encountered. Overlapping of EBSDs occurs at grain boundaries, when the electron beam diameter is large enough to produce EBSDs from two grains simultaneously.

The widths of the Kikuchi bands are determined by the Bragg's law and specimen-to-phosphor screen distance. The TSL OIM software operates with a dataset of Kikuchi bands, the width and relative position of which are determined by the crystallographic orientation for a given phase. The crystallographic data on pure copper and aluminum phases in the form of standard cif-files were used as input parameters for the TSL software. Matching algorithm compares the triplets of the detected bands with those calculated from the crystal structure for the phase of interest. The solutions found for all of the triplets are then used in a voting scheme to identify the most probable indexing of the pattern. The software ranks these orientations (or solutions) to the number of votes each solution obtains. The processing of the

results involves the voting procedure where four bands (for simplicity) are detected along with the indexing result. The confidence index is based on the voting scheme and is given as

$$CI = \frac{(V_1 - V_2)}{V_{IDEAL}}, \quad (3.1)$$

where V_1 and V_2 are the number of votes for the first and the second solutions and V_{IDEAL} is the total possible number of votes from the detected bands. The confidence index ranges from 0 to 1.

When EBSD is solved, its crystal phase, XY position, crystallographic orientation, goodness of fit (CI), and pattern quality are recorded. Nine Kikuchi-bands were used for EBSD indexing to minimize the misindexing error. To ensure a reliability of the EBSD data, all grains comprising of three or fewer pixels were automatically removed from the maps using the grain-dilation and neighbor orientation correlation options of the TSL software.

3.3.3.3. *Grain and subgrain size; grain boundary misorientations*

Grains in OIM are formed by an algorithm that groups sets of connected and similarly oriented points into "grains". For each point in the OIM scan, the neighbors of this point are checked whether they are within the Grain Tolerance Angle of the given point. If a neighboring point is found to be within the tolerance angle θ , then the neighbors of this point are checked whether they are within the tolerance angle of this point.

The cut-off value of $\theta = 2^\circ$ was set for the lower limit boundary misorientation for noise reduction. The $\theta = 15^\circ$ criterion was used to distinguish between low- and high- angle boundaries (LABs and HABs). The grain size (D) was computed using the equal diameter method, where the grain size is the average of the equivalent diameters of circles, with the area equal to the area of the grain. Crystallites with at least one of the boundaries with misorientation between 2° and 15° were identified as subgrains. It means that, if inside a grain one LAB was detected, this grain was not included into common statistic, but two subgrains were included. Specific grain area (S/S_i) distributions by the grain equivalent diameter were plotted for more than 500 grains in each state, where S is the map area and S_i is the area of the grains within the i -th interval.

For copper samples two misorientation threshold values of 3° and 15° were used to define the subgrains and grain boundaries. The respective mean grain sizes are labeled as D_3 and D_{15} .

3.3.3.4. *Scanning transmission electron microscopy*

To enhance the spatial resolution of the OIM analysis, the investigations by precession electron diffraction method using the automated crystal orientation mapping (ACOM) system integrated into a FEI Tecnai F20 transmission electron microscope (TEM) were carried out. Tecnai F20 is a field emission gun microscope operating at 200 kV and equipped with the ACOM-TEM system (ASTAR™, Nanomegas, Brussels, Belgium) [98].

Figure 3.9 illustrates the Vincent-Midgley scheme for precession electron diffraction [99]. Precession electron diffraction is a powerful method for improving the quality of electron diffraction data [100].

The deflection coils make the incident electron beam to precess in a conical shape above the sample. Such beam rocking is compensated below the sample to obtain a conventional-like diffraction pattern (DP).

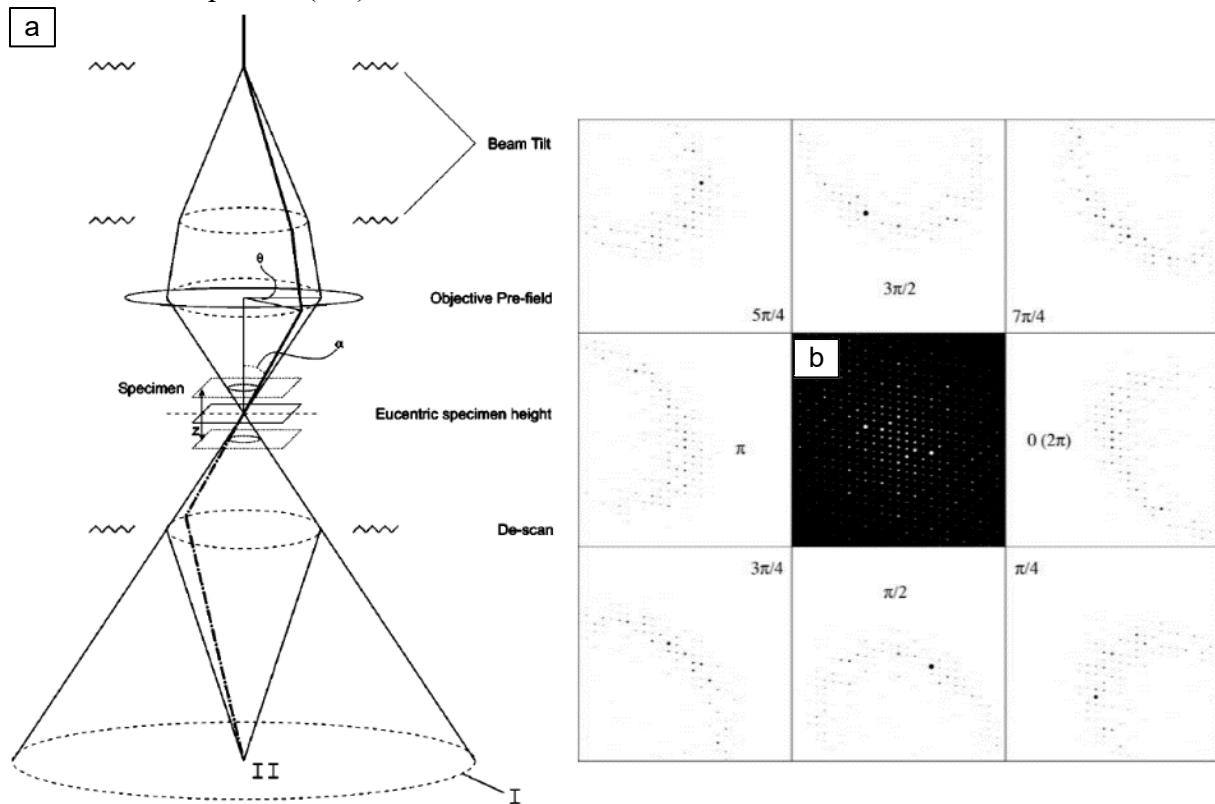


Figure 3.9 Precession geometry in the modern condenser-objective TEM (taken from [99]) applied for the ACOM-TEM technique (a) and the center precession pattern (b) (taken from [101]) are an integration of the simulated tilt series (contrast inverted) that surround the vertical axis, forming an effective cone of illumination.

The intensity is integrated at the detector (conjugated with the diffraction plane) by taking a time resolved measurement over an integral multiple of the revolution period. Figure 3.9 b from [101] demonstrates the example of the integration process using simulated [010] patterns of a $(\text{Ga, In})_2\text{SnO}_4$ crystal of 412\AA thickness. Amplitude patterns are used to portray the Laue circle more clearly. Figure 3.9 b shows eight discrete tilts along the precession circuit described by a tilt angle of the precessed beam θ , each tilted by $\theta = 24 \times 10^{-3}$ rad. The electron diffraction patterns were collected using the fast capture Stingray camera. The scanning and precession are controlled by the DigiSTARTM external device (NanoMEGAS). The fast frame acquisition camera allows to capture the spot diffraction patterns from every pixel, and these are stored by the Topspin NanoMEGAS software in the *.blo ('block') file.

The primary information that can be obtained from the spot diffraction patterns is the crystal orientation and the phase, which the crystal belongs to. Both the crystal orientation and the phases are obtained by systematic indexing procedure using the ASTAR software package. For the mapping, the μ -probe set-up for Tecnai, nominal beam diameter of $\sim 1\text{--}1.5$ nm and step size of 5 nm, semi-convergence angle of ~ 1 mrad, and a precession angle of 0.4° were used.

3.3.3.5. Estimation of dislocation density by EBSD-SEM data

The total dislocation density consists of two components: statistically stored dislocations (SSDs) and geometrically necessary dislocations (GNDs). According to the Ashby's model [25], GND density increases linearly with the imposed strain in a single-phase material, assuming that the geometric slip distance is a constant. If total dislocation density increases linearly with the strain for materials that undergo parabolic hardening, and if GND density increases linearly with strain as indicated by the Ashby's model, the evolution of SSDs and GNDs must remain proportional at deformation:

$$\rho_{SSD} + \rho_{GND} = \rho_{GND}(\rho + 1), \quad (3.2)$$

where ρ is a constant.

GND density determined from EBSD data involves the measurement of the lattice curvature in three dimensions [102-104]. With the knowledge of all possible dislocation types (combination of the slip plane and the Burgers vector), a measure of the required dislocation density that would result in the observed curvature can be obtained. Components of Nye's tensor of the dislocation density can be determined based on the lattice curvature from the EBSD data. This eventually will lead to an estimation of the GND density.

Standard nomenclature of slip systems for FCC crystals was used for copper samples. The algorithm considers both edge and screw dislocations. The maximum misorientation involved in the method was 2° . It means that misorientations included in the GND calculation were not those of the LABs. The maximum value for the GND density has to be taken also into account. The choice of the reference scale was automatically determined by the maximum density of the GND. In the case, when there is an area with a very high GND density, which is strongly different from the average value, and the step is too high to see the GND density distribution in the material, the step size is selected manually.

The calculations of GND density for a simple cylinder under torsion based on the strain gradient model proposed by Gao et al. [105] were performed. Assuming series of twist subgrain boundaries in the cylinder, where each contains two perpendicular arrays of screw dislocations, the misorientation angle ϑ is related to the GND density

$$\rho_{GND} = \frac{2\vartheta}{ub}, \quad (3.3)$$

where u is the unit length, and b is the magnitude of the Burgers vector. Kernel average misorientations (KAM), retrieved directly from EBSD data, were chosen as a measure for the local misorientations (Figure 3.10).

The KAM quantifies an average misorientation around the point of measurement with respect to a defined set of nearest (Figure 3.10 a) or nearest plus second-nearest (Figure 3.10 b) neighboring points. The values above the predefined threshold (here it is chosen to be 2°) are excluded from the calculation, because these points are assumed to belong to adjacent grains or subgrains (Figure 3.10 c).

For a physically meaningful GND density determination, the rank of the neighbor considered for the misorientation calculation is critical. Since the simple KAM values are not normalized by spacing, they increase with increasing neighbor rank.

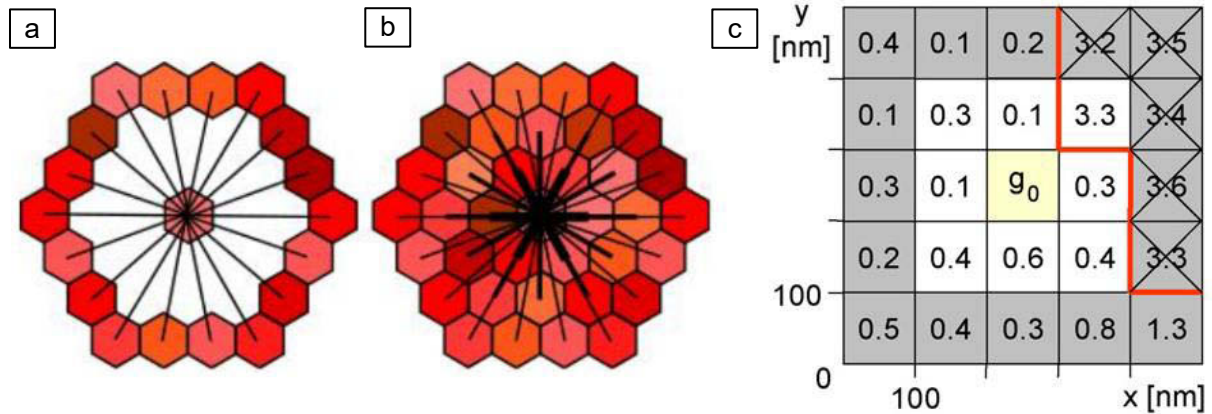


Figure 3.10 Principles of the GND density calculation based on the kernel average misorientation (a, b) for the case of a 2nd neighbor evaluation and a step size of 100 nm (c). Grain boundaries are marked in red. Misorientations that exceed the minimum threshold value of 2° are excluded from the calculation of the average misorientation of neighboring points to a given measurement point g_0 . Picture was taken from [106].

This is not the case for the calculated GND densities, since these values are distance-normalized. The calculation was done for each pixel in a map, taking into account the data for five nearest neighbors. The choice of five nearest neighbors was empirical such that the determined GND density will be comparable to that obtained in copper and aluminum after the deformation at the same conditions (temperature, strain rate, accumulated strain).

The task to estimate the GND density in UFG materials apparently faces the problem of the angular resolution of the measurement. M. Calcagnotto et al. in [106] proposed that three issues have to be considered when choosing the distance between two measurement points (step size during EBSD measurements):

- the distance has to be small enough to obtain detailed information the smallest elements of the structure. The resolution of EBSD is limited by the minimal scan step of the SEM. An enhanced spatial resolution is necessary for the detailed investigation of the dislocation density inside a grain and in the area close to GB. Although spatial resolution is directly related to the size of the interaction volume, it is not necessarily equal to it. Humphreys in [107, 108] reported an "effective" spatial resolution for various materials. The resolution is based on the size of the smallest resolvable objects that can be distinguished by EBSD, and therefore it is slightly less than the size of the interactive volume resolved by simply creating contrast on the detector screen. Even if there are two different lattice structures in the interaction volume, the EBSD software can identify the dominant structure, and thus identify the features. Since this measurements are highly situational, they indicate a possible resolution of only 20 nm.
- the distance has to be sufficiently large enough to average out the scatter of solutions due to the EBSD spatial resolution limits. In practice, the averaging of the scatter masks many details in the structure investigations.

3.3.3.6. Creation of dislocation density map from ACOM-TEM data

The ACOM maps were indexed using the ASTAR V2.0 software suite version with the orientation refinement algorithm [100, 109, 110]. The algorithm developed by Rauch et al.

[111] improves the angular resolution by interpolating the diffraction intensities between successive orientation templates. It results in the orientation determination accuracy of $\sim 0.3^\circ$, which is higher than that in the SEM-EBSD measurements under the settings used in this work.

For a quantitative analysis of the dislocation structure with a higher fidelity, a sample that shows no overlapping of the grains through the specimen thickness is required [95]. It is important also to consider projection artifacts and the resulting inconsistencies in the mapping of orientations and boundaries of crystallites (grain boundaries or subgrains) in the OIM using the original ACOM-TEM data. The projection effects arise mainly due to the presence of two or more grains through the thickness of the specimen. The images in Figure 3.11 demonstrate this issue.

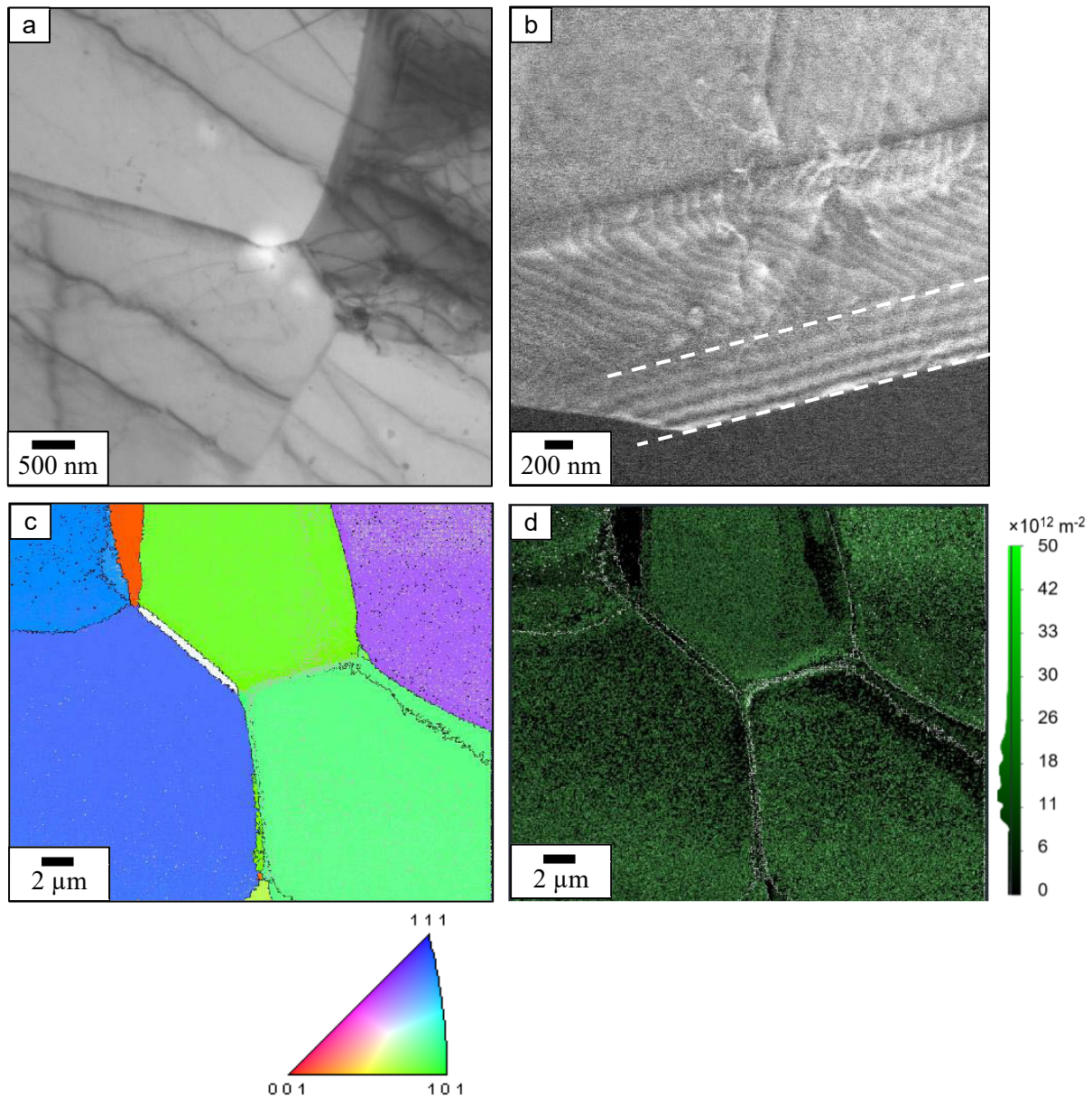


Figure 3.11 Bright field image (a), HAADF (b), oriented image map (c) and GND map (d) after reconstruction in ATEX. TEM of the coarse grained pure aluminum. Here and next the standard stereography triangle is used to indicate the crystal orientations in oriented image maps.

The dark contrast in the BF image of the Al CG sample in Figure 3.11 a is due to the two overlapping crystallites. This leads to an increase of the measured GND density in the resulting OIM. A tilted grain boundary can be clearly identified in the HAADF image of the same specimen (Figure 3.11 b) from the extinction contours.

This GB provides two HABs in OIM, since there are two intersection lines of the boundary on the projected image (marked by white dashed lines in high angle annular dark field (HAADF) Figure 3.11 b). The overlapping crystals can produce more fragments of HABs in OIM and GND maps (HABs are marked in Figure 3.11 c by black lines) and result in a higher GND density in the overlapping area (Figure 3.11 d).

The local orientation spread approach provides relative strain values for each point in a given region. It is a fast and convenient method to determine relative dislocation density values from ACOM data. These calculations were carried out using the ATEX software [112]. The values produced is a scalar estimation of a local strain that can be compared directly from sample to sample for a given material and consistent acquisition parameters.

The local strain distribution was converted into the GND distribution using the OIM TSL software in the same way as described for EBSD-SEM maps in subsection 3.3.3.5. ACOM TEM capabilities provide higher resolution than EBSD-SEM, allowing the range of the threshold angle to be extended from (1.0; 2.0) to (0.2; 2.0).

3.3.3.7. *Estimation of integral dislocation density from X-ray diffraction peak broadening*

The SSD density cannot be measured using the SEM-EBSD or ACOM-TEM techniques, since they give the lower bound estimate of the GND density. An estimation of the total dislocation density can be carried out from the broadening of X-ray diffraction (XRD) peaks. The method of peak broadening is based on analyzing the width of the peaks in the X-ray diffraction pattern obtained in Bragg-Brentano geometry.

XRD data were collected using the Philips X'Pert powder diffractometer (Figure 3.12 a), operating in the Bragg-Brentano geometry with Cu-K α wavelength. The background of the diffraction pattern was calculated by the X'pert HighScore software. The irradiated area had the dimensions of 1×5 mm². This made it possible to obtain XRD data from three different locations at the sample along the shear direction (SD) in the longitudinal rod cross section.

XRD patterns were fitted by the pseudo-Voigt function, and parameters of the XRD peak profiles, i.e., peak intensity and full width at half maximum were obtained. The mean diameter of the crystallites (size of coherently scattering domains, D_{hkl} , used for the dislocation density calculation) and micro-strain were estimated from the diffraction peak broadening using the modified Williamson-Hall method [113, 114]. It is known that in the case of a random distribution of dislocations, the total dislocation density ρ can be calculated as [114], [115]:

$$\rho = \frac{2\sqrt{3}\langle\varepsilon_{hkl}^2\rangle^{1/2}}{D_{hkl}b}, \quad (3.4)$$

where D_{hkl} is crystallite size, $\langle\varepsilon_{hkl}^2\rangle^{1/2}$ is the mean squared micro-strain value, and b is the absolute value of the Burgers vector.

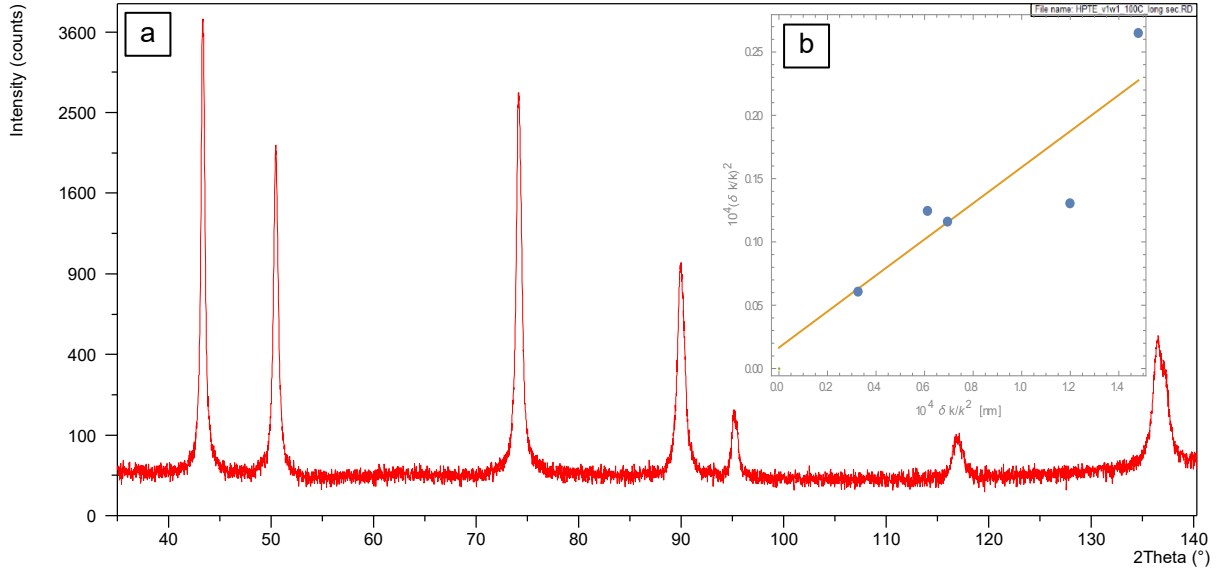


Figure 3.12 Typical X-ray diffraction pattern from the edge area of the Cu rod after HPTE $v1w1$ regime ($\lambda_{Cu}=154.183$ pm) (a). Williamson-Hall plot of the XRD pattern shown in (b).

For estimation using the Williamson-Hall method [113, 116], the measured XRD peaks were fitted using the Philips Profil Fit 1.0 software and peak position and intensity, full width at half maximum (FWHM) and integral breadth were determined. All reflections with Miller indices up to (420) were used for estimating the grain size and microstrains.

A LaB₆ standard powder was used to determine the instrumental broadening for correction. The reflection width q can be described as

$$\delta q = \frac{2\pi K}{\lambda} \cos \theta \delta(2\theta) \quad (3.5)$$

The crystal lattice strain-induced broadening of XRD peaks occurs due to local changes in the lattice parameter A relative to its average value. Its effect on the peak broadening is usually expressed as

$$\delta k_{strain} = 2\varepsilon k, \quad (3.6)$$

where ε is a microstrain.

The deconvolution of the size- and strain-contributions to the peak broadening is typically based on the assumptions on the functional form of the individual contributions. It is assumed that the size-broadening is Lorentzian, and the strain broadening is Gaussian [114]. By analysis of the convolution of the two functions, one obtains the following expression for the net broadening, δk , due to the combined strain- and size-effects:

$$\frac{(\delta k)^2}{k^2} = 1 - \left(\frac{\delta k_{strain}}{k} \right)^2. \quad (3.7)$$

In terms of Equation (3.6) and (3.7), one then obtains the modified Williamson-Hall relation:

$$\frac{(\delta k)^2}{k^2} = \frac{2\pi K}{3D} \frac{(\delta k)^2}{k^2} + 4\varepsilon \quad (3.8)$$

Equation (3.8) has a line form $y=bx+a$, where $x=\frac{\delta k^2}{k^2}$ and $y=\frac{\delta k^2}{k^2}$. Thus, in the plot (Figure 3.12 b) of $\frac{\delta k^2}{k^2}$ vs $\frac{\delta k^2}{k^2}$, the slope measures the inverse crystalline size, and the ordinate intercept measures the magnitude of a microstrain.

3.4. Mechanical properties testing

A Buehler Micromet-5104 tester was used for the microhardness measurements. A load of 0.2 kg with a dwell time of 15 s was applied to all samples during the hardness measurements. A Vickers indenter was used. Five indentations spaced 1 mm apart were made along two mutually perpendicular diameters of the specimens. The average value was computed from 10 indentations.

Tensile tests were carried out at ambient temperature at an initial strain rate of $1 \times 10^{-3} \text{ s}^{-1}$ using the Zwick Z100 screw-driven testing machine on cylinder-shaped samples with threaded heads (Figure 3.13). The tensile samples, both gradient and hybrid ones, were machined in accordance with the ASTM E 8/E 8M-08 requirements.

According to the results of the FEM calculations, tensile specimens were machined from the middle part of the HPTE-processed billets avoiding less-processed zones at the billet edges (Figure 3.13 b).

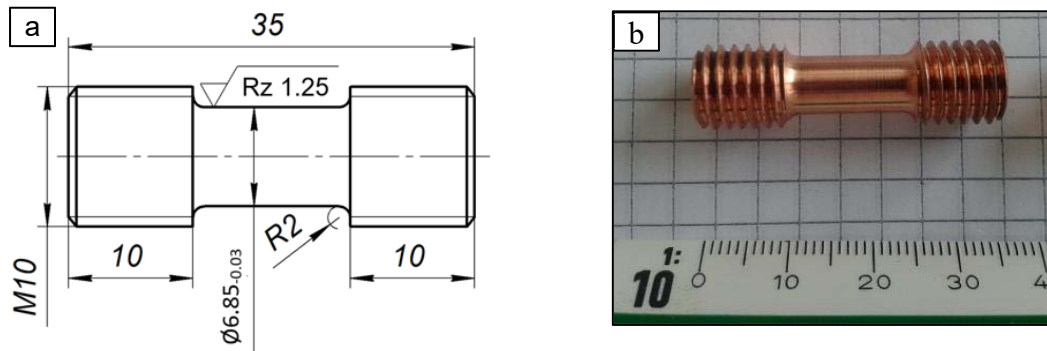


Figure 3.13 Schematic drawing of the tensile test sample (a) and photo of the sample after machining (b). Dimensions are given in millimeters.

After the rupture, the resulting engineering force-elongation curves were recalculated to the engineering stress-engineering strain curves based on the assumption of the constant volume of the gauge:

$$\sigma = \frac{P}{S_0} \quad (3.9)$$

and

$$\varepsilon = \frac{\Delta l}{l_0} \quad (3.10)$$

where P is the applied load, S_0 is the initial cross-sectional area of the specimen, l_0 is the initial length, and Δl is the displacement.

The threaded mounting of the specimens in the grips ensured sufficient fixation of the tensile specimen during the whole test. The ends of the Fe wires in the hybrid samples were fixed at the ends of the gripped portions of the hybrid specimens. This fact was confirmed by the localization of the rupture in the gauge portion in all hybrid specimen configurations tested.

3.5. Finite element modeling settings and validation

To calculate the strain distribution in the HPTE process with *hexagonal dies* (Figure 2.6 b), 3D finite element analyses were performed using the commercially available QForm VX 8.2.4 software [117].

Validation of the FEM results was performed by the marker line in Figure 3.14 a, that was placed in the same position as the marking wire in experimentally processed billet (Figure 3.3 c, d). Postprocessing analysis on the QForm included using the marker line is placed parallel to the ED (marked by the white line in Figure 3.14 a) at 5 mm from the center of the rod. The position of the marking line during the HPTE process and after that is shown by the red line in Figure 3.14 b, c.

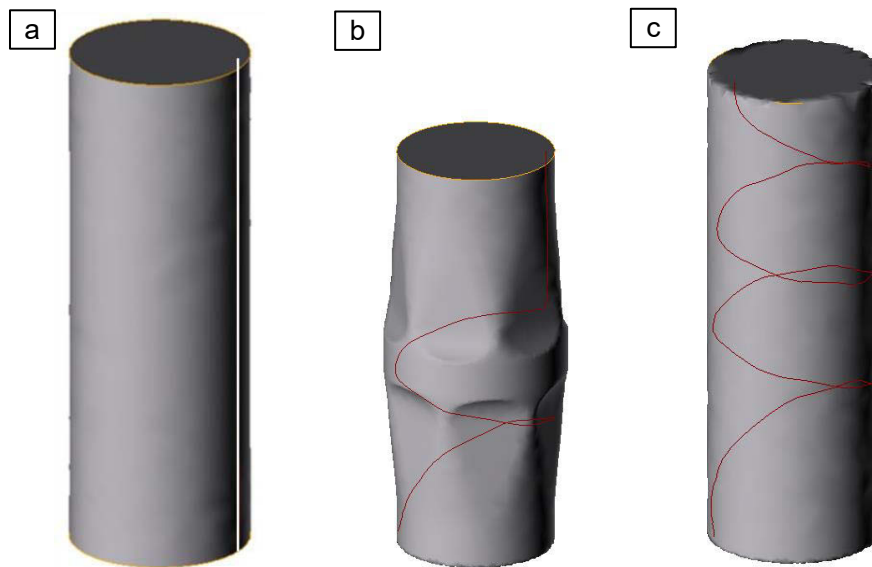


Figure 3.14 3D images of the billet and marker lines, used for the FEM, in the initial rod (a), at the intermediate stage of the HPTE process (b) and after processing (c).

The configuration of the resulting helical shape of the marker line (Figure 3.14 b, c) is compared with the configuration of marker wires, indicated by X-ray tomography.

To simplify the calculations, FEM was performed for the middle sample (marked with orange color in Figure 2.6 c). For this purpose, the top and the bottom samples in the real HPTE process were replaced by the punch and plug tools in the simulation (marked by the blue and red rectangles in Figure 2.6 c).

A 3D deformation problem was set for the stress calculation. Table 3.3 lists the material parameters for all simulations performed in this study. Levanov's law was used. According to the Levanov friction model [118], shear stresses on the contacting surface of a billet depend

on the friction factor m , flow stress σ_f of the billet material, normal contact pressure σ_n , and Levanov coefficient n :

$$\tau = m \frac{\sigma_f}{\sqrt{3}} \left(1 - e^{-n \frac{\sigma_n}{\sigma_f}} \right) \quad (3.11)$$

The nature of the curve described by the Levanov law is highly dependent on the value of n . In the QForm 8.2.4 software, the Levanov coefficient n is assumed to be equal to 1.25.

All FEM results were obtained in a steady state. The meshing procedure was applied in the Gsmh software [119] using the option for a free 3D shape that was imported from IGES (International Graphical Exchange Standard for CAD-systems) format.

Table 3.3 Data for FEM calculation of HPTE deformation of copper.

parameter	value
Density, kg/m ³	8850
Thermal conductivity, W/(m*K)	385
Specific heat, J/(kg K)	390
Levanov coefficient	1.25
Young modulus, GPa	125
Poisson coefficient	0.35

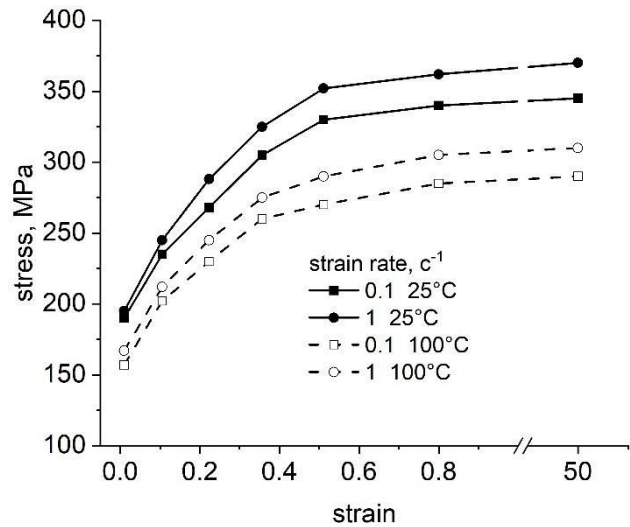


Figure 3.15 Engineering stress-strain curves for FEM calculation of HPTE deformation of copper.

Axisymmetric 4-node continuum elements were chosen for discretization. Mesh sensitivity was studied by reaching a convergent load/displacement curve extracted from the pillar region. Gerasimov et al. introduced the algorithm of the volume geometrical tetrahedral meshing network construction used in Qform software in [120]. In this approach, the size of the meshing network elements in the segments of the analyzed volume with complicated shape is finer than that in the segments with simple shape. In other words, Gerasimov et al. in [117] proposed to use in Qform two tetrahedral finite element meshes having different mesh density distributions in different parts of the analyzed volume simultaneously. The same dual mesh method was used in the present work.

Due to the large strains reached during HPTE, the geometry of meshing elements is reconstructed every few calculation steps. The maximum number of calculation steps without remeshing was 20, the maximum external angle of the meshing element set to 151°. When the value of the external angle of the triangle exceeded 151°, the remeshing procedure was initialized.

Strain hardening of each mesh element was calculated using the strain hardening curves of copper available in the QForm software database (Figure 3.15). In the examined HPTE regimes, the strain rates were $\sim 1.0 \text{ s}^{-1}$.

4. Investigation of material flow at HPTE: FEM calculations and experimental validation

4.1. Strain analysis of the processed billets

The plastic flow during the HPTE process was analyzed in two stages of the process: the intermediate stage and after processing. The intermediate processing was realized by stopping of the HPTE at the half-processed stage, followed by disassembly of the HPTE dies.

4.1.1. Intermediate processing

Figure 4.1 illustrates how aluminum wire markers, initially embedded parallel to the ED, changed their shape during HPTE deformation. In Figures 4.1 a, b it can be seen that the wires acquire a helical shape after the $v6w1$ and $v1w1$ HPTE regimes.

The longitudinal section of the billet after the $v6w1$ HPTE regime demonstrated that the initial round shape of the wire cross section transformed into a thin ribbon, with the maximum of the narrowing occurring at the bottom part of the billet. Note that the wires appeared to be severely deformed (obtained a shape of a narrow ribbon) at a distance of 4-6 mm from the contact plane of the upper and lower HPTE dies (shown with the white dashed line in Figure 4.1 a, b), which approximately delineates the size of the shear deformation zone in HPTE. The drop-like shape of the cross section of the ribbon had a maximum narrowing on the side closest to the periphery of the sample (Figure 4.1 a). After the $v1w1$ regime, neighboring Al layers became very close to each other (Figure 4.1 b, c).

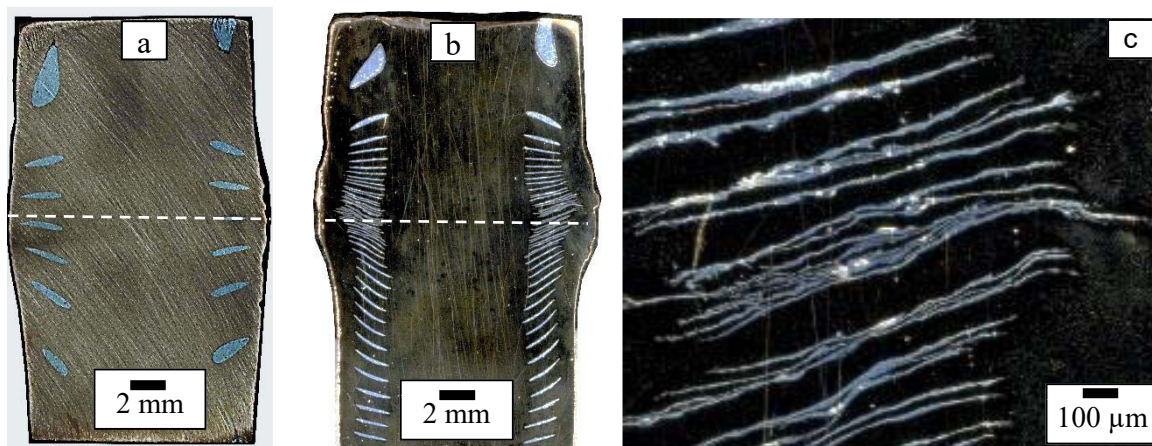


Figure 4.1 The images of the longitudinal (a, b, c) cross sections of the copper samples with six aluminum markers obtained using optical microscopy. The samples were processed by the $v6w1$ (a) and $v1w1$ (b, c) HPTE regimes at 25°C. The position of the plane between the top and bottom HPTE dies, is indicated by the dashed lines in (a), (b).

4.1.2. Full-height processing

The metal flow during HPTE was analyzed by the marker-insert technique. Commercially pure aluminum wires were used as markers tracing a real material flow in commercially pure copper samples during the HPTE process. Figure 4.2 displays 2D images

of the HPTE-processed sample after the $v6w1$ regime at 100°C and 25°C obtained by optical microscopy and X-ray tomography.

In the latter case, aluminum wires were identified as regions of interest (ROIs) and highlighted in Figure 4.2 by different colors. Each wire was resolved as a separate ROI, thus allowing to extract it from the conglomerate of six wires and consider separately (Figure 4.2 a). As was mentioned above for intermediate processing, the marker wires were transformed into ribbons. The ribbons were inclined to the billet axis (Figure 4.2 a). This tilting appears due to a strong friction at the billet/die wall surface. Each of the six wires was twisted for the equal number of loops $N_H=1.4$ (Figure 4.2 c). The marker wire helices were tighter in the bottom part of the billet compared to the middle and in the upper parts (a), indicating stronger twisting, and, therefore, better friction in the lower part of the die.

The transversal cross sections of the HPTE-processed Cu-Al hybrid sample demonstrate that the Al markers changed their shape from near-circular (Figure 3.3 c) to drop-like one (Figure 4.2 c, d). The degree of elongation of these “drops” changes along the height of the sample: from slightly elongated “drops” in the top part of the bar (Figure 4.2 b) to much more strongly elongated ones in the middle (Figure 4.2 c) and bottom parts (Figure 4.2 d).

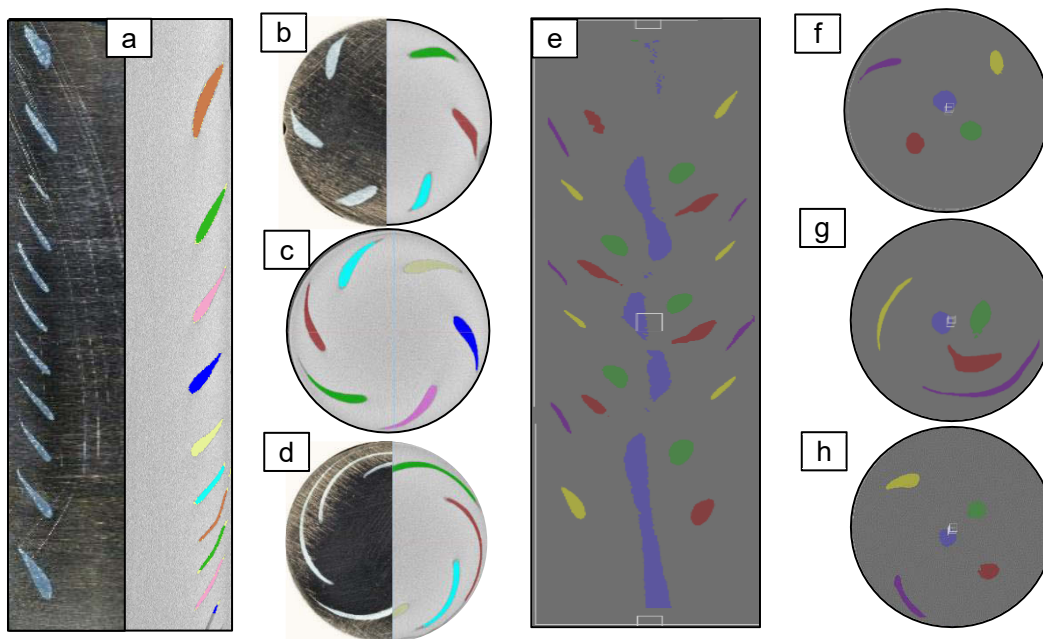


Figure 4.2 The 2D images of the aluminum wires in copper billets after the $v6w1$ regime at 100°C (a-d) and at 25°C (e-h) were captured in both longitudinal (a, e) and transversal (b-d, f-h) sections. The initial configurations with six wires (a-d) and five wires (e-h). Optical microscopy was combined with the results of X-ray tomography in (a, b, d) to obtain detailed information.

The marker wires in the sample deformed at 25°C (Figure 4.2 e) were twisted much stronger than those in the sample deformed at 100°C. Irrespective of the distance between the center of the wire and the center of the sample, all wires had an equal number of loops $N_H = 3$, but the shapes of the wire cross sections were different (Figure 4.2 f-h). The wire placed close to the center of the sample retained its initial nearly-circular shape, while other wires changed their shape to the ribbons. The same number of loops of the wires, placed at different distances from the sample center and processed by the $v6w1$ regime at 25°C (Figure 4.2 e),

demonstrates that all points in any transversal plane of the billet were rotated with the same angular velocity w .

Table 4.1 The experimentally obtained number of loops of the marker wires after the HPTE process and the values of friction coefficients employed for the FEM calculation.

$T, ^\circ\text{C}$	Process ID	N_H^*	w_e, rpm
100°C	$v10w0$	0	0
	$v6w1$	1.4	0.24
25°C	$v10w0$	0	0
	$v6w1$	3.0	0.51

* N_H – number of loops of the embedded wire in the full-height copper sample, experimentally measured after HPTE processing

The reduced number of marker wire loops in comparison with the number of HPTE tool rotations indicates significant slippage between the die walls and the billet despite the presence of hexagon holding elements in the die design (Figure 2.8 b). Summarizing the observations of the marker wires' deformation resulting from different HPTE regimes, the following conclusions can be drawn:

- the shear deformation zone in HPTE has a thickness of 4-6 mm from the contact plane of the upper and lower HPTE dies;
- apart from shear (twisting) and expansion-extrusion deformation, there is a significant strain increase in the periphery region of the billet;
- there is a noticeable discrepancy between the number of marker wire loops and the number of HPTE tool rotations, indicating significant slippage between the die walls and the billet. This discrepancy is more pronounced in billets deformed at 100 °C than at 25°C.

4.2. FEM modelling of the HPTE process

In order to explain the experimental observations above, and to calculate the strain distribution in billets at HPTE precisely, FEM simulations have been performed.

4.2.1. Definition of contact friction coefficients

One of the most important parameter for the FEM modelling calculations is a friction coefficient between the billet and contact surfaces of the HPTE tool (see Figure 2.8 c): bottom surface of the punch, top HPTE die, bottom HPTE die, and top surface of the plug providing back pressure. As discussed in section 2.3.1, there was slippage between the die walls and the billet. In order to select the appropriate values of the friction coefficient on all contact surfaces from the QForm Standard Lubricant Database, the experimentally obtained helical shape of the Al wires after HPTE (Figure 4.2) was compared with the shape of the marker lines in the simulated samples (Figure 3.14). This comparison allowed the determination of friction coefficients that ensured the alignment of HPTE tool rotations with the number of

marker line loops for FEM calculations. The validated values of the friction coefficients are summarized in Table 4.2.

The following friction coefficients were initially used for the processing without rotation of the bottom die: 0.2 (Zn Stearate grease) and 0.6 (dry metal-to-metal friction). However, it was observed that FEM simulations using these friction coefficients predicted a higher number of wire marker loops in comparison to the experimentally observed number of loops. Consequently, even lower values of friction coefficients had to be employed.

Table 4.2. The experimentally obtained values of friction coefficients employed for the FEM calculations.

T, °C	Process ID	N _H	w _e , rpm	Friction coefficient			
				plug	punch	top die	bottom die
100°C	<i>v10w0</i>	0	0	0.1	0.1	0.6	0.6
	<i>v6w1</i>	1.4	0.24	0.1	0.1	0.15	0.6
25°C	<i>v10w0</i>	0	0	0.1	0.1	0.6	0.6
	<i>v6w1</i>	3.0	0.51	0.1	0.1	0.2	0.6

Next, lower values of the friction coefficients between the billet and the top HPTE matrix were assigned for the FEM calculation to achieve a less twisting of the marker line while accurately replicating the experimentally obtained number of loops of the marker wire (Figure 3.14). It should be noted that different friction coefficients were chosen for the FEM calculations of the HPTE process at 25°C and 100°C, considering that the resulting shapes of the marker wire helix were different at different temperature of HPTE processing.

Here, we examined the shape of each wire in the sample with six wires after the *v6w1* regime performed at 100°C and the wire located at the same distance from the center in the sample with five wires after the same HPTE regime performed at 25°C (depicted as the dark blue wire in Figure 4.2 e). The significant difference in N_H values between the samples deformed with the same HPTE regime at 25 and at 100°C led to variations in the chosen friction coefficient values, particularly for the top die and the punch (refer to Table 4.2).

4.2.2. Strain analysis of the processed billets

At the beginning of this section, it was demonstrated that the previously discussed friction coefficients allowed an accurate reproduction of the real deformation of the marker wires, as described in Section 4.1.2, in the virtual experiment. Figure 4.3 illustrates the changes in the shape of the initially straight marker line after the full HPTE processing. The *v10w0* HPTE regime had no impact on the shape of the marker line, which remained straight after processing (Figure 4.3 a). However, HPTE processing with rotation of the bottom die resulted in the formation of a helical shape of the marker line (Figure 4.3 b, c), with the number of loops matching the number of marker wire loops N_H obtained in the corresponding experiments (refer to the capture below Figure 4.3).

Comparison of the shapes of the model and experimental markers revealed small differences. Specifically, the FEM-simulated configurations of the marker lines after the HPTE process using the *v6w1* regime at both temperatures showed uniform twisting of the marker wires/lines and the formation of regular helixes along the entire height of the billet

(Figure 4.3 b, c). In contrast, the loops of the marker wire helices in the real experiment were closer to each other in the bottom part of the billet compared to their spatial distribution in the middle and upper parts of the billet (Figure 4.3 a).

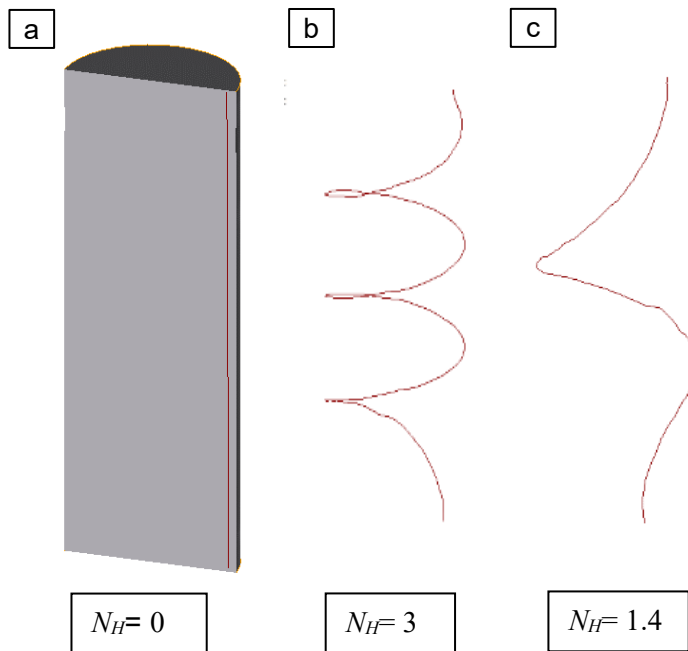


Figure 4.3 FEM-simulated configurations of the marker lines after the HPTE process executed using the $v10w0$ (a) and $v6w1$ (b, c) regimes at deformation temperatures of 25°C (a, b) and 100°C (c).

In both cases, the highest density of loops was observed in the middle part of the billet, with fewer loops at the end parts of the processed billet. This observation is consistent with the lower strain values calculated by FEM simulations, indicating a lower level of deformation in these areas. A similar non uniform distribution of strain along the length of HPTE-processed billets was also reported in the work of Kulagin et. al [76].

The strain distributions in billets processed at various HPTE regimes calculated by FEM can be discussed in terms of the holding elements shape effect on the resulting strain. In the case of the $v10w0$ HPTE regime without a rotation of the bottom die, the strain distribution in a transversal cross section of a billet exhibits a similarity to a hexagonal shape (Figure 4.4 a). However, after the $v6w1$ regime (Figure 4.4 b, d) the strain distribution appears to be smoother and takes on a ring-like pattern.

The strain distribution maps in the transversal and longitudinal billet cross sections after the $v10w0$ HPTE regime at room temperature reveal lower strain values in the center and middle-radius area, and higher strain values in the edge area compared to the same HPTE regime at 100°C (Figure 4.4 a, c). On the other hand, significantly higher resulting strain is observed in the billet processed via the $v6w1$ regime (Figure 4.4 b, d). It is important to note that the strain values in the sample processed at room temperature are much higher than those achieved at 100°C (compare left and right images in Figure 4.4 b, d). This difference is attributed to the different hardening behavior of the Cu matrix at room temperature and 100°C (Figure 3.15).

When considering the strain distribution in the longitudinal section of a billet after different HPTE regimes, it is evident that there is a gradient of strain from the center to the periphery along the RD throughout the height of the billets (Figure 4.4 c, d). In the billet processed using the $v10w0$ HPTE regime, this gradient strain distribution appears relatively uniform along the height of the billet (Figure 4.4 d).

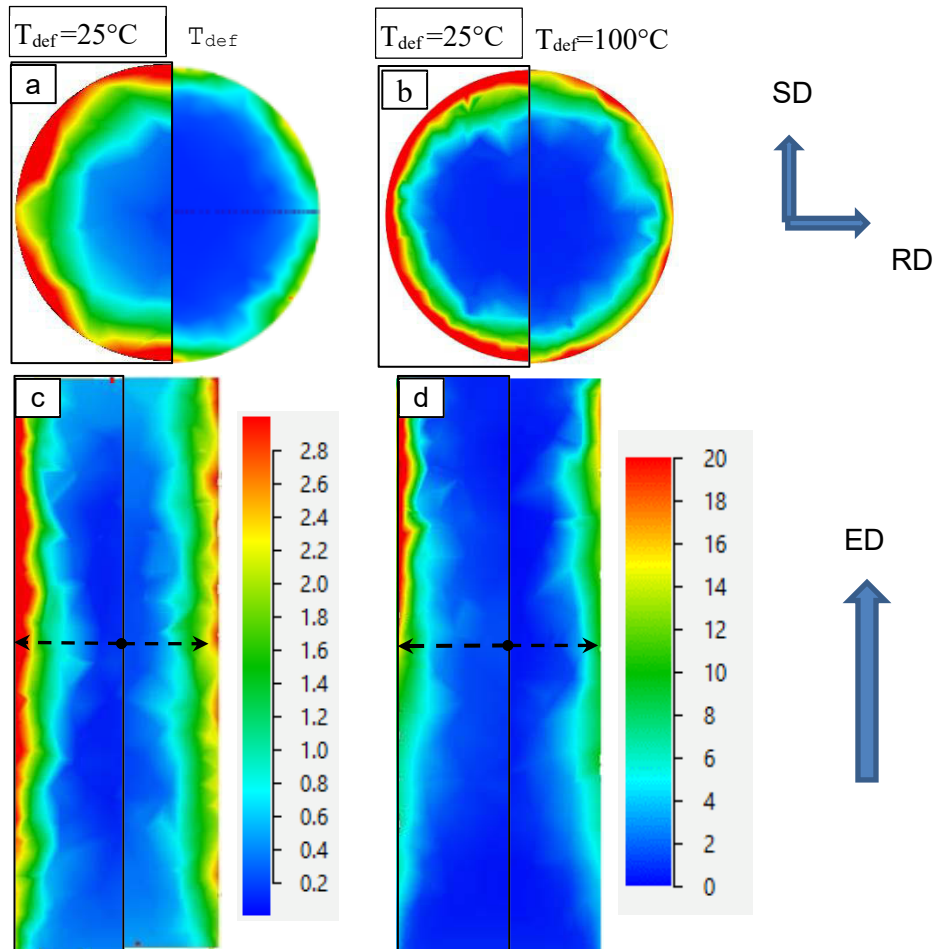


Figure 4.4 The strain distribution after HPTE of copper at 100°C (right part of a-d) and at 25°C (left part of a-d). The HPTE regimes $v10w0$ (a, c) and $v6w1$ (b, d) were used for the calculations. Strain distributions are represented in transversal (a, b) and longitudinal (c, d) billet sections. The transversal section is taken at the half of the height of the billet.

On the other hand, the $v6w1$ HPTE regime with a rotation of the bottom die results in the strongest strain distribution gradient in the top part of the billet (Figure 4.4 d). Although the variation in deformation temperature does not change the character of the strain distribution, it does lead to higher strains at the lower deformation temperature (25°C) for all HPTE regimes (Figure 4.4 c, d).

In order to illustrate the strain distribution in the HPTE-processed billets more clearly, the variation of the accumulated strain along the dashed lines, as shown in Figure 4.4 c, d, was plotted in Figure 4.5 a, b.

For comparison, Figure 4.5 showed the strain distributions along the radius of the billet, which were calculated according to the analytic Equation (2.12) using the experimental values of effective rotation velocity w_e (Table 4.2). It was also noted that strain distributions

calculated by Equation (2.12) were close to the FEM-calculated ones only for the $v10w0$ and $v6w1$ regimes at 100°C , specifically for the central and middle parts of the billet (Figure 4.5 a).

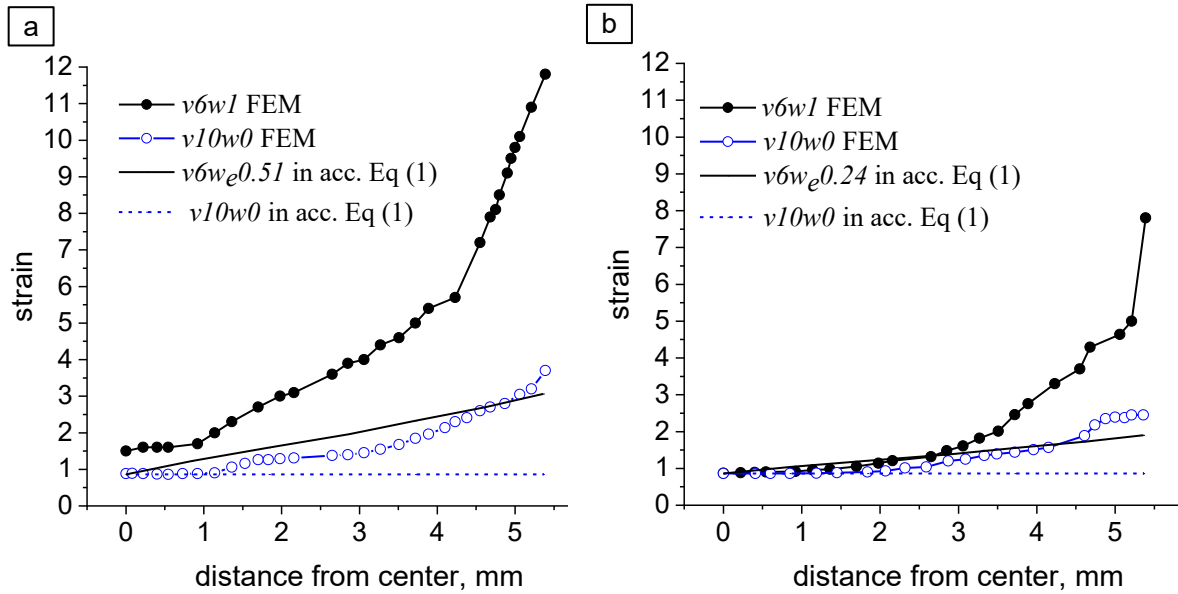


Figure 4.5 The accumulated strain distribution in the transversal cross section at the half of the billet height was calculated using the FEM and Equation (2.12) for the $v10w0$ and $v6w1$ HPTE regimes at 25°C (a) and 100°C (b). The strain estimate by Equation (2.12) utilized experimentally obtained values of rotation velocity w_e from Table 4.2.

For all other regimes or billet locations, a strong deviation between the strain distributions calculated by Equation (2.12) and by FEM was observed. Specifically, in billets subjected to the $v10w0$ and $v6w1$ HPTE regimes, the FEM calculated strain grew exponentially in the close vicinity to the edge due to surface friction (Figure 4.5 a, b). Such behavior was not predicted by the analytic equation. Additionally, after the $v6w1$ regime, the strain gradient from the center to the edge was stronger compared to the HPTE regime without rotation (increasing from approx. 1.4 to 8.0 and from approx. 0.8 to 3.0, respectively) (Figure 4.4 a, b). Furthermore, for the $v6w1$ HPTE regime at 25°C , FEM calculations resulted in significantly higher strain values compared to the strains calculated from Equation (2.12).

Different friction coefficients were chosen for the FEM calculations of the HPTE process at 25°C and 100°C , as the resulting shapes of the marker wire helix varied at different temperatures of HPTE processing. In this study, the shape of a specific wire in the sample with six wires after the $v6w1$ regime performed at 100°C , was compared with the wire located at the same distance from the center in the sample with five wires after the same HPTE regime performed at 25°C (dark blue wire in Figure 4.2 e). The discrepancy in the N_H values between the samples deformed with the same HPTE regime at 25°C and at 100°C led to differences in the selected friction coefficient values, primarily for the top die and the punch (Table 4.2).

FEM simulations revealed some minor variations in the shape of the marker lines compared to that of the wire markers. However, the number of loops and the distribution of their density along the height of the simulated marker lines (Figure 4.3) matched the

configurations of the marker wires obtained experimentally (Table 4.1). This compliance correspondents validates the accuracy of the FEM calculation and confirms the reliability of the simulation parameters. Specifically, the FEM-simulated configurations of the marker lines after the HPTE process using the $\nu 6w1$ regime at both temperatures indicate a uniform twisting of the marker wires/lines.

5. Characterisation of gradient and hybrid samples after HPTE

5.1. Microstructure of copper after HPTE

The formation of a gradient structure in samples processed by HPTE was analysed using pure copper.

5.1.1. Microstructure characterisation

A typical OIM map of the initial Cu structure is shown in Figure 5.1 a. The OIM map, obtained from the EBSD data, demonstrates random grain orientations.

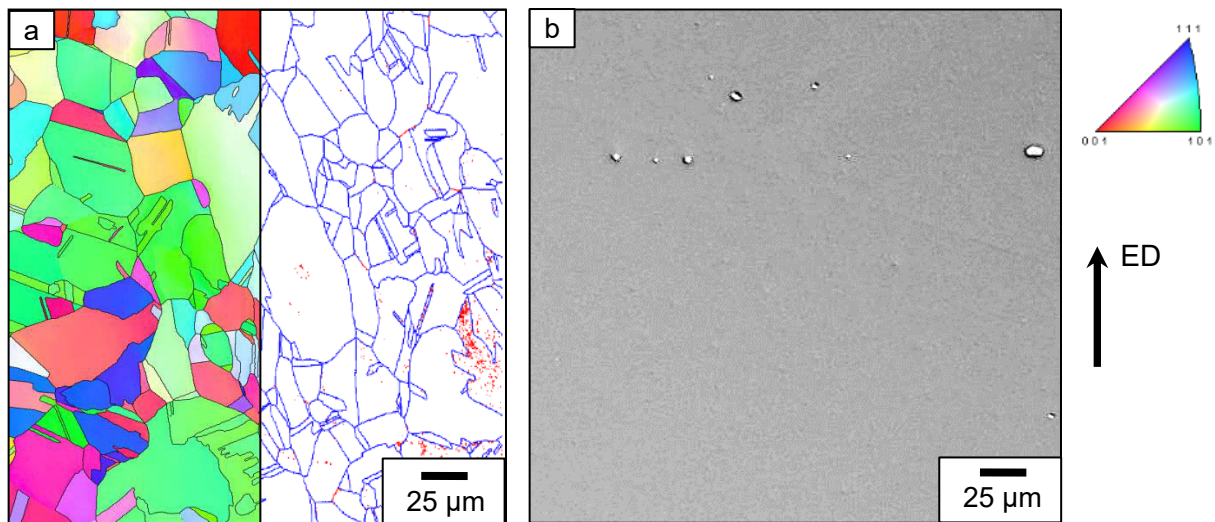


Figure 5.1 The typical OIM map (a, left), grain boundaries map (a, right) and BSE image (b) of the annealed Cu rod (longitude section). In the OIM map, the coloring corresponds to the projection of the ED in the inverse pole figure. In the grain boundaries map high angle misorientations ($\theta > 15^\circ$) are indicated with blue lines, and low angle misorientations ($2^\circ < \theta < 15^\circ$) are indicated with red lines

The initial structure of Cu sample is characterized by near-equiaxed grains, with an aspect ratio of approx. 0.8). In addition Figure 5.1 a shows the presence of numerous annealing twins and an average grain size of around 30 μm . Additionally, the backscattered electron (BSE) image in Figure 5.1 b reveals the presence of second-phase particles in the microstructure.

The BSE image indicates impurities as second-phase particles. These particles are identified as Cu-rich intermetallic phases [91, 121] and are characterized by the nearly spherical shape with an average diameter of approx. $2.5 \pm 0.5 \mu\text{m}$. According to the technical specifications of copper [91], these particles originate from metallurgical sources and may also include oxides, hydrides, and some other impurities introduced during flux-income processes.

5.1.1.1. Microstructure in the central area of the billet

The OIM analysis was performed on the central, mid-radius, and edge areas of the samples that were previously processed by HPTE using the $v10w0$, $v10w1$ and $v1w1$ regimes.

The corresponding microstructures for state are shown in Figure 5.2 and Figure 5.3. In the analysis, different colors are assigned to grains displaying different crystallographic orientations, according to the standard stereographic triangle shown in Figure 5.2. The microstructure parameters, including the grain size at respective boundary misorientation threshold (D_3 and D_{15}), the average misorientation angle (θ_{av}), the volume fraction of HABs ($V_{>15^\circ}$), the volume fraction of twin boundaries (V_{twin}), the size of second-phase particles (d_p), and their volume fraction (f), are summarized in Table 5.1.

In the transvers section of the central area, the microstructure observed after the $v10w0$ and $v10w1$ HPTE regimes is characterized by equiaxed coarse grains (Figure 5.2 a, d, top) with a mean grain size similar to that of the initial undeformed copper (Figure 5.1 a).

Following the HPTE regimes of $v10w0$ and $v10w1$, the grains in the central area of the specimen appear slightly elongated in the extrusion direction, as seen in the longitudinal section (with an aspect ratio 1.4). The aspect ratio of the grains is 1.0 and 0.9 in transversal section after the $v10w0$ and $v10w1$ HPTE regimes, respectively.

Table 5.1 The structural parameters of Cu samples after the HPTE treatment at 100°C were determined based on SEM–EBSD analysis in the longitudinal and transverse cross sections.

Process ID	$D_{15}, \mu\text{m}$	$D_3, \mu\text{m}$	$V_{>15^\circ}, \%$	θ_{av}, deg	$V_{twin}\%$	$GND \times 10^{-12} \text{m}^{-2}$	
initial	30.0 ± 0.2	-	90.0 ± 0.05	47 ± 0.5	17.0 ± 0.05	11 ± 5	
$v10w0$	center	$\frac{23.5 \pm 0.5}{21.5 \pm 0.5}$	$\frac{22.0 \pm 0.5}{9.5 \pm 0.5}$	21.9 ± 0.05	13.4 ± 0.5	19.3 ± 0.05	40 ± 5
	mid-rad	$\frac{21.5 \pm 0.5}{18.5 \pm 0.2}$	$\frac{17.5 \pm 0.2}{6.5 \pm 0.2}$	15.3 ± 0.05	10.9 ± 0.5	4.0 ± 0.05	31 ± 5
	edge	$\frac{8.9 \pm 0.2}{9.6 \pm 0.2}$	$\frac{3.5 \pm 0.2}{4.0 \pm 0.2}$	14.8 ± 0.05	12.9 ± 0.5	0.1 ± 0.05	34 ± 5
$v10w1$	center	$\frac{25.5 \pm 0.5}{27.0 \pm 0.5}$	$\frac{7.4 \pm 0.2}{9.6 \pm 0.2}$	15.0 ± 0.05	10.6 ± 0.5	8.6 ± 0.05	48 ± 5
	mid-rad	$\frac{7.5 \pm 0.5}{15.5 \pm 0.5}$	$\frac{2.2 \pm 0.2}{1.7 \pm 0.2}$	38.8 ± 0.05	18.3 ± 0.5	0.1 ± 0.05	56 ± 5
	edge	$\frac{1.7 \pm 0.2}{3.6 \pm 0.2}$	$\frac{1.5 \pm 0.2}{1.1 \pm 0.2}$	41.8 ± 0.05	19.0 ± 0.5	0.2 ± 0.05	276 ± 5
$v1w1$	center	$\frac{1.4 \pm 0.1}{1.2 \pm 0.1}$	$\frac{0.8 \pm 0.1}{0.8 \pm 0.1}$	25 ± 0.05	14.0 ± 0.5	0.4 ± 0.05	132 ± 5
	mid-rad	$\frac{0.8 \pm 0.1}{0.9 \pm 0.1}$	$\frac{0.6 \pm 0.1}{0.4 \pm 0.1}$	33 ± 0.05	16.0 ± 0.5	0.6 ± 0.05	197 ± 5
	edge	$\frac{0.7 \pm 0.1}{0.7 \pm 0.1}$	$\frac{0.6 \pm 0.1}{0.4 \pm 0.1}$	61 ± 0.05	30.5 ± 0.5	0.2 ± 0.05	189 ± 5

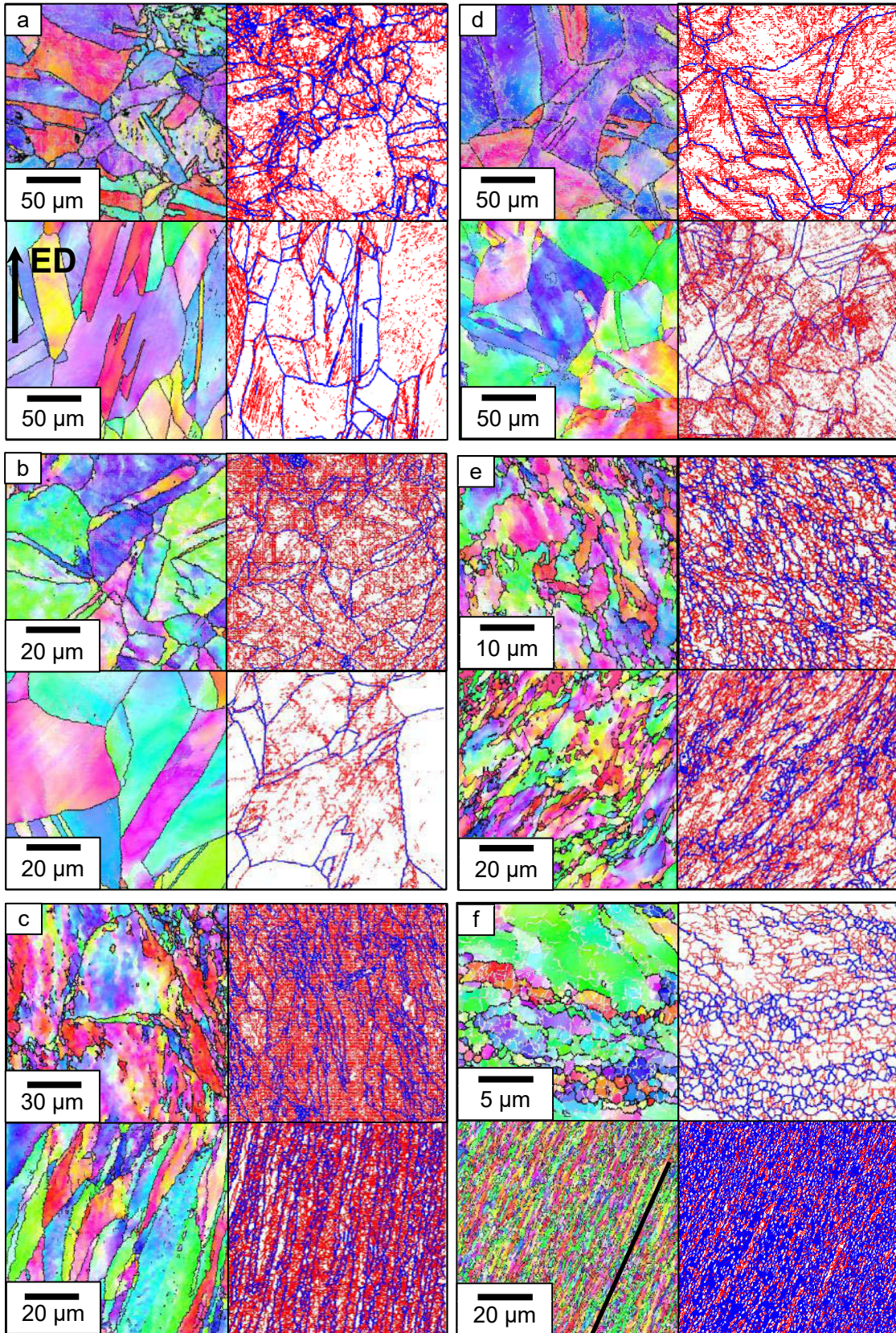


Figure 5.2 The OIM maps (left) and grain boundaries maps (right) of the $v10w0$ (a-c) and $v10w1$ (d-f) regimes are shown for both transversal (above) and longitudinal (bottom) sections of the sample areas after HPTE at 100°C . OIM and GB maps, above or bottom, represent the neighbor sites of the microstructure. These maps corresponds to the center (a, d); mid-radius (b, e); and edge regions (c, f). In the OIM maps, coloring represents the projection of the ED in the inverse pole figure. In grain boundaries maps, high angle misorientations ($\theta > 15^{\circ}$) are marked with blue lines, while low angle misorientations ($2^{\circ} < \theta < 15^{\circ}$) are marked with red lines.

The average grain size after the $v10w0$ and $v10w1$ HPTE regimes remains in the micron-range. Near the center of the billet processed with the $v10w0$ regime, the average grain size ranged from $21.5 - 23.5 \pm 0.5 \mu\text{m}$, while after processing with the $v10w1$ regime, it ranges from $25.5 - 27.0 \pm 0.5 \mu\text{m}$ (Table 5.1). The elongation of the grains in the longitudinal section, along with their equiaxed shape in the transverse cross section, indicates ellipsoid-like grain shape aligned in the direction of the extrusion in the central part of the sample processed with the $v10w0$ and $v10w1$ HPTE regimes (Table 5.1).

The fraction of low angle grain boundaries after the $v10w0$ regime was relatively high, ranging from about 78% to 83% (Table 5.1). However, for the samples processed in the $v10w1$ HPTE regime, the fraction of LABs ranged from 68% to 84% (Table 5.1).

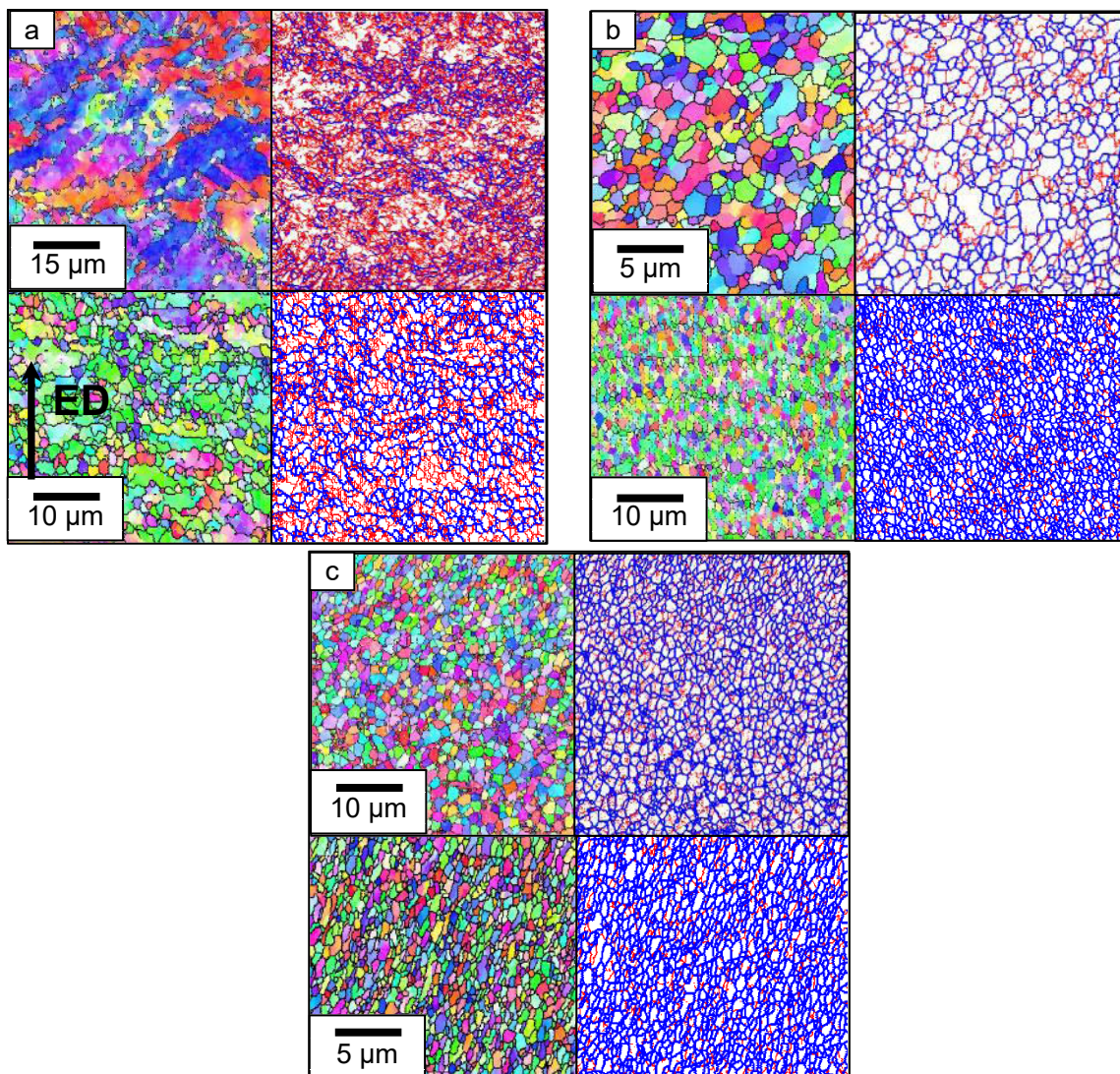


Figure 5.3 OIM maps of the $v1w1$ in the transversal (above) and longitudinal (bottom) sections of the sample are shown at (a) the center; (b) the mid-radius; and (c) the edge, after HPTE at 100°C . The coloring in the OIM map corresponds to the projection of ED in the inverse pole figure. In the grain boundaries maps, high angle misorientations ($\theta > 15^\circ$) are marked by blue lines, and low angle misorientations ($2^\circ < \theta < 15^\circ$) are marked by red lines.

The number of twin boundaries decreases compared to that in the initial state after both the $v10w0$ and $v10w1$ HPTE regimes. Furthermore, there was a significant decrease in the

volume fraction of HABs, dropping from 90% (note that misorientations $\theta < 2^\circ$ were neglected) in the initial state to 10-20 % after HPTE (Table 5.1). Such a strong change in the fraction of HABs was accompanied by a slight increase in the dislocation density from 11×10^{12} to $20\text{-}50 \times 10^{12} \text{m}^{-2}$ (Table 5.1) and no observable grain growth. This indicates that strain accumulated in the central area of the billet after both HPTE regimes $v10w0$ and $v10w1$ was not sufficient for substantial change of grain size. Generally, the microstructure of copper after the $v10w0$ and $v10w1$ regimes looked very similar to that of copper processed by conventional industrial deformation schemes.

The $v1w1$ regime of HPTE resulted in more pronounced changes in the microstructure of the central part of the billet (Figure 5.3 a). Notably, grains appeared not only refined (with a grain size of 1.2-1.4 μm), but also equiaxed in both normal and longitudinal cross sections after this treatment. The average grain sizes were very similar in both cross sections in the central area (Table 5.1, Figure 5.3 a), in contrast to the microstructure formed after treatment in the $v10w0$ and $v10w1$ regimes (Table 5.1, Figure 5.3 a, d). Microstructure investigations revealed that the $v1w1$ regime allowed for maximal grain refinement in copper billets among the applied HPTE regimes. Therefore, more detailed quantitative microstructure data for this regime is described below.

The microstructure in the central area of the copper billet after the $v1w1$ HPTE regime in the transversal section was significantly different compared to the microstructures in these areas after the $v10w0$ and $v10w1$ regimes. It represented a mixture of CG and FG structures (Figure 5.3 a).

The D_{15} grain size distribution in the transverse section of the central area showed a bimodal distribution with two peaks: one at 16.7 μm for coarse grains and another at 1.2 μm for fine grains (Figure 5.3 a, Figure 5.4 a).

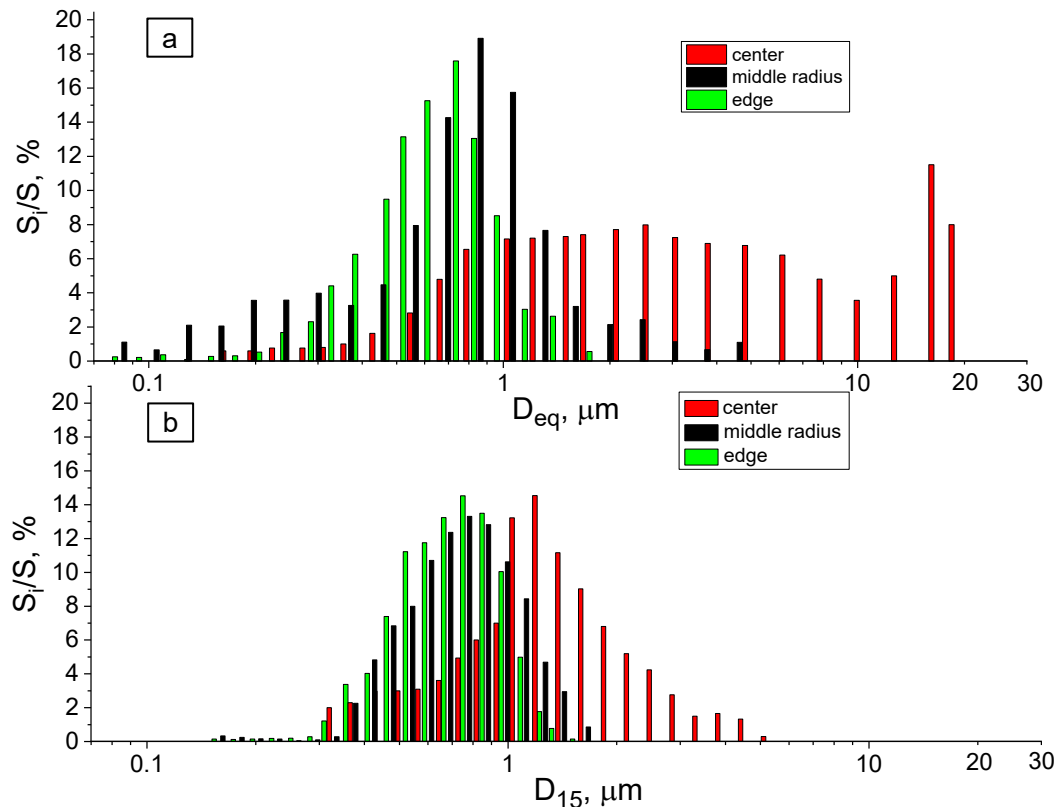


Figure 5.4 Grain size distribution (D_{15}) based on the specific area of the grains (S_j/S) after the $v1w1$ regime at 100°C in the transversal (a) and longitudinal (b) sections.

The specific area ratio between these two fractions was 1:3. In the longitudinal section, the grain size distribution followed a lognormal pattern. The average grain size in this section was 1.4 μm , which matched the peak of the histogram (Figure 5.4 b).

According to the EBSD data, the GB misorientation histograms were bimodal in both sample sections, with one maximum close to 2° in the low angle range and the second one at 47° – 48° in the high angle range (Figure 5.5). The volume fraction of HABs in the longitudinal cross section was larger than that in the transverse cross section (41% vs. 25%, see Table 5.1 and Figure 5.5 a, b). This difference in the volume fraction can be explained by the grain morphology; specifically, the coarse grains, containing numerous LABs, were elongated in the transverse section (Figure 5.5 a).

The grain size determined at the 3° boundary misorientation threshold, D_3 , was 0.8 μm in both cross-sections, whereas D_{15} in the longitudinal section was four times smaller than that in the transverse section (refer to Figure 5.5). Due to this difference in the D_{15} value, the volume fraction of HABs in the longitudinal section was larger compared to that in the transverse section.

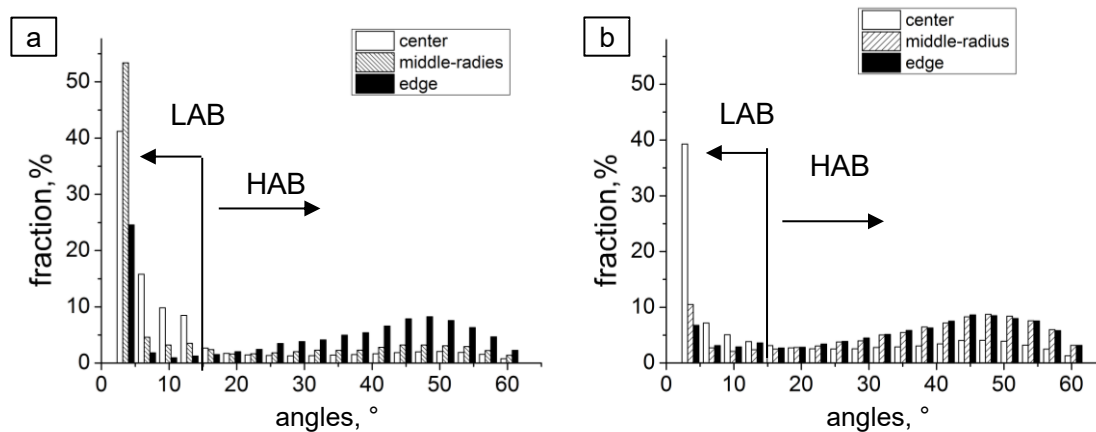


Figure 5.5 Misorientation distributions of the boundaries of crystallines after the $v1w1$ regime at 100°C in the (a) transversal and (b) longitudinal sample sections.

The grain size determined at the 3° boundary misorientation threshold, D_3 , was 0.8 μm in both cross-sections, whereas D_{15} in the longitudinal section was four times smaller than that in the transverse section (refer to Figure 5.5). Due to this difference in the D_{15} value, the volume fraction of HABs in the longitudinal section was larger compared to that in the transverse section.

5.1.1.2. Microstructure in the middle-radius area of the billet

In contrast to the central area of the billet, the $v10w0$ and $v10w1$ HPTE regimes resulted in the formation of different kinds of grain structures the middle-radius region (Figure 5.2 b, e). The microstructure at the middle-radius of the billet processed by the $v10w0$ regime was coarse-grained and similar to that in the central area. In the middle-radius area after the $v10w1$ regime, the microstructure consisted of a mixture of coarse and fine

grains. Furthermore, the grain size in the middle-radius region after the $v10w1$ regime was much smaller in the longitudinal section than that in the transverse one (Figure 5.2).

In contrast to the inhomogeneous microstructure observed in the central part of the processed sample, the grain structure after the $v1w1$ regime in the middle-radius region was rather uniform. Both average grain sizes, D_{15} and D_3 , were significantly smaller than those in the central area (Figure 5.4 a), and the grains were equiaxial (Figure 5.4 b).

The mid-radius area was most important for the analysis of mechanical properties due to the geometry of the tensile test samples (Figure 3.13). This area represented the periphery area in the tensile sample's gauge and, together with the central area, determined the tensile strength of the sample. Therefore, detailed EBSD-SEM and ACOM-TEM analysis were performed specifically for the middle-radius area of the sample processed by the $v1w1$ regime.

The BF TEM image shown in Figure 5.6 a illustrates the grain substructure of copper after HPTE in the mid-radius area. The majority of triple junctions had contact angles close to 120° (Figure 5.6 a, b).

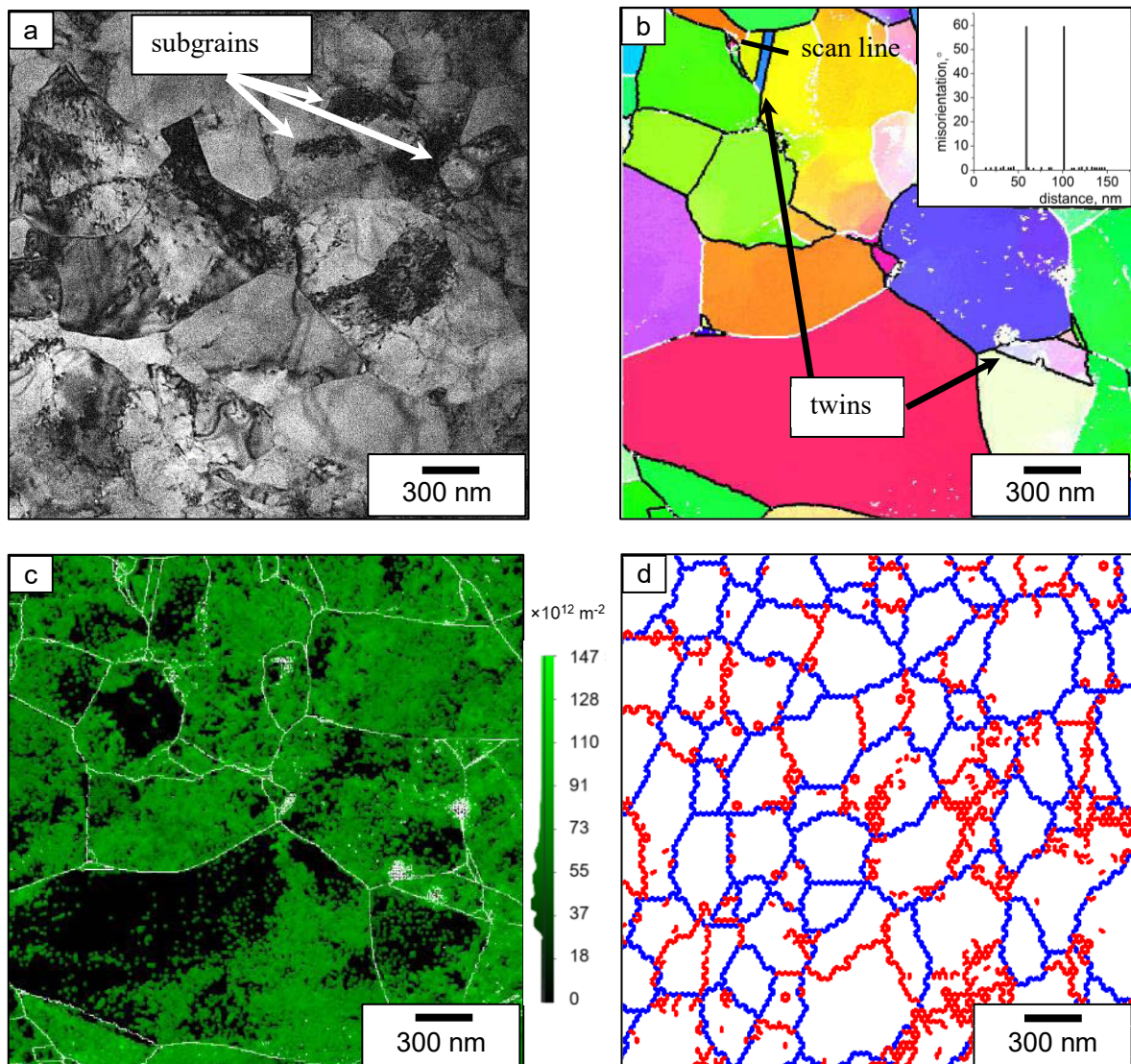


Figure 5.6 The microstructure of HPTE Cu in the mid-radius area of the longitudinal section of the billet subjected to the $v1w1$ regime is depicted in the following images, all at the same scale. (a) TEM BF image; (b) ACOM TEM OIM map, highlighting LABs ($3^\circ < \theta < 15^\circ$) with white lines and HABs ($\theta > 15^\circ$) with black lines; (c) GND distribution map from ACOM TEM, with all GBs marked by white lines; (d) EBSD OIM GBs network, with LABs marked by red lines and HABs marked by blue lines.

Some grains contained a higher dislocation density compared to that of the adjacent grains, as manifested by the diffraction contrast in the image. In general, the TEM observations were consistent with the EBSD maps with respect to the grain size values (Table 5.1).

The grain size histograms for the transverse and longitudinal sections demonstrated similar lognormal distributions. The peaks in both distributions corresponded to $0.8 \pm 0.1 \mu\text{m}$ in the transverse and $0.9 \pm 0.1 \mu\text{m}$ in the longitudinal sections (Figure 5.4). However, in the transverse section, the number of very small grains with sizes less than $0.3 \mu\text{m}$ was larger than that in the longitudinal section (Figure 5.4). Upon closer examination of the distribution in the region of large grains, it was observed that the grain size distribution, specifically for grains in the range of $3 \mu\text{m} < D_{15} < 6 \mu\text{m}$, was broader in the transversal section, whereas no grains larger than $3 \mu\text{m}$ were observed in the longitudinal section (Figure 5.4). Therefore, it can be concluded that the grain structure in copper after HPTE in the mid-radius area was quite similar in both transverse and longitudinal sections, which was not the case for the sample's central region.

The differences in grain size and grain size distribution provided evidence that the HPTE created conditions for efficient grain refinement in the middle-radius region, resulting in a smaller grain size than that in the central region of the sample (Table 5.1).

Examination of the copper microstructure after HPTE in the middle-radius area was performed using ACOM TEM, which provided additional microstructural details. The grain substructure was examined in detail using the BF images shown in Figure 5.6 a. A corresponding orientation map is displayed in Figure 5.6 b, whereas a GND spatial distribution is shown in Figure 5.6 c. It should be noted here that twins were observed inside the ultrafine grains, which was the reason for the characteristic peak at 60° in the boundary misorientation histogram (see Figure 5.5 b). The volume fraction of the twin-type boundaries was 14%, while the OIM maps obtained by the EBSD method contained only 0.6% of such boundaries (Table 5.1). Most probably, this difference results from the different statistics of the grains in the microstructure obtained by the ACOM TEM and EBSD methods. Since the number of grains analyzed using SEM was at least several thousands, the data obtained by SEM can be considered more reliable. The STEM scanning field contained just a few grains, thus characterizing only a small part of the microstructure.

The volume fraction of HABs in the longitudinal section was higher than that in the transverse one (49% and 33%, respectively, Table 5.1). This difference was similar to the difference found in the central area and was most likely due to the same grain refinement mechanism.

The average thickness of twins was of about 40 nm (Figure 5.6 b, d), and the average twin size, estimated using the equal circles method, was of about 110 nm, i.e., smaller than the measured grain size ($D_3 = 250 \text{ nm}$). The nano-sized twins and grains less than 50 nm could not be resolved in SEM using 50 nm step size. Figure 5.6 a, b shows that a high number of very small subgrains bounded by LABs were present in the HPTE-processed sample. In general, the majority of grains bounded by HABs (and marked with blue lines in Figure 5.6 d) contained one or more LABs.

As seen in the ACOM TEM maps (Figure 5.6 b, c), many twin-type GBs were formed during the HPTE deformation within the fine grains, thus dividing them into smaller grains. The GND density differed significantly in neighboring (sub)grains (Figure 5.6 c). This means that both LABs and twin-type GBs provided effective barriers for dislocation slip, and they should be taken into account in the analysis of possible strengthening factors, particularly Hall–Petch strengthening. Since the volume fraction of twin boundaries increased from the sample’s center towards the edge (Table 5.1), it can be concluded that twinning was more active at higher strains. From the nano-twins morphology, it is hypothesized that twinning occurred in the newly formed small grains.

5.1.1.3. *Microstructure in the edge area of the billet*

The microstructure of the billet after the *v10w0* regime in the edge area was rather heterogeneous. In a thin layer close to the surface, grains were strongly elongated in the ED (Figure 5.2 c, bottom right image). The thickness of this layer was only about 50 μm . The grains were much coarser towards the center of the billet (Figure 5.2 c, bottom left image). This indicated that in the surface layer, the strain was very high during extrusion via the *v10w0* HPTE regime, as predicted by the FEM calculation (Table 4.1). After the *v10w1* regime, the microstructure in the whole edge area of the billet became fine-grained ($D_{15} = 1.7/3.6 \mu\text{m}$), and the grains were strongly elongated (Figure 5.2 f). As seen in Figure 5.2 e, grains were elongated in direction tilted 20-25° to the ED.

The principal difference in the microstructure of the copper billet subjected to the *v10w0* and *v10w1* HPTE regimes in the edge area was the prevalence of the fraction of HABs over the fraction of LABs in the second case ($V_{>15^\circ} = 69\%$ after the *v10w1* regime and $V_{>15^\circ} = 26\%$ after the *v10w0* regime, Figure 5.2 c, f and Table 5.1). Additionally, the GND density reached a value of $276 \times 10^{12} \text{m}^{-2}$, which was more than five times higher than the GND density in the edge area after the *v10w0* regime (Table 5.1).

The structure at the sample’s edge after the *v1w1* regime consisted of ultrafine equiaxed grains (Figure 5.3 c). The average grain size D_{15} in this location was still higher than D_3 and became slightly smaller than that in the middle-radius region (Table 5.1). Grain size distribution histograms for the transversal and longitudinal sections were similar to those of the mid-radius area. The distributions were log-normal with a maximum at 0.7 μm in both sections (Figure 5.4 a, b). GB misorientation distributions showed that the fractions of HABs in the transversal and longitudinal sections were 61% and 79%, respectively. These values were much higher than the fractions of HABs in both the central and middle-radius regions (Table 5.1).

5.1.2. **Dislocations density**

From the center to the edge of the HPTE-processed sample, the GND density of copper after the *v1w1* regime was 10 times higher compared to that of the annealed material, gradually increasing from 100×10^{12} to $130 \times 10^{12} \text{m}^{-2}$ (Figure 5.7).

The total dislocation density (dd) derived from XRD measurements was higher ($150 \times 10^{12} \text{ m}^{-2}$ in the central region and $300 \times 10^{12} \text{ m}^{-2}$ at the edge, Figure 5.7), suggesting that X-ray diffraction data accounted for both GND and SSD.

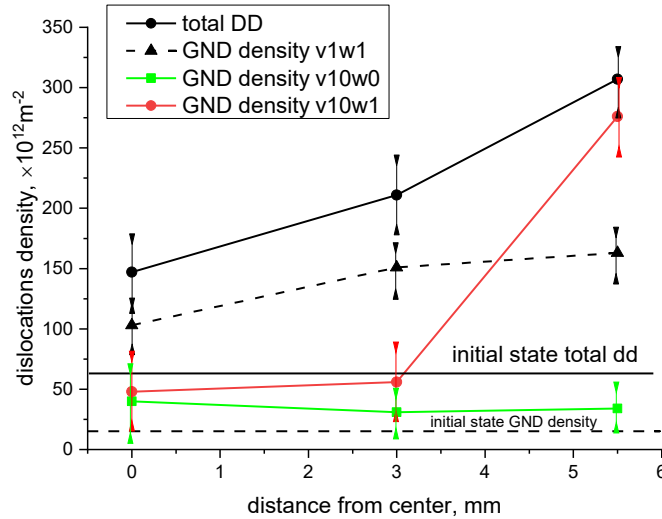


Figure 5.7 The distribution of dislocation density in the Cu sample before and after various HPTE regimes at 100°C.

HPTE processing with $v10w0$ regime, as well as with the $v10w1$ regime in the center and middle-radius area of the specimen, resulted in a lower GND density compared to that in the edge area (Figure 5.7). The GND density of the copper sample subjected to the $v10w1$ regime was very similar to that after the $v1w1$ regime.

5.2. Discussion of the microstructure of the HPTE - processed copper

In the central and middle-radius region of the billet processed at 100°C with the $v10w0$ and $v10w1$ regimes, a columnar CG structure was formed, with grains predominantly elongated in the extrusion direction and a high density of low angle boundaries. A similar microstructure was obtained after the $v10w0$ regime performed at room temperature [12] and after one pass of CEE process [122, 123], which was analogous to the extrusion regime at HPTE. Close to the specimen edge, elongated areas with a similar orientation in the extrusion direction (similar coloring with smooth transitions in color contrast) appeared (Figure 5.2 c), indicating stronger material flow in these specimen areas, which was related to the friction forces. Comparing the results of the strain calculation for the $v10w0$ regime at room temperature and at 100°C (Table 4.1), it can be concluded that an increase in the deformation temperature at HPTE led to a decrease of the accumulated strain. This resulted in the formation of a thin layer of strongly elongated grains in the edge area of the processed billet (Figure 5.2 c). A similar area of strongly elongated grains was observed in the copper billet after deformation at room temperature under the $v10w0$ regime [12].

The microstructure in the center of the $v1w1$ specimen was less refined than that in the central area of the specimens after the $v10w1$ and $v10w0$ regimes and consisted of elongated grains with irregular shape and a large number of LABs inside of the grains.

The microstructure study demonstrated that the $v1w1$ regime of the HPTE deformation carried out at 100°C resulted in the formation of a gradient microstructure in copper. This was not surprising since HPTE combined both extrusion and shear deformation modes. The shear mode gradually increased from the sample's center towards the edge (Equation 2.12). Consequently, the central zone of the HPTE-processed sample with the $v1w1$ regime was characterized by the presence of a fine-grained structure, whereas the mid-radius and edge areas were characterized by an ultrafine-grained structure. Apparently, large grains were gradually refined with an increasing strain, resulting in an increased fraction of fine grains, as shown in Figure 5.3 a. Even in the central area of the HPTE sample, the majority of grains (about 80-85%) are the refined grains with sizes in the range of $\sim 2\text{--}5\ \mu\text{m}$ (Figure 5.3 a). In this area, low angle boundaries were formed, and the difference between D_{15} and D_3 became significant (Table 5.1).

At a larger distance from the center, the applied strain increased, and the rate of new GBs formation became smaller, as both grain sizes D_3 and D_{15} were practically the same at the mid-radius and at the edge, indicating no further grain refinement. This suggests that a saturation of grain size refinement was reached, which has also been observed for other SPD methods [7, 53-55]. Following the saturation of grain refinement saturation, the misorientations at the already formed interfaces grew resulting in an increase in the fraction of HABs (Figure 5.4). It is noteworthy that this increase occurred at different rates on different grain facets, and the difference between D_{15} and D_3 still persisted up to the highest strain reached in the experiment. GB distribution maps shown in Figure 5.6 d clearly demonstrated that the microstructure in all sample areas was complex, with interpenetrated networks of LABs and HABs. In other words, a crystallite (grain or subgrain) could be simultaneously bounded by both high angle and low angle boundaries. Interestingly, the density of SSD showed a higher increase at the edge of the HPTE-processed sample compared to that of GND (Figure 5.7). This fact suggests that the multiplication rate of SSD was higher than their recovery/annihilation rate at the edge (as well as in the mid-radius area) compared to the kinetics of the same processes in the central area. The difference in density for both kinds of dislocations (GND and SSD) was consistent with the previously published data [104]. This data showed that in well-annealed metallic materials, the GND density was 20-30% lower than the total dislocation density. Additionally, the GND and SSD densities were found to be strongly correlated.

The mean grain size in the edge area of the billet after the $v1w1$ regime at 100°C was $0.7\ \mu\text{m}$, which was slightly smaller than that in the middle-radius area ($0.85\ \mu\text{m}$), despite a significant difference in the accumulated strain (22.8 at the edge and 15.0 at the middle of the radius according to Equation (2.12)), which points towards the saturation of grain refinement, in agreement with previous reports [7, 53-55]. When using the $v1w1$ HPTE regime at room temperature for the deformation of copper billets, the authors of [12] obtained a gradient structure with a CG microstructure in the central part and a uniform UFG microstructure with equiaxed grains and a mean grain size of $0.35\ \mu\text{m}$ in the rest of the sample, which was 2.5 times smaller than the grain size obtained in the present work. Therefore, the value of

saturated grain size depended on the deformation temperature, as demonstrated for pure nickel in [53] (Figure 2.5).

The microstructure resulting from the HPTE processing regime $v1w1$ exhibited similar features to the gradient microstructure of Cu after free-end torsion [124, 125]. Nevertheless, several distinctions should be mentioned here. HPTE provided a more efficient grain refinement compared to that achievable with free-end torsion. Furthermore, instead of a coarse-grained structure in the center and a fine-grained structure at the periphery, FG was observed at the center and UFG structure at the periphery after HPTE. After the HPTE $v1w1$ regime, a more homogeneous grain structure throughout the entire sample with no grain elongation, as observed after the free-end torsion, was revealed.

Based on the microstructure investigations of copper samples in the center, middle-radius, and edge region after the $v10w0$, $v10w1$ and $v1w1$ regimes, it can be concluded that the gradient structure illustrated in Figure 2.1 b and considered by Beygelzimer et al. in [35] was formed in the copper billets after the $v10w1$ and $v1w1$ regimes. It should be noted that the edge area of the billet is removed during the machining of the sample gauge, as shown in (Figure 3.13). The types of microstructures formed after HPTE processing in the copper billets, were summarized in Table 5.2.

Table 5.2 The types of resulting structures in the copper samples subjected to the HPTE at 100°C.

State/area	center	middle-radius	edge
initial	CG		
$v10w0$	CG	CG	CG/FG
$v10w1$	CG	CG/FG	FG
$v1w1$	CG/FG	UFG	UFG

It was observed that after the $v10w1$ HPTE regime, a combination of CG structure in the center of the sample and a mixture of CG/FG structure at the periphery of the gauge was obtained. On the other hand, after the $v1w1$ regime, a mixture of CG and FG structures was formed in the center, while a UFG structure was presented at the periphery of the gauge. Therefore, these samples with gradient structures could be utilized for the analysis of tensile properties of large-scale samples with gradient structure.

5.3. 3D configurations of hybrid samples after HPTE

5.3.1. Initial configurations

In order to characterize the 3D geometry of the hybrid samples, X-Ray tomography measurements on sample configurations before and after HPTE were performed in collaboration with Prof. L. Toth at the University of Lorraine. Figure 5.8 displays the 3D reconstruction of the hybrid samples, containing aluminum wires embedded in a copper matrix. The 3D images of the initial states of configurations (1) and (2) (Figure 3.4) are shown in Figure 5.8. Different colors (blue, yellow and green) represent the aluminum wires in an isometric view. Examination of the 3D images revealed the complete continuity of the Al wires, suggesting homogeneous deformation without fracture during direct extrusion (Figure 5.8). The wire length remains equal to the length of the initial hybrid sample, namely 35 mm.

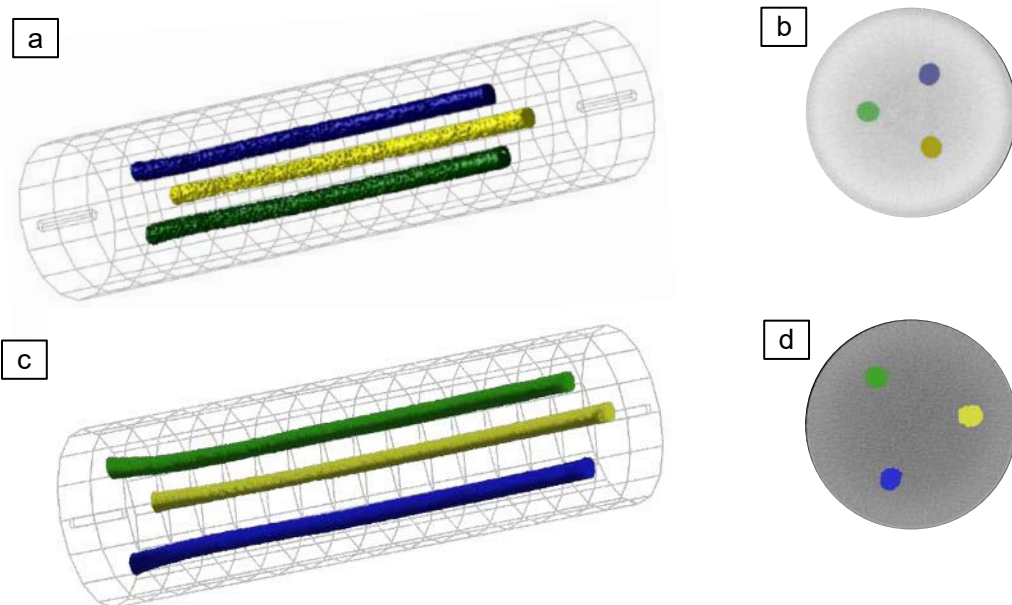


Figure 5.8 The 3D reconstruction of the initial samples in configurations (1) (a, b) and (2) (c, d). XRD tomography was conducted using ORS Dragonfly reconstruction software.

At the bottom of the sample in configuration (2), the ends of the wires (last ~2-3 mm) exhibited slight bending. A meticulous investigation of the joints between the Al wires and the Cu matrix in the configuration (1), using optical and scanning electron microscopy, revealed a good fit and no flaws between the two materials (Figure 5.9 a). EDS analysis displayed a sharp transition from Cu to Al along the scan line in the transversal section (Figure 5.9 b).

Furthermore, SEM observation of the Cu/Al hybrid sample in the longitudinal section revealed a good fit at the interface boundary with slight bending along the ED (Figure 5.9 c). The curved shape of the junction is expected to enhance friction at the interface and prevent slipping of the wire in the matrix. This, in turn, provides improved conditions for joint deformation during subsequent HPTE processing.

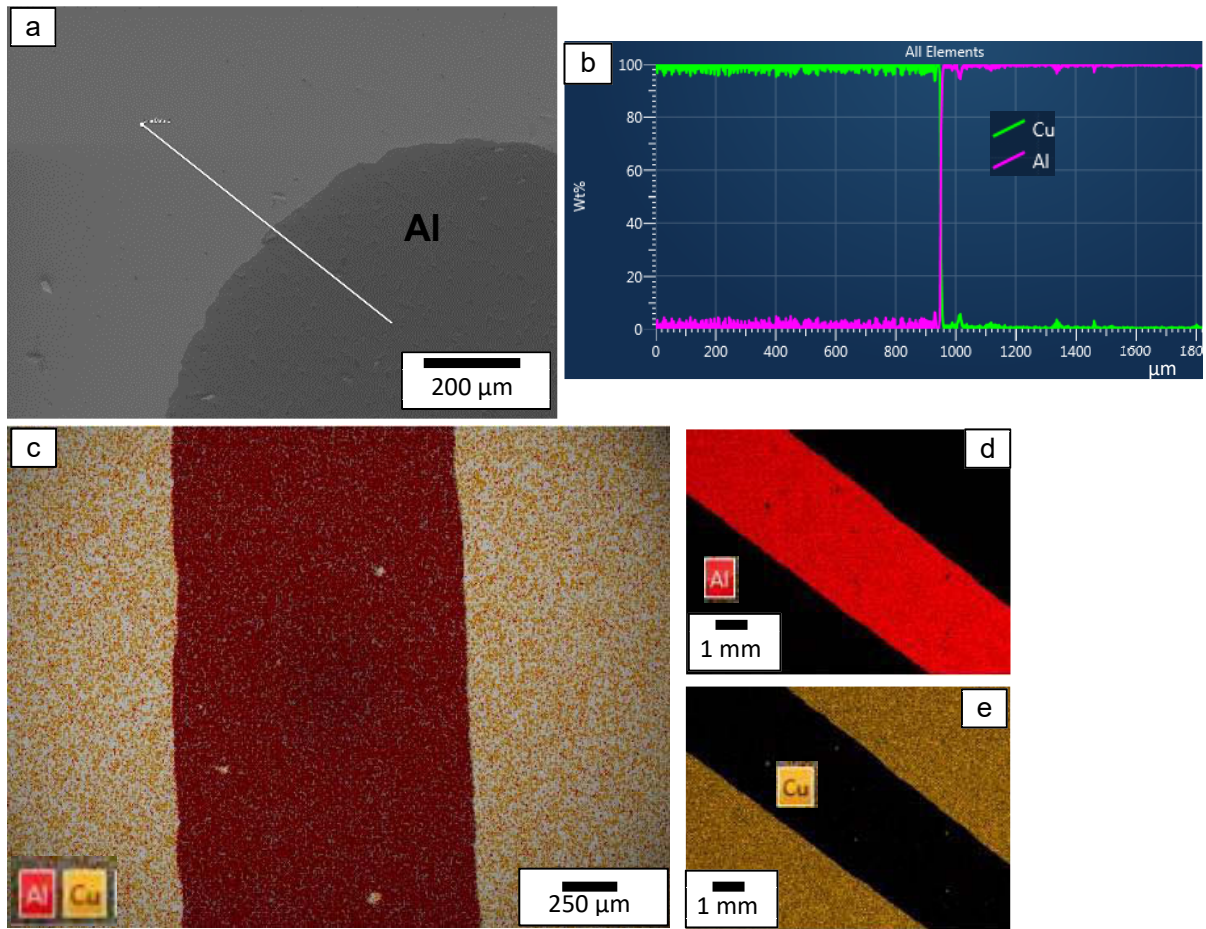


Figure 5.9 The interphase boundary in the Cu-Al hybrid samples in configuration (1) after DE at 250°C. The figure consist of transversal (a, b) and longitudinal (c-e) sections. Image (a) displays secondary electron images, image (b) exhibits the EDS detector-induced signal along the scan line, and images (c-e) present mapping data.

Two additional configurations, comprising CP Cu-matrix and three iron wires with 99.9 at.% purity, were also prepared following a similar procedure as was used for the Cu-Al hybrid samples in configurations (1) and (2), except that 20 mm samples were extruded at 400°C.

5.3.2. HPTE processing of hybrid samples

5.3.2.1. Configurations designed for the tensile tests

The inspection of the 3D images of the wires after the $v18w1$ and $v6w1$ regimes did not reveal any discontinuity of Al wires. The latter serves as a demonstration that even after experiencing large strains, the wires deformed homogeneously without fracturing (Figure 5.10).

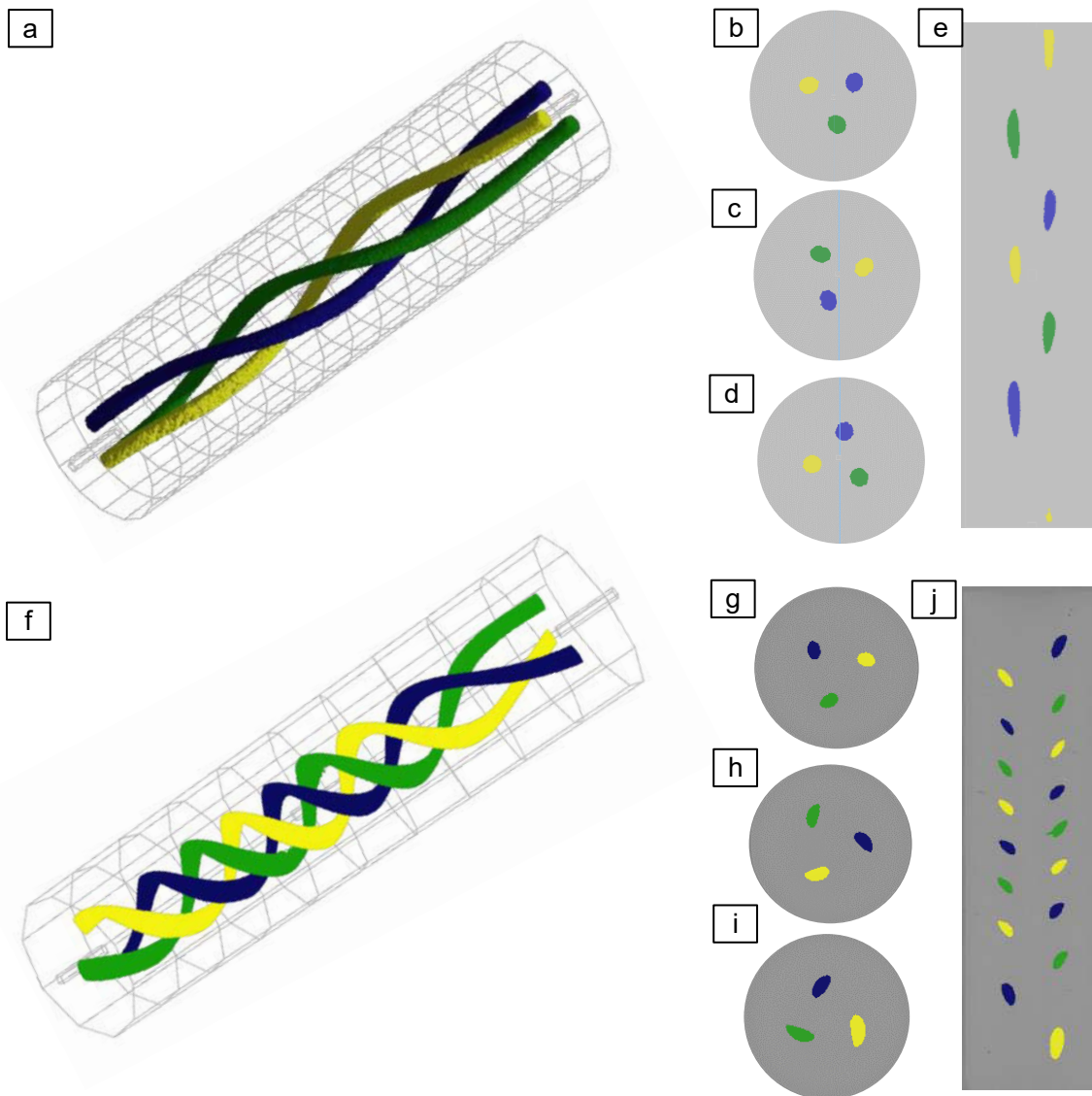


Figure 5.10 X-ray tomography of the samples in configuration (1) after the $v18w1$ (a-e) and $v6w1$ (f-j) regimes conducted at 100°C . 3D (a, f) and 2D (b-e, g-j) images were produced using ORS Dragonfly reconstruction software. The 2D images in the transverse section (b-d, g-i) were captured from the top (b, g), middle-height (c, h) and bottom (d, i) sections. The 2D images in the longitudinal section (e, j) were taken along the diameter of the billet.

Initially, straight aluminum wires were twisted into helices. Additionally, HPTE caused a change in the cross sectional geometry of the wires from circular to elliptical, and the further the wire was from the billet axis, the thinner its cross section became. Wires subjected to the

$v18w1$ HPTE regime formed one loop over the entire length of the sample, while those subjected to the $v6w1$ formed three loops (Figure 5.10).

The deformation of the Fe wires was more homogeneous after the $v6w1$ HPTE regime (Figure 5.11 a, b). Due to the similar atomic weight of Cu and Fe, it was not possible to obtain a high quality XRD tomography of the Cu-Fe hybrid samples. Therefore, optical microscopy images of the longitudinal and transversal Cu-Fe sample cross sections were compared with the corresponding sections of Cu-Al hybrid samples after HPTE processing. Figure 5.11 illustrates the similar shape of the twisted wires in the Cu-Al (Figure 5.11 a, b) and Cu-Fe (Figure 5.11 c, d) hybrid samples after the $v18w1$ HPTE regime, indicating that the configuration of the Cu-Al hybrid samples shown in Figure 5.11 is identical to that of the Cu-Fe sample.

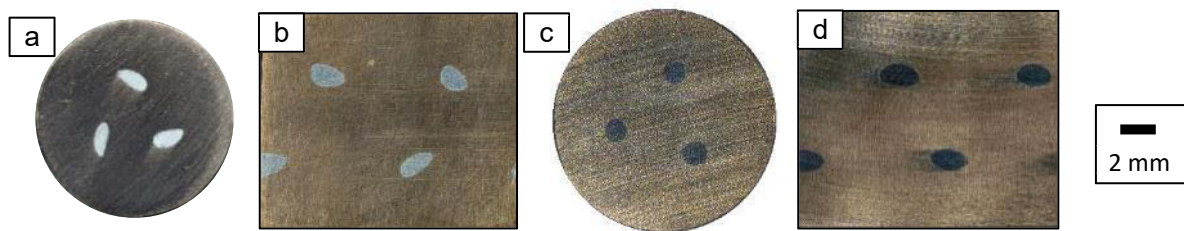


Figure 5.11 The transversal (a, c) and longitudinal (b, d) sections of the Cu-Al (a, b) and the Cu-Fe (c, d) hybrid samples after the $v18w1$ HPTE processing. The longitudinal section in the middle-part of the sample's height corresponds to the gauge of tensile sample.

Regarding the 3D configurations of the processed samples, it is important to note that for both HPTE regimes, the twisting of wires at the ends of the specimens was less pronounced (Figure 5.10). This was attributed to the non-uniform strain distribution along the extrusion direction in the HPTE-processed specimens.

5.3.2.2. Microstructure characterization of hybrid samples after HPTE

SEM observations were conducted on the joint between the embedded wires and the Cu matrix in the configuration (1) after HPTE with the $v6w1$ regime, as shown in Figure 5.12. The results revealed that in both Cu-Al and Cu-Fe deformed samples, the bonding between the Cu matrix and the Fe or Al wires was well-preserved.

Although small defects were observed between the two materials (indicated by the white dashed line in Figure 5.12 a), these defects accounted for less than 5% of the interfacial area. Consequently, they were unlikely to significantly impact the deformation behavior of the hybrid samples during tensile tests. Overall, SEM inspection demonstrated that the $v6w1$ regime conducted at 100°C resulted in nearly flawless bonding between the matrix and wires for both Cu-Al, as well as for the Cu-Fe hybrid samples.

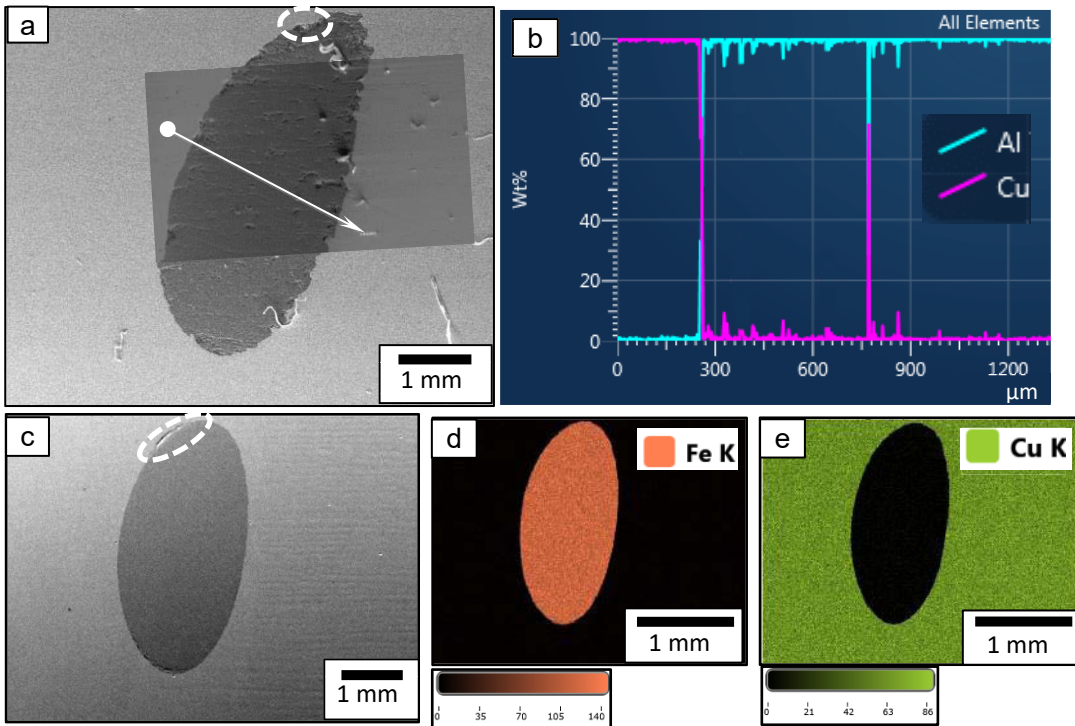


Figure 5.12 SEM image (a, c), EDS scan along the line (b) and mapping (d, e) of the Cu-Al (a, b) and Cu-Fe (c-e) hybrid samples after the *v6w1* HPTE processing. The longitudinal section in the middle-part of the sample height is presented.

EDS analysis showed a distinct and abrupt transition from Cu to Al along the scan line in the transversal sample section (Figure 5.12 b). Similarly, a sharp transition at the Cu-Fe interface was observed (Figure 5.12 d, e). Therefore HPTE-processed hybrid samples have a good fit in the junction area between the matrix and the embedded wires without forming a diffusion layer.

6. Mechanical properties of pure copper and helically architected hybrid samples

6.1. Mechanical properties of pure copper after HPTE

In agreement with microstructural observations and dislocation density measurements, the microhardness of the HPTE-processed copper increased from the initial value of 75 HV to 110 HV in the central area and to 125 HV at the mid-radius and sample edge (Figure 6.1 a). It can be observed that in samples subjected to the $v1w1$ regime, at a distance of approx. $0.4 R$ (2 mm) from the center, the microhardness reached a saturation value of approx. 125 HV and remained constant up to the specimen edge (Figure 6.1 a).

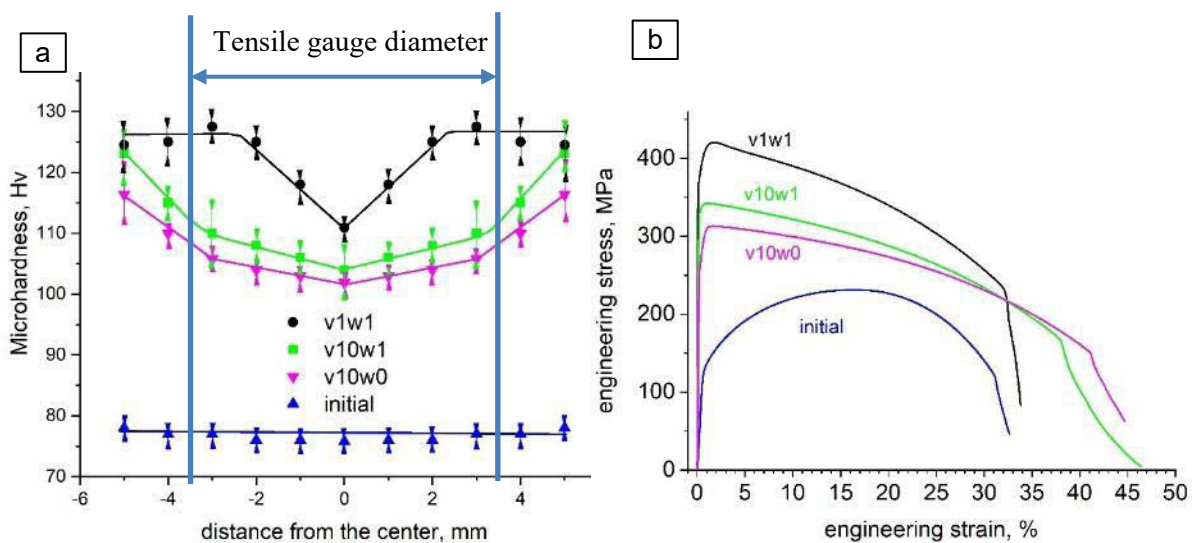


Figure 6.1 The microhardness distribution along the radius (a), and tensile curves of Cu (b) before and after the HPTE at 100°C.

Thus, based on the HV data, the Cu samples produced by the $v1w1$ regime comprised two distinct regions: (1) a central region extending up to approx. $0.4 R = 2.0$ mm (corresponding to an equivalent strain of approx. 8, as shown in Figure 4.2 b) with a gradually increasing microhardness, and (2) an outer region ($>0.4 R$) with a saturated microhardness value of about 125 HV. The tensile test samples had a gauge diameter of 6.85 mm, sampling both the central area and half of the outer area as indicated by the vertical line in Figure 6.1 a.

In contrast to the hardness distribution in samples subjected to the $v1w1$ regime, the samples subjected to the $v10w1$ and $v10w0$ regimes exhibited a gradual increase in HV in the center and middle-radius areas, and sudden growth in HV at the edge area (Figure 6.1 a). The samples subjected to the $v10w1$ regime were 3-8 HV harder than the samples subjected to the $v10w0$ regime (Table 6.1). Tensile samples machined from the billets processed by the $v10w1$ and $v10w0$ regimes contained a region with a gradually increasing microhardness from 101-104 HV to 105-110 HV (Figure 6.1 a).

Tensile tests showed that the HPTE method resulted in a more than twofold increase in the yield strength of Cu compared to the initial annealed state (370 MPa vs. 130 MPa), and a significant enhancement in ultimate tensile strength to 415 MPa. The total elongation of the

samples after the $v10w0$ regime reached 40%, which was 25% higher than that in the initial CG state. The states after the $v10w1$ and $v1w1$ regimes also exhibited a fairly high total elongation, albeit less than that after the $v10w0$ regime (Figure 6.1 b, Table 6.1).

Table 6.1 The tensile properties and microhardness of the copper before and after the HPTE conducted at 100°C.

State	YS, MPA	UTS, MPA	δ_{UTS} , %	δ , %	HV		
					center	mid rad	edge
initial	70	210	16.0	32	75	77	78
$v10w0$	250	310	1.5	40	101	105	116
$v10w1$	320	340	1.0	38	104	110	123
$v1w1$	370	415	1.8	35	110	125	123

The stress–strain curve of copper after HPTE at 100°C displayed rapid strengthening and a short uniform elongation range (Figure 6.1 b). Therefore a typical behavior for materials produced by SPD methods was observed, with a decrease in uniform elongation from ~16% in the annealed state to ~2% after HPTE deformation.

Table 6.2 The Vickers hardness (HV), yield strength (YS), ultimate strength (UTS), and elongation to failure (δ) of Cu after the HPTE and other SPD methods.

Process parameters	HV	YS, MPa	UTS, MPa	δ , %	source
soft rod ASTM		100	220	>5.0	ASTM B49-17
HPTE					
$v10w0$	105	250	310	40	this work
$v10w1$	110	320	340	38	
$v1w1$	125	370	415	35	
Free-end torsion					
1 revolution		312	333	~9	[124]
11 revolutions		387	458	~9	
16 revolutions		412	514	~10	
ECAP $e = 3$					
ECAP $e = 18$	41	382	404	2.1	[28]
HPT ½ turn	120	358	415	3.6	
HPT 10 turns	133	474	512	2.0	
	127	444	487	4.0	

However, after the deformation localized, the elongation to fracture reached 30%, which was twice as high as the post-necking elongation of the annealed copper (Figure 6.1 b).

Cu samples deformed via the $v1w1$ regime exhibited a yield strength and ultimate strength similar to the corresponding values obtained after free-end torsion with strain of 1.3 [124]. The elongation to failure of Cu after the $v1w1$ regime achieved 35%, which was more than 3.5 times higher than the elongation after free-end torsion.

The saturation value of microhardness at 125 HV closely corresponded to the microhardness of copper after HPT, as reported in reference [28] (Table 6.2). The strength of HPTE-processed copper was comparable to that of copper after ECAP but not as high as that after HPT [28].

Analyzing the change in microhardness along the radius of the Cu sample cross-section allowed to assess the contribution of different hardening mechanisms in HPTE processed samples (Figure 3.7). Specifically, the variation in hardness after HPTE treatment was influenced by the distribution of strain within the sample, which in turn affected dislocation density and the degree of grain refinement leading to Hall–Petch hardening [66].

6.1.1. Analysis of strengthening factors in HPTE-processed pure copper

The strength of the copper samples after HPTE was assumed to result from the following hardening mechanisms: accumulation of dislocations σ_ρ (Equation 2.8), Hall–Petch strengthening σ_{H-P} (Equation 2.9), solid solution strengthening σ_{SSS} (Equation 2.10), and second-phase particle strengthening σ_{SPPS} (Equation 2.11). The contributions to the hardening of solid solution and second phase particles are significant due to the presence of impurities and cannot be neglected.

The gauge of the tensile sample contained material from central and mid-radius areas. The microstructure in both areas was complex due to the presence of grains bounded by both HABs and LABs. Consequently, it was unclear which GB misorientation threshold and grain size should be used in Equation (2.9). A prior *in-situ* TEM study [67] had demonstrated that LABs with $\theta > 3^\circ$ and special GBs act as effective barriers for dislocation slip in FCC metals with low and middle stacking fault energy. It can be assumed that the effective grain size, d , in the Hall–Petch equation is equal to D_3 .

The parameters (σ_0 , k , α , G , b) used for computing the various strengthening mechanisms described above were taken from references [91, 126, 127], while the structure parameters D_3 , ρ , d_p , f , and C are provided in Table 5.1 and Table 6.3. The d_p values were measured in SEM-BSE images and the f and C values were obtained from SEM-EDX elemental analysis of pure copper before and after HPTE.

As shown in Table 6.4, the calculated contributions from solid solution and precipitation strengthening were small, accounting for less than 10% of the calculated YS (a similar estimate of the strength contribution is valid for UTS). Dislocation strengthening, on the other hand, was 3–4 times higher and contributed approx. 50% of the initial state YS_{calc} and only 20% of the YS_{calc} in the HPTE-processed copper. The reduced contribution of dislocation strengthening to YS_{calc} in the HPTE-processed copper is likely attributed to the elevated processing temperature of 100°C, which promoted dislocation density recovery. Consequently, the primary contribution (~60%) to the strength of HPTE-processed Cu is derived from GB strengthening through the Hall–Petch mechanism.

To compare the calculated YS_{calc} and the experimentally measured YS_M yield strengths of the entire HPTE-processed sample, the rule of mixture was employed. In terms of tensile strength parameters, Equation (2.1) can be rewritten as:

$$YS_M = YS_C V_C + YS_{MR} V_{MR}, \quad (6.1)$$

where YS_C and YS_{MR} represent the calculated values of the yield strength from the center and middle-radius area, respectively (Table 6.4). V_C and V_{MR} are the volume fractions in the according areas.

Table 6.3 The microstructure parameters of copper measured in the transversal section of the HPTE sample, which were used for the calculations of strengthening contributions.

Parameter	Initial	$v10w0$		$v10w1$		$v1w1$	
		center	mid-rad	center	mid-rad	center	mid-rad
$\rho^*, \times 10^{12} m^{-2}$	111	179 ± 17	108 ± 16	62 ± 57	275 ± 27	147	211
$d_p, \mu m$	6.1	6.1	6.1	6.1	6.1	1.2	1.2
$f, \%$	0.17	0.17	0.17	0.17	0.17	0.16	0.16
$C, at\%$	0.5	0.5	0.5	0.5	0.5	0.6	0.6

*Here ρ values were measured by X-ray peak broadening and C is the concentration of Al in Cu.

Based on the microhardness distribution along the radius of the HPTE-processed sample (Figure 6.1 a), the hardness is low in a narrow area with a radius of 1.2 mm around the billet axis. Hence, the volume fraction of this part of the tensile specimen is only 0.12, while the rest corresponds to the mid-radius area. The calculated value of $YS_M = 374.6$ MPa aligns well with the experimentally measured yield strength of 370 MPa. The outer part of the HPTE-processed sample characterized by high hardness and strength, was removed during the machining of the tensile specimen (Figure 6.1 a). Otherwise, the strength of the entire specimen would be even higher.

Table 6.4 The contributions (in MPa) of various strengthening mechanisms in Cu before and after the HPTE process conducted at 100°C.

Area		σ_0	$\sigma_{H-P D3}$	$\sigma_{H-P D15}$	σ_{SSS}	σ_{SPPS}	σ_ρ	YS_{D3}^*	YS_{D15}^*
initial		30	25.6	25.6	7.9	3.4	60.7	128.0	128.0
$v10w0$	center	30	29.8	30.1	1.8	17.3	74.0	190.8	169.3
	mid-rad	30	33.4	32.6	1.8	16.9	93.4		
$v10w1$	center	30	45.3	35.9	1.7	17.3	141.1	304.9	277.0
	mid-rad	30	106.4	73.4	1.8	16.9	169.7		
$v1w1$	center	30	156.5	88.3	8.9	17.3	69.8	374.6	307.7
	mid-rad	30	224.5	128.9	8.8	16.9	83.7		

* YS_{D3} , YS_{D15} are the values of yield strength, calculated by the mixture rule for grain sizes of D_3 and D_{15} .

The stress-elongation curve of copper after HPTE exhibits a short uniform elongation range. A typical behavior for materials produced by SPD methods is the decrease of uniform elongation from approx. 16% in the annealed state to around 2% after HPTE deformation. However, once the deformation is localized, the elongation to fracture reaches 30%, which is twice as high as the post-necking elongation of the annealed copper (Figure 6.1 b). Such behavior is characteristic of materials with an UFG microstructure [5, 52, 128] and is likely attributed to the increased strain rate sensitivity of such materials. Therefore, HPTE

processing of CP copper provides large elongation to failure and high strength, primarily due to the Hall–Petch mechanism. Despite the presence of a gradient microstructure, the uniform elongation was not improved as it was proposed in [51]. This can be attributed to the fact that both the central and outer layers of the HPTE-processed copper sample were sufficiently strengthened, resulting in the tensile behavior similar to that of the homogeneous UFG materials.

6.2. Mechanical properties of hybrid samples after HPTE

Tensile tests were performed for the configuration (1) (Figure 6.2) of the Cu-Al and Cu-Fe hybrid samples. At least three samples per state were pulled to fracture using the Zwick Proline universal testing stage with a 100 kN capacity. Typical tensile curves for the Cu-Al sample configuration (1) before and after HPTE processing via the *v6w1* and *v18w1* regimes were shown in Figure 6.2 a.

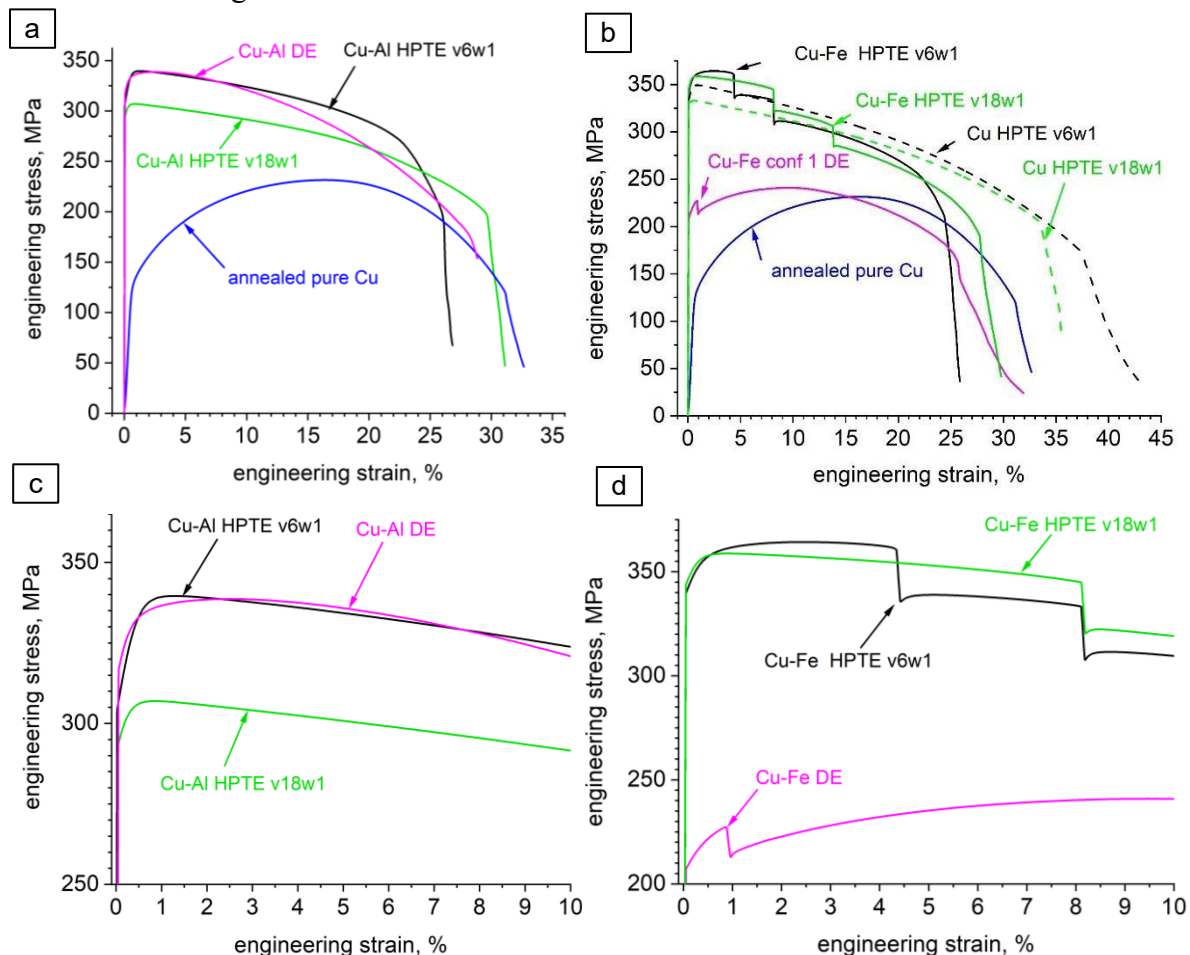


Figure 6.2 The tensile curves of copper, Cu-Al (a, c), and Cu-Fe (b, d) hybrid samples in the configuration (1) before and after the HPTE process.

The values of yield strength, ultimate tensile strength, uniform and total elongation are presented in Table 6.5. The uniform elongation was determined from the engineering curves in Figure 6.2 according to the Considere criterion (Equation (2.3)) governing the onset of localized deformation.

It was observed that the new architecture of the sample with spiral Al wires did not improve the tensile behavior with respect to uniform elongation. The values of YS and UTS of the hybrid samples were slightly lower than those of the Cu sample after HPTE processing (Table 6.5). The difference between the strength of Cu-Al hybrids and pure Cu corresponded to the specific volume of aluminum wires in the hybrid samples. Surprisingly, mechanical properties of the hybrid sample extruded at 250 °C (DE in Figure 6.2 a) were even better than those of the HPTE-processed one. YS was slightly higher, and uniform elongation δ_U was three times higher than that of the hybrid sample, i.e. 1.1% vs. 3.9% (Figure 6.2 a, Table 6.5). This result aligned well with the analytical description of tensile behavior of the hybrid material with serrated geometry (Figure 2.3 b) under uniaxial tension for several values of the inclination angle of the CG layers proposed in [44].

The mechanical behavior of the Cu-Fe hybrid samples was different from that of the Cu-Al hybrid samples. Figure 6.2 b, d show the typical tensile curves for the Cu-Fe samples in configuration (1) before and after HPTE processing. Additionally, a tensile curve for the annealed Cu sample is presented for comparison. The values of yield strength, ultimate tensile strength, uniform and total elongation were listed in Table 6.5. The tensile curve of the Cu-Fe hybrid sample extruded at 400 °C exhibited strain hardening until 1% strain, a small drop of the flow stress and then a long stage of strain hardening with a maximal elongation of 9.5%.

Table 6.5 The tensile properties of copper gradient samples, as well as the Cu-Al and Cu-Fe hybrid samples before and after the HPTE process.

	Sample / State	HV_{Cu}	HV_{wire}	YS , MPa	UTS , MPa	δ , %	δ_U , %
Cu	ann. 600°C 2 h	44	-	130±1	230±6	32±1	16.5±1
	$v18w1$, T=180°C	90	-	305±2	330±2	35±1	0.8±0.1
	$v6w1$, T=180°C	95	-	340±2	350±2	37±1	0.8±0.1
Cu-Al	DE 250°C	102	32	325±5	338±5	28±1	2.3±1
	$v18w1$, T=100°C	105	42	300±5	305±5	30±1	0.7±0.1
	$v6w1$, T=100°C	108	45	320±5	340±5	26±1	1.1±0.2
Cu-Fe	DE 400°C	80	220	215±2	240±5	30±1	9.5±1
	$v18w1$, T=180°C	91	230	350±5	360±5	28±1	0.8±0.1
	$v6w1$, T=180°C	95	233	350±5	365±5	24±1	3.9±1

The stress drop at a strain of approx. 1% likely occurred because all three Fe wires ruptured simultaneously.

The tensile behavior of the $v6w1$ hybrid sample with helical Fe wires was slightly improved compared to that of the homogenous one. After rapidly reaching the UTS point, the tensile curve of the HPTE-processed hybrid sample remained at this level of flow stress within a short range of strain (~3%), which was followed by two abrupt flow stress drops corresponding to the consequent rupture of Fe wires (Figure 6.2 b). YS of the hybrid Cu-Fe

sample was 25 MPa (7.7%) higher than that of homogenous Cu sample after processing under the same conditions. However, the main difference in the tensile properties of the hybrid samples compared to the homogenous ones was a significant improvement in uniform elongation: δ_U value after the $v6w1$ regime increased from 0.8% in pure copper to 3.9% in the hybrid Cu-Fe sample (Table 6.5).

Microhardness measurements were conducted on the Cu-Fe and Cu-Al hybrid samples, revealing a substantial hardening of the copper matrix. The microhardness increased from 44 HV in the annealed state to 90-95 HV after HPTE at 180 °C and 102-108 HV after HPTE at 100 °C (Table 6.5).

6.2.1. Analysis of the strain hardening rate of Cu and Cu-Fe hybrid samples

The strain hardening rate (SHR) θ normalized by true stress σ_t was calculated from the true stress-strain tensile curves for the Cu-Fe hybrid samples. True stress σ_t and true strain ε_t values were calculated from the engineering tensile curves demonstrated in Figure 6.2 b using the following equations:

$$\varepsilon_t = \ln\left(1 + \frac{\Delta l}{l}\right), \quad (6.3)$$

where $\frac{\Delta l}{l}$ is engineering strain, and

$$\sigma_t = \sigma_e(1 + \varepsilon_t), \quad (6.4)$$

where σ_e is engineering stress.

The strain hardening rate was determined as:

$$\theta = \left(\frac{\partial \sigma_t}{\partial \varepsilon_t}\right) \quad (6.5)$$

The plot of the strain hardening rate normalized to the true stress σ_t vs. the true strain is shown in Figure 6.3. The region of small strains is shown enlarged in Figure 6.3 for a detailed analysis of the strain hardening rate of hybrid samples before the onset of strain localization.

All three curves cross the $\theta/\sigma_t = 0$ value after a strain of 0.08, which is marked by a black vertical line in Figure 6.3 a. Actually, the calculation of the true stresses and strains after necking is a complicated task due to the formation of a non-uniaxial stress-strain state in the neck. The variation of the actual cross-section area of the sample should be monitored during the tensile test. Therefore, true strains and true stresses were calculated before the strain localization occurred.

Pure copper after the $v6w1$ and $v18w1$ regimes, and Cu-Fe hybrid samples after the $v18w1$ regime, demonstrated uniform elongation of 0.008 (Figure 6.3). The strain hardening rate of the hybrid sample processed by the $v6w1$ regime showed uniform elongation of 0.041 (marked by the vertical line in Figure 6.3). The true stress-true strain curves for the hybrid samples were calculated from the engineering tensile-strain curves in the range from the beginning of plastic deformation to the abrupt stress drop at the point when the first wire

ruptured (Figure 6.2 d). In this range, the deformation of the sample after the $v6w1$ regime is uniform.

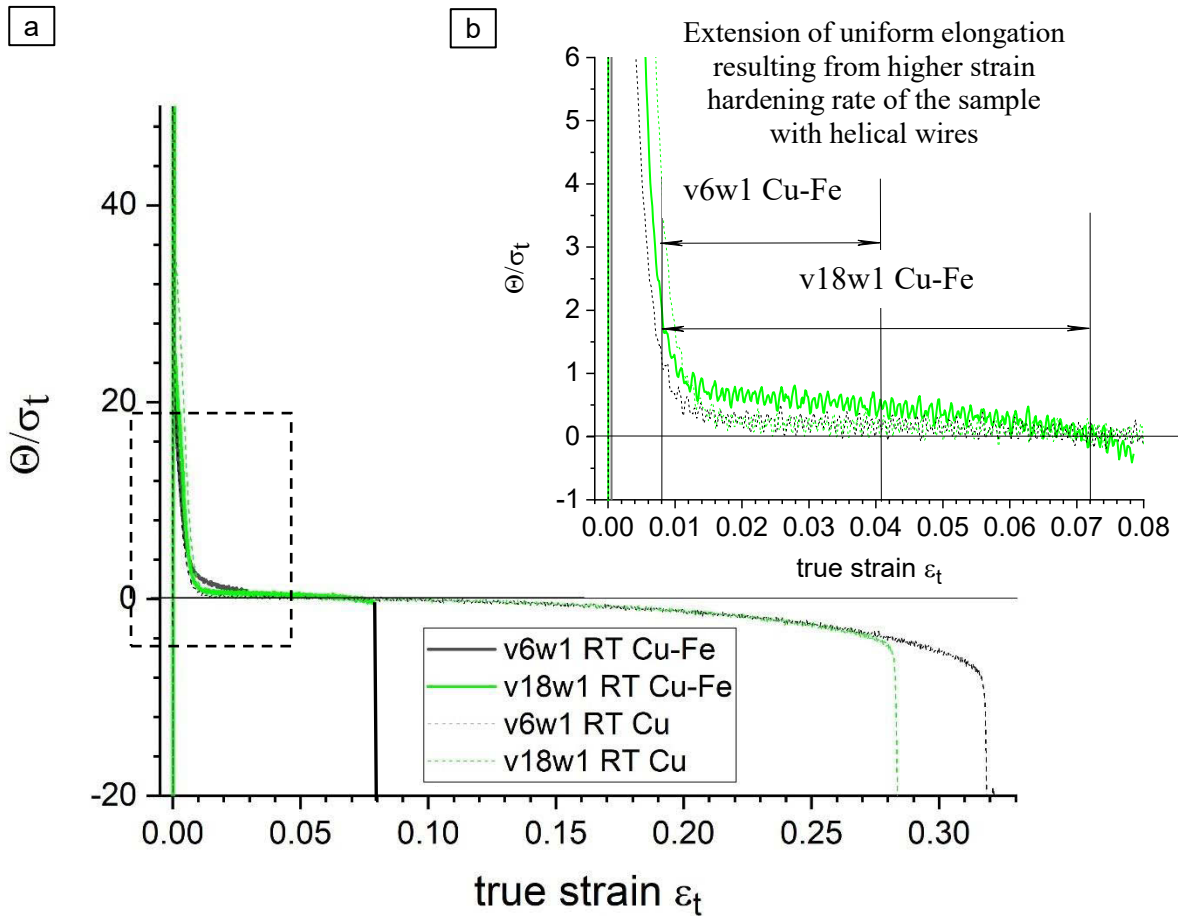


Figure 6.3 The normalized strain hardening rates, θ/σ_t , of the copper and Cu-Fe hybrid samples in the configuration (1) after the HPTE process, as function of the true strain.

As seen, up to a strain of 0.008, the highest hardening rate was observed in pure copper processed via the $v18\omega1$ regime. The hybrid sample after the $v6w1$ regime demonstrated a lesser SHR, and the hybrid sample after the $v18w1$ regime showed an even lesser one (Figure 6.3). With increasing tensile strain, the SHR rapidly falls almost down to zero in both copper samples and in the hybrid sample after the $v18w1$ regime.

After the $v18w1$ regime, slight twisting of the wires doesn't prevent rapid localization, as confirmed by the tensile test results. The work hardening rate drops to zero after the rupture of the first wire at a strain of $e \sim 0.072$ in the hybrid sample processed by the $v18w1$ regime, at the same point where it occurs in both pure copper samples after HPTE (the point is shown by the thick line in Figure 6.3). Therefore the $v18w1$ sample and both Cu samples exhibit essentially the same tensile behavior. As shown in Figure 6.3 b, after a strain of $e \sim 0.008$, the SHR of the hybrid sample processed by the $v6w1$ regime became the highest corresponding to the largest uniform elongation observed in this sample.

6.2.2. Analysis of helical reinforcements during the uniaxial extension process

For a detailed analysis of the reason for the increase in the uniform elongation stage in Cu-Fe specimens processed by the *v6w1* HPTE regime (Figure 6.2 b), a tensile test was interrupted at the uniform elongation stage after a strain of 3.1%. To assess the resulting change in the shape of the gauge and the strengthening elements (Figure 6.2 b), the sample was diametrically cut, and the corresponding images are presented in Figure 6.4 a, b. The diametrical cross-section of the hybrid sample was also analyzed after complete fracture. The rectangular cross-sectional shape indicates that the shape of the gauge of the sample remained cylindrical after deformation by 3.1 % (Figure 6.4 a). Additionally, Figure 6.4 a shows that the shape of the wires did not change significantly. After fracture, the gauge assumed a conical shape, and the wires were pulled in an axial direction (Figure 6.4 c).

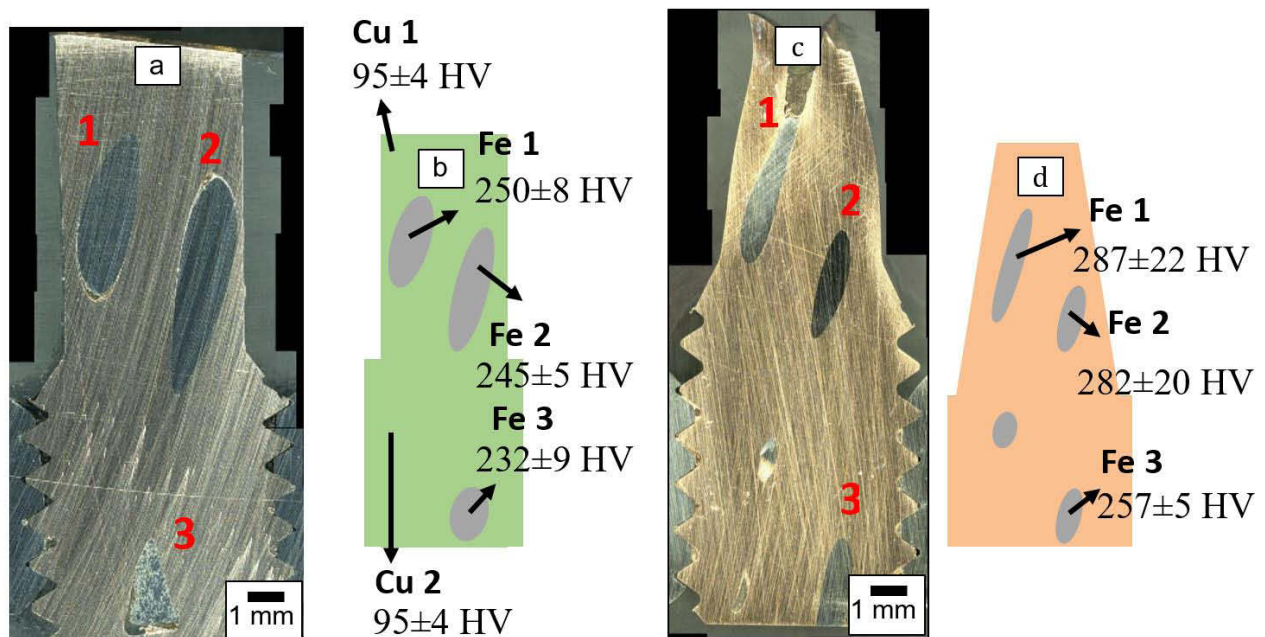


Figure 6.4 The image of the longitudinal section of the hybrid Cu-Fe sample in the configuration (1) processed by the *v6w1* regime, showing the state after 3.1% of extension (a, b) and after full rupture (c, d). The microhardness of iron wires in the area of holders and in the gauge was displayed on the scheme. The schemes (b, d) illustrated the shape of the longitudinal section of the hybrid sample, with the copper matrix marked by the green colour and the iron wires marked by the grey colour. The microhardness of the copper matrix was measured in the middle-radius region of the rod.

Microhardness measurements reveal that the hardness of the wires in the working part of the sample, stretched by 3.1%, increased by 5-7% from the original 230 HV (Figure 6.4 b). In the fractured sample, the hardness of the wires was approx. 290 HV, corresponding to a more significant hardening of approx. 15%. The hardness values obtained after tensile test were exceptionally high for pure iron. For example instance, as demonstrated by Edalati et al. [129], SPD of pure iron resulted in an increase in microhardness up to approx. 300 HV, which represented the maximum hardening of the material after SPD. As indicated by the tests with straight wires (Figure 6.2 b), the maximum elongation of straight wires in DE specimens before fracture was approx. 1%. Therefore, it can be assumed that during the uniaxial tension of the sample by 3.1%, the elongation of the wires themselves did not exceed 1%. Let us

consider the geometry of the shape change of the helical strengthening elements under the uniaxial tension of the hybrid specimens.

6.2.3. Geometrical consideration of the helical elements extension in the hybrid samples

The enhancement of the uniform elongation in the hybrid samples with embedded iron wires was obtained in samples processed via the *v6w1* regime and was not achieved after the *v18w1* regime. Furthermore, the improvement in uniform elongation was observed only for the strain range in which all three wires remained intact. After the rupture of the first wire, the tensile curve became parallel to that of the tensile curve of pure copper sample processed via the *v6w1* regime (Figure 6.2 b). The hybrid samples processed via the *v18w1* regime didn't show any improvement in uniform elongation. It appeared that the enhancement of the uniform elongation in the HPTE-processed hybrid material depends on the strength of the embedded material and the helix geometry.

The helical shape of the embedded wires, as demonstrated in Figure 5.10, can be defined by three parameters: its radius (R_f), the height at which the spiral makes a full rotation (R_l) and the lay (helix) angle (α) (Figure 6.5).

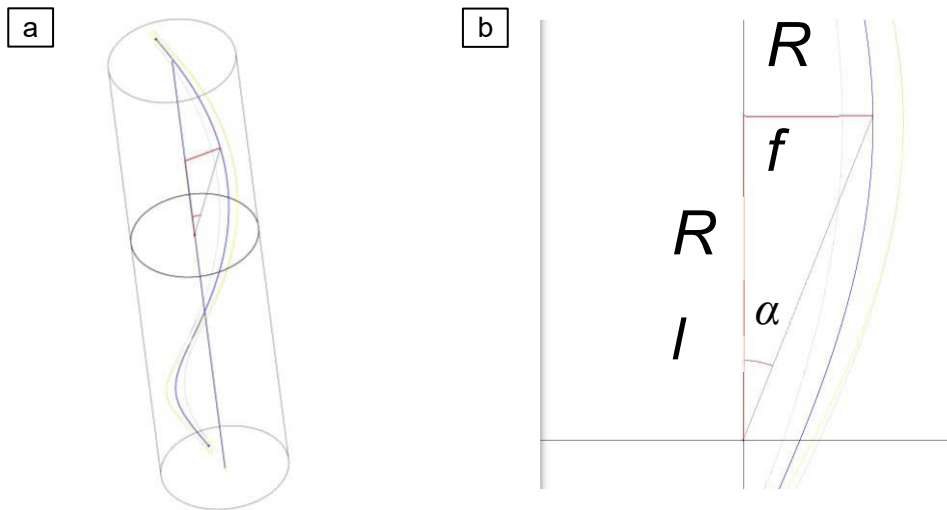


Figure 6.5 The geometry of the helical wire after twisting in 3D image (a) and a 2D longitudinal diametral section (b).

It is worth noting that the helical structure of fibers or wires in conventional ropes provides flexibility in bending, which increases with higher lay angles (α). However, as the lay angle increases, the load-carrying capacity of the rope decreases. The geometry parameters of the Fe wire helixes resulting from HPTE are summarized in Table 6.6.

Consider a wire helix with a total length (L) and a lay angle (α), which is purely in tension. The height (R_l) and the radius (R_f) (Figure 6.5 b) are related to α by the following relationship:

$$\operatorname{tg} \alpha = \frac{R_f}{R_l}, \quad (6.2)$$

The values of the lay angles of the helices (α) after the $v18w1$ and $v6w1$ regimes calculated via Equation (6.2), coincide with those measured directly from the longitudinal section obtained using X-ray tomography (Figure 5.10 a, b). Thus, the angle (α) and the value of (R_f) value characterize the helical geometry of the sample.

Table 6.6 The geometry parameters of the helical wires after HPTE.

state	N_H	R_f , mm	L , mm	α , °	R_f/R_l
initial	0	2.4	0	0	0
$v18w1$	1.0	2.4	15.1	3.9	1.0
$v6w1$	3.0	2.4	37.7	9.7	2.3

Considering the deformation of hybrid specimens hardened with helix wires of two configurations obtained by the HPTE $v6w1$ and $v18w1$ regimes, the helix length (L) is calculated based on the condition of joint deformation and the constancy of the sample volume during the uniaxial extension test, using the formula [130]:

$$L = 2\pi N \sqrt{R_f^2 + \left(\frac{l}{2\pi}\right)^2}, \quad (6.6)$$

where N is the number of helix loops, l is the length of the gauge.

Unlike a free spring, where the radius of the coils can change arbitrarily, in our case, the radius of the coils of the spiral will be determined by the condition of the constancy of the volume of the cylinder on the surface of which the spiral is located:

$$V = 2\pi N R_f^2 l \quad (6.7)$$

The height of the cylinder l is equal to the pitch of the coil H multiplied by the number of coils N .

$$L = 2\pi N \sqrt{\frac{V}{2\pi N H} - \left(\frac{H}{2\pi}\right)^2} = \sqrt{2\pi N \frac{V + N H^3}{H}} \quad (6.8)$$

Given the rigid fixation of the spiral in the gauge of the sample, the pitch of the coil (H) changes in direct proportion to the gauge elongation $H = H_0 * \frac{l}{l_0}$.

Equation (6.8) allowed the calculation of the length of the wire spirals in samples after the $v6w1$ and $v18w1$ regimes (Figure 6.6 a). The corresponding plot of the elongation of the wires versus gauge elongation is shown in Figure 6.6 b.

Figure 6.6 a demonstrates a close to linear dependence of the length of the helix, L , on the length of the sample gauge, l .

An increase in the gauge length per unit length led to a greater elongation of the wire helix in the samples obtained in the $v18w1$ regime than in samples obtained in the $v6w1$ regime. The greater strain of the helix after the $v18w1$ regime also resulted in a greater strain (Figure 6.6 b) due to the smaller initial length, L_0 , of the helix. According to the analytical

dependences obtained, under the condition of the same SHR of the iron wire, one could expect more effective hardening by wires precisely in the samples after the HPTE *v18w1* regime. However, the experiment showed that in the *v18w1* state, the hardening rate was lower than after the *v6w1* (Figure 6.3).

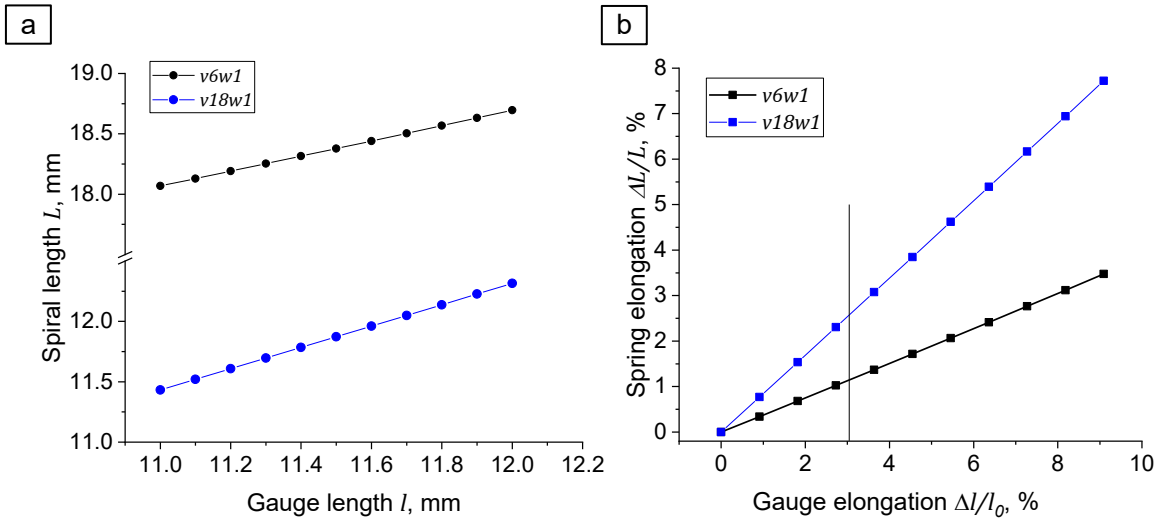


Figure 6.6 The diagram illustrated two relationships: (a) the length of the helices formed after HPTE plotted against the length of the gauge of the tensile sample, and (b) and the elongation of the helices plotted against the elongation of the gauge.

According to the analytical calculation (Equation (6.8)), stretching the gauge by 3% would lead to the elongation of the wire by approx. 1% (Figure 6.6 b), thus reaching the maximum elongation expected under uniaxial tension before fracture. However, fracture occurred later, after a strain of 3.9%, which may be attributed to a non-ideal joint deformation of the wire and matrix. For example, the wires could slip inside the copper matrix and stretch like springs without plastic deformation, resulting in a difference between the analytically calculated 3% (Figure 6.6 b) and the actual 3.9% (Table 6.5) elongation.

The observed increase in the uniform elongation stage of the hybrid sample after the *v6w1* HPTE regime was the result of a complex interaction between the soft matrix and the hard reinforcing elements. A preliminary investigation of this phenomenon led to many new questions. The main questions revolved around the nature of wire hardening in the matrix at the stage of uniform elongation of the sample, the role of the ratio of matrix and reinforcement element hardening, the possibility of slippage and the role of friction between reinforcement elements and the matrix, the influence of the twisted wire configuration on the interaction between the matrix and wires, and the influence of wire location relative to the surface of the gauge of the sample. A detailed study of this phenomenon is a separate major work, which is beyond the scope of the present study of the mechanical properties of hybrid SPD materials and will be the subject of further research.

7. Conclusions and Outlook

7.1 General discussion and conclusions

In this thesis, the high-pressure torsional extrusion (HPTE) scheme has been explored for its application in the severe plastic deformation of pure copper, copper-aluminum, and copper-iron hybrids. Throughout this research, gradient structures of pure copper, as well as copper-iron composites with helical architecture, have been designed, processed, and characterized. The processing regimes were carried out to investigate the impact of the HPTE processing on the resulting strain distribution along the radius of the cylinder-shaped samples. The main results and observations are summarized below:

A series of gradient coarse-grained to fine-grained (CG-FG) and fine-grained to ultrafine-grained (FG-UFG) bulk samples of pure copper and composite materials were successfully produced by HPTE. Both the microstructural analysis of pure copper and the tomography of the inserted aluminum wires showed that the use of elevated processing temperature allows a reduction of the pressing forces. However, it also leads to the elimination of sliding between the die and the processed sample.

Conclusions on Chapter 4

- The accumulated strain during HPTE results from both shear (twisting) and expansion-extrusion deformations. Additionally, significant shearing occurs due to friction, which is typical for the extrusion flow distortion, particularly in the periphery region of the billet. However, the primary contribution to the accumulated strain is attributed to the twisting of the billet within the HPTE die.
- Experimental observations of changes in the shape of the marker wires, coupled with Finite Element Method (FEM) calculations, have indicated the presence of significant slippage between the walls of the HPTE die and the billet. This slippage is more pronounced in billets deformed at 100°C compared to those deformed at 25°C.
- HPTE enabled the attainment of notably high strain values during a single pass. For instance, in copper billets processed via the $\nu 6\omega 1$ regime at 25°C, the strain values varied from 1.5 at the billet center to 12 at its periphery. These values were considerably higher than the strain achieved after a single Equal Channel Angular Pressing (ECAP) pass or a single twist extrusion pass.

Microstructure investigations of the pure copper samples processed by HPTE at 100°C demonstrated the potential formation of a gradient structure (either CG-FG or CG/FG-UFG) in the bulk rods of this commercially significant structural material. The efficiency of HPTE methods for producing helical-architected samples is noteworthy. The capability to twist input wires within a copper matrix without inducing cracks, along with the optimal fit of the matrix to the reinforcement elements, distinguishes it significantly from prior experimental methods involving the formation of corrugated wires [35].

In the case of pure copper processed by HPTE at room temperature, as reported in [12], grain refinement was more pronounced than that achieved by HPTE at 100°C in the present study. Consequently, a further increase in the deformation temperature might reduce the efficiency of HPTE as a Severe Plastic Deformation (SPD) method. Conversely, lower temperatures may result in reduced slippage between the specimen and the die surface, thereby enhancing the efficiency of HPTE for grain refinement. In this scenario, the lowest deformation temperature for HPTE is constrained by the plasticity of the working material.

Conclusions on Chapter 5

- HPTE processing of copper deformed at 100°C using the *v10w0*, *v10w1* and *v1w1* regimes results in the formation of a gradient structure. The region near the billet axis exhibits a fine-grained microstructure, while the remaining portion of the billet displays an ultrafine-grained microstructure.
- HPTE processing of copper at 100°C leads to significant grain refinement. The initial annealed microstructure, with a grain size around 30 μm, transforms into an ultrafine-grained structure with a saturated final grain size of approx. 0.7 μm.
- The HPTE process facilitates the formation of helical geometries for reinforcing wires in Cu-Al and Cu-Fe hybrid samples. The number of loops in the helices can be controlled by the specific HPTE regime employed.

The potential for producing bulk UFG samples through HPTE enables the testing of their mechanical strength. Tensile tests conducted on HPTE-processed samples demonstrate a significant strengthening of pure copper samples. The specific volume of the UFG, FG, and CG structures in the samples contributes to the corresponding strength of the overall material.

Copper-iron bulk samples, produced through HPTE with various helical architectures, were subjected to uniaxial tension testing at room temperature. One of the tested configurations illustrates the extension stage of uniform elongation in the SPD-processed material. The mechanism involving the interaction between the matrix and reinforcement elements is then considered.

Conclusions on Chapter 6

- The mechanical properties and tensile behavior of pure copper, following HPTE with a gradient structure, were observed to be similar to those exhibited by pure copper after other SPD techniques that yield a homogeneous structure.
- The strength of the gradient HPTE copper sample was found to follow the rule of mixture. It was observed that the primary contribution to the strength of copper processed by HPTE at 100 °C is the grain boundary strengthening via the Hall–Petch mechanism. Low-angle boundaries and nanotwins act as effective barriers to dislocation slip, and their

influence should be considered when applying the grain size aspect in the Hall–Petch equation.

- The combination of a copper matrix with a helical architecture of aluminum wires, characterized by a hard matrix and soft wires, did not influence the tensile behavior of the hybrid samples. However, in the case of copper-iron hybrid samples, a slight strengthening was observed.
- Tensile tests were conducted on the HPTE-processed copper/iron hybrid samples, demonstrating the potential to extend the stage of uniform elongation.

7.2 Outlook and future investigations

The experimental validation of the results calculated by FEM allows us to understand the actual limitations of the HPTE method for industrial applications. This method can be employed for the production of SPD-processed bulk materials by combining HPTE with high-productivity industrial conventional methods, such as rolling, direct extrusion, and ECAP-conform. The limitation of the deformation temperature for many structural conventional metals and alloys is determined by the slipping of the workpiece in the HPTE die, resulting in a decrease in processing efficiency. The material of the embedded element should match the strength and plasticity of the matrix closely. In such cases, deformation by HPTE can achieve levels of deformation that cannot be realized by conventional deformation methods. Despite existing limitations in additional deformation realized using HPTE, it is possible to implement "soft" regimes, such as $v_{10}w_1$, for the formation of a gradient CG-FG structure, as demonstrated in this work for pure copper.

Simultaneously, structural investigations of the hybrid samples have revealed opportunities for creating hybrid materials with a helical architecture suitable for both structural and functional applications. The production of hybrid samples should be carried out using a high-plasticity matrix at low deformation temperatures to ensure the high efficiency of deformation. This approach enhances the effectiveness of HPTE, facilitating significant grain refinement and strengthening for both the matrix material and the reinforcement elements. Moreover, HPTE processing can be integrated with deformation and temperature treatments to systematically alter the structure and properties of the matrix and the reinforcement elements.

HPTE regimes employing high strains, such as the v_1w_1 regime, result in a substantial reduction in the thickness of embedded wires by more than 100 times. The initial wires, characterized by a circular cross-section, transform into thin ribbons after undergoing this deformation process. Consequently, HPTE emerges as a viable method for synthesizing multilayers within bulk samples.

Hybrid configurations featuring numerous thin wires can be effectively processed using HPTE, yielding architected samples with ribbons measuring approx. 100 nm or less in thickness. The final ribbon thickness depends on the initial geometry of the embedded elements and the specific HPTE regimes employed. In these multilayers, effects commonly observed in thin nano- and micro-layers can be realized within bulk samples. In this context,

the HPTE process presents itself as a potential means for upscaling techniques used in thin-layer technologies, as implemented by various layer deposition processes on substrates.

The potential for enhanced plasticity, particularly an extended uniform elongation, in highly strengthened SPD structural materials holds critical significance for the development and industrial application of such materials. As reported in various publications [5, 130-132], an enhancement in strain hardening capacity contributes to extending the uniform elongation of SPD-processed materials.

As highlighted in the introduction, a significant challenge faced by SPD-processed metals and alloys is the notable decrease in low-cycle fatigue strength σ_{LCF} and shortened fatigue life N_f of UFG metals and alloys, as documented in [16, 17]. The extended uniform elongation stage can potentially improve the low-cycle fatigue properties of HPTE-processed hybrid samples. Consequently, combining the advantages of the SPD-treated matrix (enhanced strength) with an increase in its ductility should enhance the overall complex of mechanical properties, rendering them more attractive for commercial applications.

Hence, one promising avenue for investigation involves the design and processing of hybrids with helical architectures using HPTE to develop advantageous mechanical properties.

References

- [1] H. Gleiter, "Nanocrystalline materials". *Progress in Materials Science*, vol. 33, pp. 223-315, 1989.
- [2] O. A. Kaibyshev, in *Superplasticity of alloys, intermetallides and ceramics*, (Ed: O. A. Kaibyshev), Springer, Berlin, Heidelberg 1992, 92-116.
- [3] R. W. Siegel, "Nanostructured materials -mind over matter". *Nanostructured Materials*, vol. 4, pp. 121-138, 1994.
- [4] R. Z. Valiev, R. K. Islamgaliev and I. V. Alexandrov, "Bulk nanostructured materials from severe plastic deformation". *Progress in Materials Science*, vol. 45, pp. 103-189, 2000.
- [5] R. Valiev, "Nanostructuring of metals by severe plastic deformation for advanced properties". *Nature Materials*, vol. 3, pp. 511-516, 2004.
- [6] V. M. Segal, V. I. Reznikov, F. E. Drobishevski and V.I.Kopilov, "Deformation processing of metals by a simple shearing". *Izvestia academy of sciences of the USSR: Metals*, vol. 1, pp. 115, 1981.
- [7] Y. Estrin and A. Vinogradov, "Extreme grain refinement by severe plastic deformation: A wealth of challenging science". *Acta Materialia*, vol. 61, pp. 782-817, 2013.
- [8] P. W. Bridgman, "On torsion combined with compression". *Journal of Applied Physics*, vol. 14, pp. 273-283, 1943.
- [9] Y. Saito, H. Utsunomiya, N. Tsuji and T. Sakai, "Novel ultra-high straining process for bulk materials—development of the accumulative roll-bonding (ARB) process". *Acta Materialia*, vol. 47, pp. 579-583, 1999.
- [10] Y. Beygelzimer, R. Kulagin, Y. Estrin, L. S. Toth, H. S. Kim and M. I. Latypov, "Twist extrusion as a potent tool for obtaining advanced engineering materials: a review". *Advanced Engineering Materials*, vol. 19, pp. 1600873, 2017.
- [11] S. V. Zherebtsov, G. A. Salishchev, R. M. Galeev, O. R. Valiakhmetov, S. Y. Mironov and S. L. Semiatin, "Production of submicrocrystalline structure in large-scale Ti–6Al–4V billet by warm severe deformation processing". *Scripta Materialia*, vol. 51, pp. 1147-1151, 2004.
- [12] Y. Ivanisenko, R. Kulagin, V. Fedorov, A. Mazilkin, T. Scherer, B. Baretzky and H. Hahn, "High pressure torsion extrusion as a new severe plastic deformation process". *Materials Science and Engineering: A*, vol. 664, pp. 247-256, 2016.
- [13] V. Fedorov, J. Ivanisenko, B. Baretzky and H. Hahn, "Vorrichtung und Verfahren zur Umformung von Bauteilen aus Metallwerkstoffen". *DE Patent DE102013213072A1*, vol. 8, 2015.
- [14] S. R. Agnew, A. Y. Vinogradov, S. Hashimoto and J. R. Weertman, "Overview of fatigue performance of Cu processed by severe plastic deformation". *Journal of Electronic Materials*, vol. 28, pp. 1038-1044, 1999.
- [15] I. P. Semenova, E. B. Yakushina, V. V. Nurgaleeva and R. Z. Valiev, "Nanostructuring of Ti-alloys by SPD processing to achieve superior fatigue properties". *International Journal of Materials Research*, vol. 100, pp. 1691-1696, 2009.
- [16] A. Vinogradov and S. Hashimoto, "Fatigue of severely deformed metals". *Advanced Engineering Materials*, vol. 5, pp. 351-358, 2003.
- [17] H. Mughrabi and H. W. Höppel, "Cyclic deformation and fatigue properties of very fine-grained metals and alloys". *International Journal of Fatigue*, vol. 32, pp. 1413-1427, 2010.
- [18] X. W. Li, Q. W. Jiang, Y. Wu, Y. Wang and Y. Umakoshi, "Stress-amplitude-dependent deformation characteristics and microstructures of cyclically stressed ultrafine-grained copper". *Advanced Engineering Materials*, vol. 10, pp. 720-726, 2008.

-
- [19] Y. S. Li, Y. Zhang, N. R. Tao and K. Lu, "Effect of thermal annealing on mechanical properties of a nanostructured copper prepared by means of dynamic plastic deformation". *Scripta Materialia*, vol. 59, pp. 475-478, 2008.
- [20] M. Korn, R. Lapovok, A. Böhner, H. W. Höppel and H. Mughrabi, "Bimodal grain size distributions in UFG materials produced by SPD-their evolution and effect on the fatigue and monotonic strength properties". *Kovove Mater*, vol. 49, pp. e63, 2011.
- [21] T. Fang, W. Li, N. Tao and K. Lu, "Revealing extraordinary intrinsic tensile plasticity in gradient nano-grained copper". *Science*, vol. 331, pp. 1587-1590, 2011.
- [22] O. Bouaziz, "Geometrically induced strain hardening". *Scripta Materialia*, vol. 68, pp. 28-30, 2013.
- [23] D. Raabe, P.-P. Choi, Y. Li, A. Kostka, X. Sauvage, F. Lecouturier, K. Hono, R. Kirchheim, R. Pippan and D. Embury, "Metallic composites processed via extreme deformation: toward the limits of strength in bulk materials". *MRS Bulletin*, vol. 35, pp. 982-991, 2010.
- [24] A. Bachmaier and R. Pippan*, "Generation of metallic nanocomposites by severe plastic deformation". *International Materials Reviews*, vol. 58, pp. 41-62, 2013.
- [25] M. F. Ashby and Y. J. M. Bréchet, "Designing hybrid materials". *Acta Materialia*, vol. 51, pp. 5801-5821, 2003.
- [26] O. Bouaziz, H. S. Kim and Y. Estrin, "Architecturing of metal-based composites with concurrent nanostructuring: a new paradigm of materials design". *Advanced Engineering Materials*, vol. 15, pp. 336-340, 2013.
- [27] R. Z. Valiev, I. V. Alexandrov, Y. T. Zhu and T. C. Lowe, "Paradox of strength and ductility in metals processed by severe plastic deformation". *Journal of Materials Research*, vol. 17, pp. 5-8, 2002.
- [28] M. Y. Alawadhi, S. Sabbaghianrad, Y. Huang and T. G. Langdon, "Direct influence of recovery behaviour on mechanical properties in oxygen-free copper processed using different SPD techniques: HPT and ECAP". *Journal of Materials Research and Technology*, vol. 6, pp. 369-377, 2017.
- [29] R. Matsutani, N. Nakada and S. Onaka, "Increase in total elongation caused by pure shear deformation in ultra-fine-grained Cu processed by equal-channel angular pressing". *Metals*, vol. 10, 2020.
- [30] M. Furukawa, Z. Horita, M. Nemoto and T. G. Langdon, "Review: processing of metals by equal-channel angular pressing". *Journal of Materials Science*, vol. 36, pp. 2835-2843, 2001.
- [31] V. Segal, "Review: modes and processes of severe plastic deformation (SPD)". *Materials*, vol. 11, 2018.
- [32] A. Zhilyaev, G. Nurislamova, B.-K. Kim, M. Baró, J. Szpunar and T. Langdon, "Experimental parameters influencing grain refinement and microstructural evolution during high-pressure torsion". *Acta Materialia*, vol. 51, pp. 753-765, 2003.
- [33] Q. Pan and L. Lu, "Improved fatigue resistance of gradient nanograined metallic materials: Suppress strain localization and damage accumulation". *Scripta Materialia*, vol. 187, pp. 301-306, 2020.
- [34] R. Matsutani, Y. Miyajima and S. Onaka, "Refinement and coarsening of grains caused by tensile-shear tests in ultra-fine grained Cu processed by severe plastic deformation". *Materials Transactions*, vol. 60, pp. 751-757, 2029.
- [35] Y. Estrin, Y. Bréchet, J. Dunlop and P. Fratzl, "Architected materials in nature and engineering". *Cham, Switzerland: Springer Nature Switzerland AG*, 2019.
- [36] H. Wargnier, F. X. Kromm, M. Danis and Y. Brechet, "Proposal for a multi-material design procedure". *Materials & Design (1980-2015)*, vol. 56, pp. 44-49, 2014.

- [37] S. Gasser, Y. Brechet and F. Paun, "Materials design for acoustic liners: an example of tailored multifunctional materials". *Advanced Engineering Materials*, vol. 6, pp. 97-102, 2004.
- [38] L. Li, J. C. Weaver and C. Ortiz, "Hierarchical structural design for fracture resistance in the shell of the pteropod *Clio pyramidata*". *Nature Communications*, vol. 6, pp. 6216, 2015.
- [39] J. D. Currey, *Bones: structure and mechanics*, Princeton university press, 2006.
- [40] K. Lu and J. Lu, "Nanostructured surface layer on metallic materials induced by surface mechanical attrition treatment". *Materials Science and Engineering: A*, vol. 375-377, pp. 38-45, 2004.
- [41] Y. Beygelzimer, R. Kulagin and Y. Estrin, in *Architected materials in nature and engineering: archimats*, (Eds: Y. Estrin, Y. Bréchet, J. Dunlop and P. Fratzl), Springer International Publishing, Cham 2019, 231-255.
- [42] Y. Qi, R. Lapovok and Y. Estrin, "Microstructure and electrical conductivity of aluminium/steel bimetallic rods processed by severe plastic deformation". *Journal of Materials Science*, vol. 51, pp. 6860-6875, 2016.
- [43] O. Prokof'eva, Y. Beygelzimer, V. V. Usov, N. Shkatulyak, T. S. Sovkova, A. Sapronov, D. Prilepo and V. Varyukhin, "Formation of a gradient structure in a material by twist extrusion". *Russian Metallurgy (Metally)*, vol. 2020, pp. 573-578, 2020.
- [44] Y. Beygelzimer, Y. Estrin and R. Kulagin, "Synthesis of hybrid materials by severe plastic deformation: a new paradigm of SPD processing". *Advanced Engineering Materials*, vol. 17, pp. 1853-1861, 2015.
- [45] C. Chen, Y. Beygelzimer, L. S. Toth, Y. Estrin and R. Kulagin, "Tensile yield strength of a material preprocessed by simple shear". *Journal of Engineering Materials and Technology-Transactions of the Asme*, vol. 138, pp. 4, 2016.
- [46] L. Li, J. C. Weaver and C. Ortiz, "Hierarchical structural design for fracture resistance in the shell of the pteropod *Clio pyramidata*". *Nature Communications*, vol. 6, pp. 1-10, 2015.
- [47] E. W. Hart, "Theory of the tensile test". *Acta Metallurgica*, vol. 15, pp. 351-355, 1967.
- [48] G. E. Dieter, Ed. *Mechanical metallurgy*, McGraw-Hill Book Company (UK) Limited, London 1988.
- [49] S. Khoddam, Y. Estrin, H. S. Kim and O. Bouaziz, "Torsional and compressive behaviours of a hybrid material: Spiral fibre reinforced metal matrix composite". *Materials & Design*, vol. 85, pp. 404-411, 2015.
- [50] K. Edalati, T. Fujioka and Z. Horita, "Microstructure and mechanical properties of pure Cu processed by high-pressure torsion". *Materials Science and Engineering: A*, vol. 497, pp. 168-173, 2008.
- [51] Y. Wang, M. Chen, F. Zhou and E. Ma, "High tensile ductility in a nanostructured metal". *Nature*, vol. 419, pp. 912, 2002.
- [52] Y. M. Wang and E. Ma, "Strain hardening, strain rate sensitivity, and ductility of nanostructured metals". *Materials Science and Engineering: A*, vol. 375-377, pp. 46-52, 2004.
- [53] R. Pippan, S. Scheriau, A. Taylor, M. Hafok, A. Hohenwarter and A. Bachmaier, "Saturation of fragmentation during severe plastic deformation". *Annual Review of Materials Research*, vol. 40, pp. 319-343, 2010.
- [54] N. Lugo, N. Llorca, J. M. Cabrera and Z. Horita, "Microstructures and mechanical properties of pure copper deformed severely by equal-channel angular pressing and high pressure torsion". *Materials Science and Engineering: A*, vol. 477, pp. 366-371, 2008.
- [55] F. Dalla Torre, R. Lapovok, J. Sandlin, P. F. Thomson, C. H. J. Davies and E. V. Pereloma, "Microstructures and properties of copper processed by equal channel angular extrusion for 1–16 passes". *Acta Materialia*, vol. 52, pp. 4819-4832, 2004.
- [56] R. Kocich, J. Fiala, I. Szurman, A. Macháčková and M. Mihola, "Twist-channel angular pressing: effect of the strain path on grain refinement and mechanical properties of copper". *Journal of Materials Science*, vol. 46, pp. 7865-7876, 2011.

- [57] Z. Horita, T. G. Langdon, "Microstructures and microhardness of an aluminum alloy and pure copper after processing by high-pressure torsion". *Materials Science and Engineering: A*, vol. 410–411, pp. 422-425, 2005.
- [58] S. Sabbaghianrad and T. G. Langdon, "An evaluation of the saturation hardness in an ultrafine-grained aluminum 7075 alloy processed using different techniques". *Journal of Materials Science*, vol. 50, pp. 4357-4365, 2015.
- [59] A. Vorhauer and R. Pippan, "On the onset of a steady state in body-centered cubic iron during severe plastic deformation at low homologous temperatures". *Metallurgical and Materials Transactions A*, vol. 39, pp. 417-429, 2008.
- [60] R. Pippan, S. Scheriau, A. Hohenwarter and M. Hafok, "Advantages and limitations of HPT: a review". *Materials Science Forum*, vol. 584-586, pp. 16-21, 2008.
- [61] C. Zener and J. H. Hollomon, "Effect of strain rate upon plastic flow of steel". *Journal of Applied Physics*, vol. 15, pp. 22-32, 1944.
- [62] Y. Wang, M. Chen, F. Zhou and E. Ma, "High tensile ductility in a nanostructured metal". *Nature*, vol. 419, pp. 912-915, 2002.
- [63] J. Čížek, M. Janeček, T. Krajňák, J. Stráská, P. Hruška, J. Gubicza and H. S. Kim, "Structural characterization of ultrafine-grained interstitial-free steel prepared by severe plastic deformation". *Acta Materialia*, vol. 105, pp. 258-272, 2016.
- [64] N. Kumar and R. S. Mishra, "Additivity of strengthening mechanisms in ultrafine grained Al–Mg–Sc alloy". *Materials Science and Engineering: A*, vol. 580, pp. 175-183, 2013.
- [65] G. I. Taylor, "The mechanism of plastic deformation of crystals. Part I.—Theoretical". *Proceedings of the Royal Society of London. Series A, Containing Papers of a Mathematical and Physical Character*, vol. 145, pp. 362-387, 1934.
- [66] E. O. Hall, "The deformation and ageing of mild steel: III discussion of results". *Proceedings of the Physical Society. Section B*, vol. 64, pp. 747-753, 1951.
- [67] H. Fujita, K. Toyoda, T. Mori, T. Tabata, T. Ono and T. Takeda, "Dislocation behavior in the vicinity of grain boundaries in FCC metals and alloys". *Transactions of the Japan Institute of Metals*, vol. 24, pp. 195-204, 1983.
- [68] A. W. Thompson, "Substructure strengthening mechanisms". *Metallurgical Transactions A*, vol. 8, pp. 833-842, 1977.
- [69] J. Gil Sevillano, P. van Houtte and E. Aernoudt, "Large strain work hardening and textures". *Progress in Materials Science*, vol. 25, pp. 69-134, 1980.
- [70] M. A. Stremel, "Prochnost splavov", Vol. 2, MISIS, 1997.
- [71] P. Kratochvíl and E. Neradová, "Solid solution hardening in some copper base alloys". *Czechoslovak Journal of Physics B*, vol. 21, pp. 1273-1278, 1971.
- [72] K. J. S. Orowan E. , F. Seitz, and S. J. W. Read, "Dislocations in metals", AIME, New York 1954.
- [73] U. F. Kocks, "A statistical theory of flow stress and work-hardening". *The Philosophical Magazine: A Journal of Theoretical Experimental and Applied Physics*, vol. 13, pp. 541-566, 1966.
- [74] P. B. H. a. F. J. Humphreys, in *Physics of Strength and Plasticity*, Vol. 404 (Ed: A. S. Argon), M.I.T. Press, Cambridge, Mass 1969, 404.
- [75] B. Omranpour, R. Kulagin, Y. Ivanisenko and E. Garcia Sanchez. "Experimental and numerical analysis of HPTE on mechanical properties of materials and strain distribution", *IOP Conference Series: Materials Science and Engineering*, vol. 194, 012047.
- [76] R. Kulagin, Y. Beygelzimer, Y. Estrin, Y. Ivanisenko, B. Baretzky and H. Hahn, "A Mathematical Model of Deformation under High Pressure Torsion Extrusion". *Metals*, vol. 9, 2019.

- [77] X. Ma, M. R. Barnett and Y. H. Kim, "Forward extrusion through steadily rotating conical dies. Part I: experiments". *International Journal of Mechanical Sciences*, vol. 46, pp. 449-464, 2004.
- [78] C. Etherington, "Conform—a new concept for the continuous extrusion forming of metals". *Journal of Engineering for Industry*, vol. 96, pp. 893-900, 1974.
- [79] J. Hu, R. Kulagin, Y. Ivanisenko, B. Baretzky and H. Zhang, "Finite element modeling of Conform-HPTE process for a continuous severe plastic deformation path". *Journal of Manufacturing Processes*, vol. 55, pp. 373-380, 2020.
- [80] B. Omranpour, Y. Ivanisenko, R. Kulagin, L. Kommel, E. Garcia Sanchez, D. Nugmanov, T. Scherer, A. Heczal and J. Gubicza, "Evolution of microstructure and hardness in aluminum processed by High Pressure Torsion Extrusion". *Materials Science and Engineering: A*, pp. 138074, 2019.
- [81] Y. Cao, L. He, Y. Zhou, P. Wang and J. Cui, "Contributions to yield strength in an ultrafine grained 1050 aluminum alloy after DC current annealing". *Materials Science and Engineering: A*, vol. 674, pp. 193-202, 2016.
- [82] E. A. El-Danaf, M. S. Soliman, A. A. Almajid and M. M. El-Rayes, "Enhancement of mechanical properties and grain size refinement of commercial purity aluminum 1050 processed by ECAP". *Materials Science and Engineering: A*, vol. 458, pp. 226-234, 2007.
- [83] M. Naderi, M. Peterlechner, S. V. Divinski and G. Wilde, "The effect of pre-annealing on defects, microstructure and recrystallization of ultra-fine grained Al produced by high-pressure torsion". *Materials Science and Engineering: A*, vol. 708, pp. 171-180, 2017.
- [84] A. Hohenwarter, "Incremental high pressure torsion as a novel severe plastic deformation process: Processing features and application to copper". *Materials Science and Engineering: A*, vol. 626, pp. 80-85, 2015.
- [85] N. Pardis, B. Talebanpour, R. Ebrahimi, S. Zomorodian, "Cyclic expansion-extrusion (CEE): A modified counterpart of cyclic extrusion-compression (CEC)", *Materials Science and Engineering: A*, vol 528, pp. 7537-7540, 2011,
- [86] E. Schafler, "Effects of releasing the hydrostatic pressure on the nanostructure after severe plastic deformation of Cu". *Scripta Materialia*, vol. 62, pp. 423-426, 2010.
- [87] K. Edalati, D. J. Lee, T. Nagaoka, M. Arita, H. S. Kim, Z. Horita and R. Pippan, "Real hydrostatic pressure in high-pressure torsion measured by bismuth phase transformations and FEM simulations". *Materials Transactions*, vol. 57, pp. 533-538, 2016.
- [88] T. Hausöl, V. Maier, C. W. Schmidt, M. Winkler, H. W. Höppel and M. Göken, "Tailoring materials properties by accumulative roll bonding". *Advanced Engineering Materials*, vol. 12, pp. 740-746, 2010.
- [89] T. Hausöl, H. W. Höppel and M. Göken, "Tailoring materials properties of UFG aluminium alloys by accumulative roll bonded sandwich-like sheets". *Journal of Materials Science*, vol. 45, pp. 4733-4738, 2010.
- [90] S. Amirkhanlou, M. Ketabchi, N. Parvin, S. Khorsand and R. Bahrami, "Accumulative press bonding; a novel manufacturing process of nanostructured metal matrix composites". *Materials & Design*, vol. 51, pp. 367-374, 2013.
- [91] J. R. Davis and A. S. M. I. H. Committee, *Copper and copper alloys*, ASM International, 2001.
- [92] J. G. Kaufman, *Introduction to aluminum alloys and tempers*, ASM international, 2000.
- [93] G. E. Dieter, H. A. Kuhn and S. L. Semiatin, *Handbook of workability and process design*, ASM international, 2003.
- [94] M. Gholami, A. Rashedi, N. Lenoir, D. Hautemayou, G. Ovarlez and S. Hormozi, "Time-resolved 2D concentration maps in flowing suspensions using X-ray". *Journal of Rheology*, vol. 62, pp. 955-974, 2018.

- [95] F. J. Humphreys, "Review grain and subgrain characterisation by electron backscatter diffraction". *Journal of Materials Science*, vol. 36, pp. 3833-3854, 2001.
- [96] A. P. Day, P. Trimby, K. Mehnert and B. Neumann, "Channel 5 user manual". *HKL Technology A/S, Hobro, Denmark*, 2001.
- [97] S. I. Wright, D. P. Field and D. J. Dingley, in *Electron Backscatter Diffraction in Materials Science*, (Eds: A. J. Schwartz, M. Kumar and B. L. Adams), Springer US, Boston, MA 2000, 141-152.
- [98] A. Kobler and C. Kübel, "Challenges in quantitative crystallographic characterization of 3D thin films by ACOM-TEM". *Ultramicroscopy*, vol. 173, pp. 84-94, 2017.
- [99] C. S. Own, L. D. Marks and W. Sinkler, "Electron precession: A guide for implementation". *Review of Scientific Instruments*, vol. 76, pp. 033703, 2005.
- [100] R. Vincent and P. A. Midgley, "Double conical beam-rocking system for measurement of integrated electron diffraction intensities". *Ultramicroscopy*, vol. 53, pp. 271-282, 1994.
- [101] C. Own, "System design and verification of the precession electron diffraction technique". *Department of Materials Science and Engineering, Northwestern, Evanston*, vol. 161, 2005.
- [102] B. S. El-Dasher, B. L. Adams and A. D. Rollett, "Viewpoint: experimental recovery of geometrically necessary dislocation density in polycrystals". *Scripta Materialia*, vol. 48, pp. 141-145, 2003.
- [103] D. P. Field, P. B. Trivedi, S. I. Wright and M. Kumar, "Analysis of local orientation gradients in deformed single crystals". *Ultramicroscopy*, vol. 103, pp. 33-39, 2005.
- [104] A. Kundu and D. P. Field, "Geometrically necessary dislocation density evolution in interstitial free steel at small plastic strains". *Metallurgical and Materials Transactions A*, vol. 49, pp. 3274-3282, 2018.
- [105] H. Gao, Y. Huang, W. D. Nix and J. W. Hutchinson, "Mechanism-based strain gradient plasticity— I. Theory". *Journal of the Mechanics and Physics of Solids*, vol. 47, pp. 1239-1263, 1999.
- [106] M. Calcagnotto, D. Ponge, E. Demir and D. Raabe, "Orientation gradients and geometrically necessary dislocations in ultrafine grained dual-phase steels studied by 2D and 3D EBSD". *Materials Science and Engineering A - Structural Materials Properties Microstructure and Processing*, vol. 527, pp. 2738-2746, 2010.
- [107] F. J. Humphreys, Y. Huang, I. Brough and C. Harris, "Electron backscatter diffraction of grain and subgrain structures — resolution considerations". *Journal of Microscopy*, vol. 195, pp. 212-216, 1999.
- [108] F. J. Humphreys, "Characterisation of fine-scale microstructures by electron backscatter diffraction (EBSD)". *Scripta Materialia*, vol. 51, pp. 771-776, 2004.
- [109] P. Oleynikov, S. Hovmöller and X. D. Zou, "Precession electron diffraction: Observed and calculated intensities". *Ultramicroscopy*, vol. 107, pp. 523-533, 2007.
- [110] E. F. Rauch, J. Portillo, S. Nicolopoulos, D. Bultreys, S. Rouvimov and P. Moeck, "Automated nanocrystal orientation and phase mapping in the transmission electron microscope on the basis of precession electron diffraction". *Zeitschrift für Kristallographie*, vol. 225, pp. 103-109, 2010.
- [111] E. F. Rauch and M. Véron, "Automated crystal orientation and phase mapping in TEM". *Materials Characterization*, vol. 98, pp. 1-9, 2014.
- [112] B. Beausir, J.-J. Fundenberger, Université de Lorraine - Metz, ATEX[®] - analysis tools for electron and X-ray diffraction, <http://ATEX-software.eu/>, 2015.
- [113] J. Markmann, V. Yamakov and J. Weissmüller, "Validating grain size analysis from X-ray line broadening: A virtual experiment". *Scripta Materialia*, vol. 59, pp. 15-18, 2008.
- [114] G. K. Williamson and R. E. Smallman, "III. Dislocation densities in some annealed and cold-worked metals from measurements on the X-ray debye-scherrer spectrum". *The*

- Philosophical Magazine: A Journal of Theoretical Experimental and Applied Physics*, vol. 1, pp. 34-46, 1956.
- [115] R. E. Smallman and K. H. Westmacott, "Stacking faults in face-centred cubic metals and alloys". *The Philosophical Magazine: A Journal of Theoretical Experimental and Applied Physics*, vol. 2, pp. 669-683, 1957.
- [116] H. P. Klug and L. E. Alexander, *X-ray diffraction procedures: for polycrystalline and amorphous materials*, 1974.
- [117] N. Biba, A. Maximov, S. Stebunov and A. Vlasov, in *Proceedings of the 14th international conference on metal forming, Krakow, Poland, (2012)*, Vol., p. pp. 1363-1366.
- [118] A. N. Levanov, "Improvement of metal forming processes by means of useful effects of plastic friction". *Journal of Materials Processing Technology*, vol. 72, pp. 314-316, 1997.
- [119] C. Geuzaine and J.-F. Remacle, "Gmsh: A 3-D finite element mesh generator with built-in pre- and post-processing facilities". *International Journal for Numerical Methods in Engineering*, vol. 79, pp. 1309-1331, 2009.
- [120] D. Gerasimov, N. Biba, S. Stebunov and M. V. Kadach, "Implementation of a dual mesh method for longitudinal rolling in QForm V8". *Materials Science Forum*, vol. 854, pp. 158-162, 2016.
- [121] D. M. Rabkin, Ryabov, V.R., Lozovskaya, A.V. , "Preparation and properties of copper-aluminum intermetallic compounds". *Powder Metall Met Ceram*, vol. 9, pp. 695, 1970.
- [122] F. Samadpour, G. Faraji, P. Babaie, S.R. Bewsher, M. Mohammadpour, "Hydrostatic cyclic expansion extrusion (HCEE) as a novel severe plastic deformation process for producing long nanostructured metals", *Materials Science and Engineering: A*, vol. 718, pp. 412-417, 2018.
- [123] N. Pardis, C. Chen, R. Ebrahimi, L. S. Toth, C. F. Gu, B. Beausir and L. Kommel, "Microstructure, texture and mechanical properties of cyclic expansion–extrusion deformed pure copper". *Materials Science and Engineering: A*, vol. 628, pp. 423-432, 2015.
- [124] N. Guo, B. Song, H. B. Yu, R. L. Xin, B. S. Wang and T. T. Liu, "Enhancing tensile strength of Cu by introducing gradient microstructures via a simple torsion deformation". *Materials & Design*, vol. 90, pp. 545-550, 2016.
- [125] C. P. Wang, F. G. Li, J. H. Li, J. Z. Dong and F. M. Xue, "Microstructure evolution, hardening and thermal behavior of commercially pure copper subjected to torsion deformation". *Materials Science and Engineering A*, vol. 598, pp. 7-14, 2014.
- [126] N. Hansen, "Hall-Petch relation and boundary strengthening". *Scripta Materialia*, vol. 51, pp. 801-806, 2004.
- [127] C. X. Huang, K. Wang, S. D. Wu, Z. F. Zhang, G. Y. Li and S. Li, "Deformation twinning in polycrystalline copper at room temperature and low strain rate". *Acta Materialia*, vol. 54, pp. 655-665, 2006.
- [128] M. A. Meyers, A. Mishra and D. J. Benson, "Mechanical properties of nanocrystalline materials". *Progress in Materials Science*, vol. 51, pp. 427-556, 2006.
- [129] K. Edalati, T. Fujioka and Z. Horita, "Evolution of mechanical properties and microstructures with equivalent strain in pure Fe processed by high pressure torsion". *Materials Transactions*, vol. 50, pp. 44-50, 2009.
- [130] Y. M. Wang and E. Ma, "Three strategies to achieve uniform tensile deformation in a nanostructured metal". *Acta Materialia*, vol. 52, pp. 1699-1709, 2004.
- [131] Y. H. Zhao, X. Z. Liao, S. Cheng, E. Ma and Y. T. Zhu, "Simultaneously increasing the ductility and strength of nanostructured alloys". *Advanced Materials*, vol. 18, pp. 2280-2283, 2006.
- [132] Y. H. Zhao, X. Z. Liao, Z. Jin, R. Z. Valiev and Y. T. Zhu, "Microstructures and mechanical properties of ultrafine grained 7075 Al alloy processed by ECAP and their evolutions during annealing". *Acta Materialia*, vol. 52, pp. 4589-4599, 2004.

Acknowledgements

At the final of this thesis, I would like to express my sincerest appreciation to all the people who have made this work possible.

I would like to thank Prof. Horst Hahn who considered me to be capable of doing this PhD work. I am grateful for his interest in the project and the constructive discussions.

It is my privilege to express my deep sense of gratitude to Dr. Yulia Ivanisenko. I appreciate her vast knowledge and skills in many areas. Throughout my research, she provided encouragement, good teaching, sound advices, good company, and many interesting ideas.

I wish to thank Dr. Roman Kulagin for his scientific suggestions, friendly support and the valuable discussions.

I gratefully acknowledge Dr. Andrey Mazilkin patience in explaining to me the introductions of SEM and TEM analysis, and I appreciate his constructive comments and suggestions, and of course, the fruitful discussions. My appreciation also goes for helping with the HRTEM of my samples.

I am grateful to KNMF in face of Prof. Christian Kübel and Dr. Torsten Scherer for the access to the metallography preparation, SEM-EBSD and TEM microscope equipment.

I sincerely appreciated Prof. Laszlo Toth and Dr. Olivier Perrot help in conducting the X-ray tomography experiments and introduction for the postprocessing of the X-ray tomography.

I would like to acknowledge the affection and the support from my friends and colleagues Stefan, Dima, Svetlana, Harsha, Iwiza, Askar and Sergey. Their company has made my time at INT a memorable experience.

Special thanks to Christine Fischer and Patricia Jaeger for taking care of official matters during my stay at the Institute of Nanotechnology. And many thanks to everyone who has contributed in any way to this PhD thesis.

Financial support from the Deutsche Forschungsgemeinschaft under contract IV98/8-1 is gratefully acknowledged.

Finally, I want to thank my wife and my parents for the patience, support, and understanding.

Curriculum Vitae

Education

- Sep 2003 – Feb 2009 Ufa State Aviation Technical University
MD, Materials science
Ufa, Bashkortostan, Russia
- Sep 2001 – Jun 2003 Physics and Mathematics Lyceum Nr. 153, Ufa, Russia
- Sep 1993 – Jun 2001 School Nr. 23, Ufa, Russia

Research Experience

- Sept 2017 – present **Fellow researcher**
Karlsruhe Institute of technology, Karlsruhe, Baden-Wuerttemberg,
Germany
- Oct 2010 – Aug 2017 **Fellow researcher**
Institute for Metals Superplasticity Problems of Russian Academy of
Sciences, Russia
- May 2009 – Oct 2010 **Technical engineer**
Ufa Engine Industrial Association
- Jan 2008 – Jan 2009 **Technical staff**
Ufa State Aviation Technical University, The Institute of Physics of
Advanced Materials, Russia

Awards & Grants

- September 2014 Award: Diploma of the best scientific work among young researchers
competition of the VI International school “Material science”
- May 2010 Award: Diploma of the Russian government for the best student of technical
and human scientific work №470 from 27.05.2010

Funding

- 1 RFBR № 14-08-31344 «Experimental and theoretical analysis of the texture effect on the static strength anisotropy ultrafine-grained magnesium alloy sheets» (2014-2015) (supervisor).
- 2 RSF № 16-19-10152. The role of the precipitates in the formation of nanostructures and properties of severely deformed aluminum alloys of industrial compositions (co-performer)
- 3 DFG IV98/8-1 «Hybrid ultrafine grained materials produced by high pressure torsion extrusion» (co-performer)
- 4 DFG IV 98/12-1 Fatigue and corrosion performance of model Mg-Zn-Zr alloys subjected to the High Pressure Torsion Extrusion (co-performer)
- 5 VirtMat project № P05 and “Material Systems Engineering (MSE)” of the Helmholtz association. (co-performer)
- 6 KNMFi and MDMC initiatives (no. 43.31.01) through the research data infrastructure KADI4MAT <https://kadi.iam.kit.edu>.



Scientific Output

16 scientific publications

24 conference contributions

Publications

- 1 **Nugmanov, D.**, Kulagin, R., Perroud, O., Mail, M., Hahn, H. & Ivanisenko, Y. (2023). “Equivalent strain distribution at high pressure torsion extrusion of pure copper: Finite element modeling and experimental validation”. *Journal of Materials Processing Technology*, vol. 315, 117932.
- 2 **Nugmanov, D.**, Mazilkin, A., Hahn, H. & Ivanisenko, Y. (2019). “Structure and tensile strength of pure Cu after high pressure torsion extrusion”. *Metals*, vol. 9(10), 1081.
- 3 Omranpour, B., Ivanisenko, Y., Kulagin, R., Kommel, L., Sanchez, E. G., **Nugmanov, D.**, & Gubicza, J. (2019). “Evolution of microstructure and hardness in aluminum processed by High Pressure Torsion Extrusion”. *Materials Science and Engineering: A*, vol. 762, 138074.
- 4 **Nugmanov, D.**, Knezevic, M., Zecevic, M., Sitdikov, O., Markushev, M. & Beyerlein, I. J. (2018). “Origin of plastic anisotropy in (ultra)-fine-grained Mg–Zn–Zr alloy processed by isothermal multi-step forging and rolling: Experiments and modeling”. *Materials Science and Engineering: A*, vol. 713, pp. 81-93.
- 5 Markushev, M., **Nugmanov, D.**, Sitdikov, O. & Vinogradov, A. (2018). Structure, texture and strength of Mg-5.8 Zn-0.65 Zr alloy after hot-to-warm multi-step isothermal forging and isothermal rolling to large strains. *Materials Science and Engineering: A*, vol. 709, pp. 330-338.
- 6 Mukhametdinova, O., Ilyasov, R., **Nugmanov, D.**, Avtokratova, E., Sitdikov, O. & Markushev, M. (2016). “Effect of the size of transition-metal aluminides on the structure of 1570C aluminum alloy processed by hot multidirectional isothermal forging”. *AIP Conference Proceedings*, vol. 1783, No. 1. AIP Publishing.
- 7 **Nugmanov, D.**, Sitdikov, O. & Markushev, M. (2015). “Texture and anisotropy of yield strength in multistep isothermally forged Mg-5.8 Zn-0.65 Zr alloy”. *IOP Conference Series: Materials Science and Engineering*, vol. 82, No. 1, p. 012099. IOP Publishing
- 8 Vasilev, E., Linderov, M., **Nugmanov, D.**, Sitdikov, O., Markushev, M. & Vinogradov, A. (2015). “Fatigue performance of Mg-Zn-Zr alloy processed by hot severe plastic deformation”. *Metals*, vol. 5(4), pp. 2316-2327.
- 9 **Nugmanov, D.**, Sitdikov, O. & Markushev, M. (2015). “Structure of magnesium alloy MA14 after multistep isothermal forging and subsequent isothermal rolling”. *Physics of metals and metallography*, vol. 116, pp. 993-1001
- 10 **Nugmanov, D.**, Sitdikov, O. & Markushev, M. (2015). “Grain refinement in the magnesium alloy ZK60 during multi-step isothermal forging”. *Materials Science Forum*, vol. 830, pp. 7-10.
- 11 **Nugmanov, D.**, Sitdikov, O. & Markushev, M. (2014). “Electron-microscopy analysis of changes in magnesium alloy parameters of excess phases due to multistep isothermal forging”. *Letters on Materials*, vol. 4, pp. 209-214.

-
- 12 **Nugmanov, D.**, Markushev, M. (2013). “Microstructure of magnesium alloy MA14 after multidirectional isothermal forging in single-phase area”, *Science vector of TSU*, vol. 25, pp. 234-236.
- 13 **Nugmanov, D.**, Sitdikov, O. & Markushev, M. (2012). “About fine-grain structure forming in bulk magnesium alloy MA14 under multidirectional isothermal forging”. *Basic Problems of Material. Science*, vol. 9(2), p. 230.
- 14 **Nugmanov, D.**, Sitdikov, O. & Markushev, M. (2012). “Deformability of magnesium alloy Mg-2, 5Nd-0, 6Zr at intermediate temperatures and structures formed”. *Letters on Materials*, vol. 2(4), pp. 245-248.
- 15 **Nugmanov, D.** & Islamgaliev, R. (2012). “The texture strengthening effect in a magnesium alloy processed by severe plastic deformation”. *Reviews of Advanced Material Science*, vol. 31, pp. 157-162.
- 16 **Nugmanov, D.** & Islamgaliev, R. (2011). “Structure and mechanical properties of magnesium alloy AM60V after equal channel angular pressing and rolling”. *Metal Science and Heat Treatment*, vol. 53(1-2), pp. 8-13.